Chapter 3

Numerical Weather Prediction Models

3.1 Summary

JMA operates NWP models to meet various kinds of requirements on weather forecasting. The suite of the NWP models covers a wide temporal range of forecast periods from a few hours to two seasons providing a seamless sequence of products for the public. The following is a brief description of the major NWP models.

1. The Global Spectral Model (GSM) produces 132-hour forecasts four times a day (00, 06, 12 and 18 UTC) to support short-range forecasting (up to three days ahead) and tropical cyclone forecasts and to provide lateral boundary conditions for the Meso-Scale Model (MSM). The GSM forecasts at 00 and 12 UTC are extended to 264 hours (11 days) to support one-week forecasting. The specifications of the GSM are shown in Table 3.1.1 and a description is given in Section 3.2.

2. The Global Ensemble Prediction System (GEPS) produces seamless short to extended-range forecasts up to 34 days ahead with uncertainty for applications such as tropical cyclone forecasts, one-week forecasts and one-month forecasts as well as issuance of Early Warning Information on Extreme Weather. In addition, the Seasonal EPS system produces seven-month forecasts to support three-month forecasts, warm- and cold-season outlooks and El Niño outlooks. The specifications and other details of the GEPS are outlined in Section 3.3, and the coupled atmosphere-ocean general circulation model used in the Seasonal EPS system is described in Section 3.4.

3. The MSM produces 78-hour forecasts (00 and 12 UTC) and 39-hour forecasts (03, 06, 09, 15, 18 and 21 UTC) to support disaster prevention, very short-range precipitation forecasts and aviation forecasts, and also provides lateral boundary conditions for the Local Forecast Model (LFM). The specifications of the MSM are shown in Table 3.1.2, and a description is given in Section 3.5.

4. The Meso-scale Ensemble Prediction System (MEPS) produces 39-hour forecasts four times a day (00, 06, 12 and 18 UTC) to provide uncertainty of the MSM prediction. The specifications and other details of the MEPS are outlined in Section 3.6.

5. The LFM produces ten-hour forecasts 24 times a day on the hour to support aviation forecasts, disaster prevention and very short-range precipitation forecasts. Its specifications are shown in Table 3.1.3, and a description is given in Section 3.7.

JMA operates a global atmospheric transport and dispersion model (Section 3.8) to support its RSMC activities for nuclear environmental emergency response. The model is executed on request in coordination with the World Meteorological Organization (WMO).

JMA also operates three Chemical Transport Models (CTMs; Section 3.9 and Section 3.10). The aerosol CTM produces 96-hour forecasts of atmospheric distribution for airborne Kosa (Aeolian dust), which arrives seasonally from the Eurasian Continent. The global CTM produces 120-hour forecasts of Ultra Violet (UV)

index distribution, and the regional CTM produces 51-hour forecasts of photochemical oxidants. These models are run at 12 UTC daily.

The operational verification procedure is outlined in Section 3.11. An atmospheric transport model (Section 3.12) is operated to create information on the extent and movement of volcanic ash.

Table 3.1.1: Specifications of Global Spectral Model (GSM)

System	
Model (version)	Global Spectral Model (GSM2303)
Date of implementation	December 1987 (Latest version: 14 March 2023)
Configuration	
Horizontal resolution (Grid spacing)	Spectral triangular truncation 959 with a quadratic and reduced Gaussian grid system (TQ959), roughly equivalent to 0.125 ×0.125° (13 km) in latitude and longitude
Vertical resolution (model top)	128 stretched sigma pressure hybrid levels (0.01 hPa)
Forecast length (initial time)	132 hours (06 and 18 UTC) and 264 hours (00 and 12 UTC)
Coupling to ocean / wave / sea ice models	–
Integration time step	300 seconds
Initial conditions	
Data assimilation	Hybrid Four-dimensional variational (4D-Var) method using the Local Ensemble Transform Kalman Filter (LETKF)
Surface boundary conditions	
Treatment of sea surface	Climatological sea surface temperature with daily analysis anomaly Climatological sea ice concentration with daily analysis anomaly
Land surface analysis	Snow depth: two-dimensional optimal interpolation scheme using the first guess estimated from the satellite observation and the model forecast Temperature: first guess Soil moisture: simplified extended Kalman filter scheme
Other details	
Land surface and soil	GSM land model based on the Simple Biosphere (SiB) scheme
Radiation	Two-stream with delta-Eddington approximation for short wave (hourly) Two-stream absorption approximation method for long wave (hourly)
Numerical techniques	Spectral (spherical harmonics) in horizontal, finite differences in vertical Two-time-level, semi-Lagrangian, semi-implicit time integration scheme Hydrostatic approximation
Planetary boundary layer	Hybrid scheme combining Mellor and Yamada level-2 turbulence closure with local eddy diffusivity model Similarity theory in bulk formulae for surface layer
Convection	Prognostic Arakawa-Schubert cumulus parameterization
Cloud	PDF-based cloud parameterization
Subgrid orography	Low-level blocked-flow drag, gravity wave drag and turbulent orographic form drag schemes
Non-orographic gravity wave drag	Spectral gravity wave forcing scheme

Table 3.1.2: Specifications of Meso-Scale Model (MSM)

System	
Model (version)	Meso-Scale Model (forecast model: ASUCA)
Date of implementation	1 March 2001 (Last version: 16 June 2022)
Configuration	
Domain	Japan and its surroundings, Lambert projection, 817×661 grid points
Horizontal resolution (Grid spacing)	5 km
Vertical resolution (model top)	Stretched hybrid terrain-following coordinate grid with 96 levels (37.5 km)
Forecast length (initial time)	78 hours (00 and 12 UTC) and 39 hours (03, 06, 09, 15, 18 and 21 UTC)
Coupling to ocean / wave / sea ice models	–
Integration time step	100/3 seconds (3-stage Runge-Kutta method)
Initial conditions	
Data assimilation	4D-Var analysis
Surface boundary conditions	
Sea surface temperature	SST analysis (with variations due to atmospheric forcing considered via an ocean mixed layer model) and sea-ice distribution (fixed during integration)
Land surface analysis	Climatological soil moisture values Snow cover analysis for Japan using a land surface model
Lateral boundary conditions	
Model providing lateral boundary conditions	GSM
Lateral boundary condition update frequency	4 times a day, 0 – 45 hours (GSM00 – MSM03/06, GSM06 – MSM09, GSM12 – MSM15/18, GSM18 – MSM21) and 0 – 84 hours (GSM06 – MSM12, GSM18 – MSM00)
Other details	
Soil scheme	Ground temperature prediction using an eight-layer model Soil moisture prediction using force-restore application
Radiation	Two-stream with delta-Eddington approximation for short wave (every 15 minutes) Two-stream absorption approximation for long wave (every 15 minutes)
Large-scale dynamics	Finite volume method with Arakawa-C-type staggered coordinates, horizontally explicit and vertically implicit time integration scheme, combined third- and first-order upwind finite difference schemes in flux form with a limiter proposed by Koren (1993) in advection treatment for monotonicity, time-splitting of vertical advection, fully compressible non-hydrostatic equations
Planetary boundary layer	Mellor-Yamada-Nakanishi-Niino Level-3 scheme Similarity theory in bulk formulae for surface layer
Convection	Kain-Fritsch convection scheme
Cloud/microphysics	Three ice-phase bulk cloud microphysics Consideration of PDF-based cloud distribution in microphysics Time-split treatment for rain and graupel sedimentation Cloud water and cloud cover diagnosis using a partial condensation scheme
Orography	Mean orography smoothed to eliminate shortest-wave components
Horizontal diffusion	–
Gravity wave drag	–

Table 3.1.3: Specifications of Local Forecast Model (LFM)

System	
Model (version)	Local Forecast Model (forecast model: ASUCA)
Date of implementation	30 August 2012 (Last version: 28 March 2023)
Configuration	
Domain	Japan and its surroundings, Lambert projection, 1,581 × 1,301 grid points
Horizontal resolution (Grid spacing)	2 km
Vertical resolution (model top)	Stretched hybrid terrain-following coordinate grid with 96 levels (21.8 km)
Forecast length (initial time)	10 hours (00, 01, 02, 03, 04, 05, 06, 07, 08, 09, 10, 11, 12, 13, 14, 15, 16, 17, 18, 19, 20, 21, 22 and 23 UTC)
Coupling to ocean / wave / sea ice models	–
Integration time step	12 seconds
Initial conditions	
Data assimilation	Three-hour assimilation window based on hybrid 3D-Var and three one-hour forecasts
Surface boundary conditions	
Sea surface temperature	SST analysis and sea-ice distribution (both fixed during time integration)
Land surface analysis	Climatological values of evaporability, roughness length and albedo Snow cover analysis from MSM
Lateral boundary conditions	
Model providing lateral boundary conditions	MSM
Lateral boundary condition update frequency	8 times a day, 0 – 13-hour forecasts using the latest MSM information
Other details	
Soil scheme	Ground temperature prediction using an eight-layer model Evaporability prediction initialized using climatological values depending on location and season
Radiation	Two-stream with delta-Eddington approximation for short wave (every 15 minutes) Two-stream absorption approximation for long wave (every 15 minutes)
Large-scale dynamics	Finite volume method with Arakawa-C-type staggered coordinates, horizontally explicit and vertically implicit time integration scheme, combined third- and first-order upwind finite difference schemes in flux form with a limiter proposed by Koren (1993) in advection treatment for monotonicity, time-splitting of vertical advection, fully compressible non-hydrostatic equations
Planetary boundary layer	Mellor-Yamada-Nakanishi-Niino Level-3 scheme Similarity theory in bulk formulae for surface layer
Convection	Convective initiation
Cloud/microphysics	Three ice-phase bulk cloud microphysics Time-split treatment for rain and graupel sedimentation Cloud water and cloud cover diagnosis using a partial condensation scheme
Orography	Mean orography smoothed to eliminate shortest-wave components
Horizontal diffusion	–
Subgrid orography	Turbulent orographic form drag scheme

3.2 Global Spectral Model (JMA-GSM2303)

3.2.1 Introduction

The Global Spectral Model (GSM) employs primitive equations to express resolvable motions and states of the atmosphere. It also incorporates sophisticated parameterization schemes for physical processes. In the horizontal direction, prognostic variables are spectrally discretized using triangular truncation at wave number 959 with a quadratic reduced Gaussian grid system (TQ959[1]), and the corresponding transform grids cover around 0.125° in both longitude and latitude. In the vertical direction, the model has 128 layers up to 0.01 hPa.

JMA has operated GSM since March 1988. The model originally had a horizontal resolution of T63 and 16 vertical layers up to 10 hPa with a sigma coordinate system.

In a model upgrade implemented in November 1989, the truncation wave number and the number of vertical layers were increased to T106 and 21, respectively, and a hybrid η vertical coordinate system was adopted.

In March 1996, the horizontal resolution was doubled to T213 and the number of vertical layers was increased to 30. The cumulus parameterization was changed from a Kuo scheme to a prognostic Arakawa-Schubert scheme.

In December 1999, the parameterization schemes underwent extensive refinement. Treatment of cloud water content as a prognostic variable was introduced, and the moist convection process was improved.

In March 2001, the number of vertical layers was increased to 40 and the vertical domain was extended up to 0.4 hPa. The model was highly parallelized to suit massively distributed-memory parallel computer operation.

In February 2005, the Eulerian advection scheme was replaced with a semi-Lagrangian one, and the spectral resolution was increased from T213 (quadratic grid) to TL319 (linear grid). Incremental non-linear normal mode initialization and vertical mode initialization were also introduced.

In March 2006, operations at 06 and 18 UTC were begun with a forecast range of 36 hours in addition to those conducted at 00 UTC with a forecast range of 90 hours and 12 UTC with a forecast range of 216 hours.

In November 2007, the horizontal resolution of GSM was enhanced to TL959, while the number of vertical layers was increased to 60 and the vertical domain was extended up to 0.1 hPa (Iwamura and Kitagawa 2008; Nakagawa 2009). The numerical integration scheme was upgraded from the three-time-level leap-frog scheme to a two-time-level scheme. The forecasts run at 00, 06 and 18 UTC were altered to each cover a uniform period of 84 hours. At the same time, the 20-km-resolution Regional Spectral Model (RSM) and the 24-km-resolution Typhoon Model (TYM) were retired from operational use.

In August 2008, a reduced Gaussian grid was incorporated into GSM as a new dynamical core. This removed redundant grid points at higher latitudes, thereby saving on computational resources (Miyamoto 2006). Incremental non-linear normal mode initialization and vertical mode initialization were eliminated.

In December 2012, a relative humidity threshold was introduced to the diagnostic stratocumulus scheme (Shimokobe 2012).

In March 2013, the coverage period of the forecast run at 12 UTC was extended from 216 to 264 hours.

In April 2013, the radiation scheme was improved by updating the coefficients used for the short-wave parameterization of water vapor.

In March 2014, the number of vertical layers was increased to 100 and the vertical domain was extended up to 0.01 hPa. The parameterization schemes for variables such as the boundary layer, radiation, non-orographic gravity waves and deep convection were also revised (Yonehara et al. 2014).

In March 2016, various parameterization schemes such as deep convection, cloud, radiation, land model, and sea surface were substantially revised (Yonehara et al. 2017).

In May 2017, the parameterization schemes underwent extensive refinement (Yonehara et al. 2018).

In June 2018, the coverage period of forecasts run at 00, 06 and 18 UTC was extended from 84 to 132 hours.

In March 2020, various parameterization schemes such as surface drag processes, land surface processes, and surface albedo and stratocumulus on sea ice were refined (Yonehara et al. 2020).

---

[1]In older GSM versions with Eulerian advection, quadratic grid denotations were indicated by 'T'. The latest GSM with semi-Lagrangian advection re-employed quadratic grid to increase effective resolution (the smallest spatial scale not contaminated by numerical errors or noises). In this section, 'TQ' denotes quadratic grids employed for effective resolution enhancement.

In February 2021, the coverage period of forecasts run at 00 UTC was extended from 132 to 264 hours.

In March 2021, the number of vertical layers was increased to 128 (Ujiie *et al.* 2021).

In March 2023, the horizontal resolution of GSM was enhanced to TQ959 with refinements to parametrized surface drag, non-orographic sub-grid gravity waves, and radiation (Yonehara *et al.* 2023). The source datasets used were updated for application of orographic ancillary files (Kanehama *et al.* 2023a).

3.2.2 Dynamics

The GSM is based on the framework of a semi-implicit semi-Lagrangian global model. In order to reduce the general shortcomings of semi-Lagrangian models (such as the lack of conservation properties and the high computational cost of three-dimensional interpolations), a vertically conservative semi-Lagrangian scheme (Yukimoto *et al.* 2011) is adopted for the GSM.

3.2.2.1 Governing Equations

The GSM is run on an η vertical coordinate system, which is a hybrid between pressure p and σ ($\sigma = p/p_S$, where p_S is surface pressure), implicitly defined as $p = A(\eta) + B(\eta)p_S$. η ranges from 0 to 1; $\eta = 1$ corresponds to the lower boundary (ground surface) and $\eta = 0$ corresponds to the upper boundary. The prognostic variables (wind vector $\boldsymbol{u} = (u, v)$, temperature T, pressure p, specific humidity q and cloud water content q_c) follow the system of primitive equations in the η-coordinate system as follows:

$$\frac{d\mathbf{u}}{dt} = -f\mathbf{z} \times \mathbf{u} - (\nabla\Phi + R_d T_V \nabla \ln p) + \mathbf{F}_{\boldsymbol{u}} \tag{3.2.1}$$

$$\frac{dT}{dt} = \frac{\kappa T_V \omega}{\left[1 + \left(C_{pv}/C_{pd} - 1\right)q\right]p} + F_T \tag{3.2.2}$$

$$\frac{dq}{dt} = F_q \tag{3.2.3}$$

$$\frac{dq_c}{dt} = F_c \tag{3.2.4}$$

$$\frac{\partial}{\partial t}\left(\frac{\partial p}{\partial \eta}\right) + \nabla \cdot \left(\mathbf{u}\frac{\partial p}{\partial \eta}\right) + \frac{\partial}{\partial \eta}\left(\dot{\eta}\frac{\partial p}{\partial \eta}\right) = 0 \tag{3.2.5}$$

Here, d/dt is a total derivative defined as $d/dt = \partial/\partial t + \mathbf{u} \cdot \nabla + \dot{\eta}\partial/\partial\eta$, and ∇ is a horizontal gradient operator. The other notations used above are conventional: $\mathbf{z}$ is the unit vertical vector, T_V is the virtual temperature, f is the Coriolis parameter, R_d is the gas constant for dry air, and $\kappa = R_d/C_{pd}$. C_{pd} is the specific heat capacity at the constant pressure of dry air and C_{pv} is the specific heat capacity at the constant pressure of water vapor. $\mathbf{F}_{\boldsymbol{u}}$, F_T, F_q and F_c are tendencies relating to parameterized processes. In addition, $\mathbf{F}_{\boldsymbol{u}}$ and F_T include the effects of horizontal diffusion (to be described later). Integrating Eq. (3.2.5) with respect to η using the boundary conditions of $\dot{\eta} = 0$ at $\eta = 0$ and $\eta = 1$, η-velocity and ω are found:

$$\dot{\eta}\frac{\partial p}{\partial \eta} = -\frac{\partial p}{\partial t} - \int_0^\eta \nabla \cdot \left(\mathbf{u}\frac{\partial p}{\partial \eta'}\right)d\eta' \tag{3.2.6}$$

$$\omega \equiv \frac{dp}{dt} = -\int_0^\eta \nabla \cdot \left(\mathbf{u}\frac{\partial p}{\partial \eta'}\right)d\eta' + \mathbf{u} \cdot \nabla p \tag{3.2.7}$$

The geopotential Φ is given by the following hydrostatic relation:

$$\frac{\partial \Phi}{\partial \eta} = -R_d T_V \frac{\partial \ln p}{\partial \eta} \tag{3.2.8}$$

3.2.2.2 Vertical Finite Difference Scheme

The vertical finite difference scheme is coded by following Simmons and Burridge (1981). The prognostic variables $\mathbf{u}$, T, q and q_c are defined on the full levels, while η (including vertical fluxes) is defined on half-integer levels. Pressure on half-integer levels are expressed as

$$p_{k-1/2} = A_{k-1/2} + B_{k-1/2}p_S \qquad (k = 1, 2, \ldots, \text{kmax}) \tag{3.2.9}$$

Here, the level index k increases with height, $kmax$ is the index of the highest model level, $A_{k-1/2} = A(\eta_{k-1/2})$ and $B_{k-1/2} = B(\eta_{k-1/2})$. The profiles of $A_{k-1/2}$ and $B_{k-1/2}$ are determined by following Kawai et $al.$ (2013). $A_{1/2}$ is set to zero so that the lowest level coincides with the ground surface, and values of $B_{k-1/2}$ above 60hPa are set to zero so that these levels coincide with constant pressure surfaces. For intermediate levels, $A_{k-1/2}$ and $B_{k-1/2}$ vary smoothly with k.

From the hydrostatic relation given by Eq. (3.2.8) the finite difference form of geopotential on the full level is chosen as

$$\Phi_k = \Phi_S + \sum_{k'=1}^{k-1} R_d T_{Vk'} \ln\left(\frac{p_{k'-1/2}}{p_{k'+1/2}}\right) + \alpha_k R_d T_{Vk} \tag{3.2.10}$$

$$\alpha_k = \begin{cases} 1 - \dfrac{p_{k+1/2}}{\delta p_k} \ln\left(\dfrac{p_{k-1/2}}{p_{k+1/2}}\right) & (1 \le k < \text{kmax}) \\ \ln 2 & (k = \text{kmax}) \end{cases} \tag{3.2.11}$$

Here, Φ_S is the geopotential at the surface, and $\delta p_k = p_{k-1/2} - p_{k+1/2}$. The pressure gradient force term in Eq. (3.2.1) and the adiabatic heating rate term in Eq. (3.2.2) can then be written in discretized form as

$$(\nabla \Phi + R_d T_V \nabla \ln p)_k = \nabla \Phi_k + \frac{R_d T_{Vk}}{\delta p_k} \left[\ln\left(\frac{p_{k-1/2}}{p_{k+1/2}}\right) \nabla p_{k+1/2} + \alpha_k \nabla(\delta p_k) \right] \tag{3.2.12}$$

and

$$\left[\frac{\kappa T_V}{C_p/C_{pd}} \frac{\omega}{p}\right]_k = \frac{\kappa T_{Vk}}{C_{pk}/C_{pd}} \frac{1}{\delta p_k} \left[\left(\ln\frac{p_{k-1/2}}{p_{k+1/2}}\right) \left(B_{k+1/2}\mathbf{u}_k \cdot \nabla p_S - \sum_{l=k+1}^{\text{kmax}} \nabla \cdot (\mathbf{u}_l \delta p_l)\right) - \alpha_k (\nabla \cdot \mathbf{u}_k)\delta p_k \right] \tag{3.2.13}$$

respectively, where C_p is the specific heat capacity at the constant pressure of moist air, that defined as $C_p = [1 + (C_{pv}/C_{pd} - 1)q]C_{pd}$. The vertical mass flux in Eq. (3.2.6) is discretized as

$$\left(\dot{\eta}\frac{\partial p}{\partial \eta}\right)_{k-1/2} = -B_{k-1/2}\frac{\partial p_S}{\partial t} - \sum_{l=k}^{\text{kmax}} \nabla \cdot (\mathbf{u}_l \delta p_l) = B_{k-1/2}\sum_{l=1}^{\text{kmax}} \nabla \cdot (\mathbf{u}_l \delta p_l) - \sum_{l=k}^{\text{kmax}} \nabla \cdot (\mathbf{u}_l \delta p_l) \tag{3.2.14}$$

3.2.2.3 Horizontal Grid

To mitigate the overconcentration of grid points at high latitudes and lower the computational cost, a reduced Gaussian grid is adopted for the GSM. The number of east-west grid points at each latitude is determined based on the magnitude of associated Legendre functions, which is negligibly small at high latitudes and in high orders. With this method, the computational cost of Legendre transformation can also be reduced (Juang 2004). The number of east-west grid points is in fact restricted by FFT package specifications, the number of east-west decompositions in parallelization (as described in 3.2.10) and the interval of coarser radiation grids (as shown in 3.2.3).

3.2.2.4 Semi-implicit Semi-Lagrangian Formulation

Prior to the time integration, the forecast equations (Eq. (3.2.1) - Eq. (3.2.5)) are rewritten in the form of $d_H X/dt = \partial X/\partial t + \mathbf{u} \cdot \nabla X = R$ with vertical advection terms incorporated into R on the right-hand side. These equations are integrated with respect to time along the trajectory of the parcel from the departure point D at time t to the arrival point A at time $t + \delta t$. The linear term L separated from the forcing term R is treated semi-implicitly (i.e. using a trapezoidal rule), and the remaining R, including vertical advection terms, are treated with spatial averaging (Tanguay *et al.* 1992).

The resulting linear terms are slightly amplified by the factor $\beta = 1.2$ for computational stability, and the following is obtained:

$$X^{A+} - X^{D0} = \delta t \frac{R^{A0} + R^{D(+)}}{2} + \delta t \beta \left[\frac{L^{A+} + L^{D-}}{2} - \frac{L^{A0} + L^{D0}}{2} \right] \tag{3.2.15}$$

Superscript A represents the arrival point $\mathbf{x}_{ij}$ assumed to be on the Gaussian grid, and D is the departure point $\mathbf{x}_{ij} - \boldsymbol{\alpha}$ (the displacement vector $\boldsymbol{\alpha}$, whose calculation will be described later). The abbreviations used above are the same as those for $X^{A+} = X(\mathbf{x}, t + \delta t)$, $X^{D0} = X(\mathbf{x} - \boldsymbol{\alpha}, t)$, $R^{A0} = R(\mathbf{x}, t)$, $R^{D(+)} = R(\mathbf{x} - \boldsymbol{\alpha}, t + \delta t)$ and others. $R^{D(+)}$ is calculated based on extrapolation with respect to time. Rearranging the terms of the above equations gives a system of linear equations for the unknown values X^{A+}:

$$X^{A+} - \frac{\beta \delta t}{2} L^{A+} = \left[X^0 + \frac{\delta t}{2} \left\{ R^{(+)} - \beta \left(L^0 - L^- \right) \right\} \right]^D + \frac{\delta t}{2} \left[R^0 - \beta L^0 \right]^A \tag{3.2.16}$$

3.2.2.5 Vertically Conservative Semi-Lagrangian Scheme

Yoshimura and Matsumura (2003, 2004) developed a vertically conservative semi-Lagrangian scheme in which vertical advection is treated separately from horizontal advection so that conserved quantities such as water vapor under non-dissipative conditions are preserved in the vertical direction. Processing advection separately in the horizontal and vertical directions also reduces the model's cost of interpolation.

Eq. (3.2.16) can be reformulated with flux forms appropriate for a scheme in which vertical advection can retain conservative properties. Beginning with Eq. (3.2.5) and Eq. (3.2.1) - Eq. (3.2.4), rewriting is performed as follows:

$$\frac{d_H}{dt} \frac{\partial p}{\partial \eta} = -D \frac{\partial p}{\partial \eta} - \frac{\partial}{\partial \eta} \left(\dot{\eta} \frac{\partial p}{\partial \eta} \right) \tag{3.2.17}$$

$$\frac{d_H}{dt} \left(X \frac{\partial p}{\partial \eta} \right) = -DX \frac{\partial p}{\partial \eta} - \frac{\partial}{\partial \eta} \left(\dot{\eta} X \frac{\partial p}{\partial \eta} \right) + R_X \frac{\partial p}{\partial \eta} \tag{3.2.18}$$

Here, X represents $\mathbf{u}$, T_V, q and q_c, and $R_X = dX/dt$. The parallel nature of these equations is easily recognizable. The first term on the right hand side of these equations represents the increase caused by horizontal convergence, and the second term is the increase caused by vertical flux convergence. With respect to the latter, where q and q_c being conservative when $R_X = 0$, devising a vertically integrated quantity that remains unchanged in vertical advection appears to be a promising approach. A simple outline of the procedure is given here for specific humidity q without R_q.

Vertical discretization and time integration during the period δt described earlier give the following equations with the omission of terms related to the semi-implicit method for reasons of simplicity:

$$(\delta p_k)^{A+} = \left[(\delta p_k)^0 - \frac{1}{2} (D_k \delta p_k)^{(+)} \delta t + \frac{1}{2} \left\{ \left(\dot{\eta} \frac{\partial p}{\partial \eta} \right)_{k+1/2} - \left(\dot{\eta} \frac{\partial p}{\partial \eta} \right)_{k-1/2} \right\}^{(+)} \delta t \right]^D$$

$$+ \left[-\frac{1}{2} (D_k \delta p_k)^0 \delta t + \frac{1}{2} \left\{ \left(\dot{\eta} \frac{\partial p}{\partial \eta} \right)_{k+1/2} - \left(\dot{\eta} \frac{\partial p}{\partial \eta} \right)_{k-1/2} \right\}^0 \delta t \right]^A \tag{3.2.19}$$

$$(q_k \delta p_k)^{A+} = \left[(q_k \delta p_k)^0 - \frac{1}{2} q_k^0 (D_k \delta p_k)^{(+)} \delta t + \frac{1}{2} \left\{ \left(q\dot{\eta} \frac{\partial p}{\partial \eta} \right)_{k+1/2} - \left(q\dot{\eta} \frac{\partial p}{\partial \eta} \right)_{k-1/2} \right\}^{(+)} \delta t \right]^D$$

$$+ \left[-\frac{1}{2} q_k^+ (D_k \delta p_k)^0 \delta t + \frac{1}{2} \left\{ \left(q\dot{\eta} \frac{\partial p}{\partial \eta} \right)_{k+1/2} - \left(q\dot{\eta} \frac{\partial p}{\partial \eta} \right)_{k-1/2} \right\}^0 \delta t \right]^A \tag{3.2.20}$$

$$p_{k-1/2} = \sum_{k'=k}^{kmax} \delta p_{k'}, \quad (k = 1, 2, \ldots, kmax) \tag{3.2.21}$$

Here, the vertically cumulative quantity Q is defined as follows:

$$Q_{k-1/2} = \sum_{k'=k}^{kmax} \delta Q_{k'}, \quad \delta Q_k = q_k \delta p_k, \quad (k = 1, 2, \ldots, kmax + 1) \tag{3.2.22}$$

Eq. (3.2.20) rewritten for δQ_k is found to be similar to Eq. (3.2.19) for δp_k, and there is a clear correspondence between Q and p. Computation of Q can therefore be carried out in the five steps outlined below in a fashion parallel to that of p. The first two steps concern the operations inside the square brackets $[\ldots]^D$ in the above equations. The third step involves the calculation of variables at departure points based on interpolation. The fourth and the fifth steps are similar to the first two, but for the operations in the square brackets $[\ldots]^A$.

1. First step: Horizontal divergence is calculated. As the mass of each layer δp_k varies to $\delta p_k'$, the half-level pressure values $p_{k-1/2}$ by which layers are bound also shift to $p_{k-1/2}'$, which can be computed using Eq. (3.2.21). The values of q_k remain constant under the horizontal convergence $q_k' = q_k$.

2. Second step: Vertical flux convergence is calculated using Eq. (3.2.14) as in the Eulerian scheme. In the same way as in the first step, $\delta p_k'$ varies to $\delta p_k''$, and the values of $p_{k-1/2}'$ shift to $p_{k-1/2}''$ except $k = 1$ ($p_{1/2}' = p_{1/2}''$). In this step, the shift in $Q_{k-1/2}'$ caused by the vertical flux convergence is computed based on interpolation from $Q_{k-1/2}'(p_{k-1/2}')$ using $Q_{k-1/2}'' = Q_{k-1/2}'(p_{k-1/2}'')$. This procedure ensures the conservation of the total mass-weighted integral $Q_{1/2}' = Q_{1/2}''$, because $p_{1/2}' = p_{1/2}''$ holds and the other values of $p_{k-1/2}''$ ($k = 2, 3, \ldots, kmax$) merely have their intervals changed in the vertical column. New values of q_k'' are computed using $\delta Q_k''$ and $\delta p_k''$ with Eq. (3.2.22).

3. Third step: Horizontal advection is incorporated by computing $(\delta p_k)^D$ and q_k^D via quasi-cubic interpolation.

4. Forth step: Vertical flux convergence is calculated at the arrival point via the second step.

5. Fifth step: Horizontal divergence is calculated at the arrival point via the first step.

The time-integration of q and q_c is completed based on these five steps, and that of $\mathbf{u}$, T_V and p_S is followed by the semi-implicit calculation shown in Eq. (3.2.16).

3.2.2.6 Departure Point Determination

The displacement vector $\boldsymbol{\alpha}$ (as yet undetermined) obeys the implicit equation

$$\boldsymbol{\alpha} = \delta t \left\{ \frac{\mathbf{u}_k(\mathbf{x}_{ij} - \boldsymbol{\alpha}, t + \delta t) + \mathbf{u}_k(\mathbf{x}_{ij}, t)}{2} \right\} \tag{3.2.23}$$

which expresses that the horizontal advection during the time interval δt is related to the average of future time-step wind value at the departure point and current time-step wind value at the arrival point (SETTLS; Hortal 2002). To improve stability, a method based on wind integrated in a semi-Lagrangian scheme rather than the time extrapolated wind is adopted (Yoshimura 2002). This implicit equation is solved by successive insertions of $\boldsymbol{\alpha}$. For the computation of these vector components, it is considered that the axes of the local coordinates (λ, φ) rotate due to the spherical metric as a parcel advances along a trajectory, as is the case whenever horizontal vector components are interpolated on a sphere. The wind at the departure point is computed from linear interpolation except for the last third of the iteration, for which a quasi-cubic approach is used.

3.2.2.7   Spectral Method and Horizontal Diffusion

Spectral variables (i.e. vorticity $\zeta(= \mathbf{z} \cdot \nabla \times \mathbf{u})$, divergence $D(= \nabla \cdot \mathbf{u})$, T_V and $\ln(p_S)$) are expanded in terms of spherical harmonics with triangular truncation. In accordance with the framework of the semi-Lagrangian scheme, a linear Gaussian transformation grid is used. Solutions of horizontal Helmholtz equations (derived when Eq. (3.2.16) is solved for D), horizontal diffusion and variables such as the differentials on the sphere are calculated using the spectral method (Bourke 1974; Hoskins and Simmons 1975). The remaining variables q and q_c are defined only on grid points.

To prevent the accumulation of small scale noise (spectral blocking), fourth-order linear horizontal diffusion is applied to ζ, D and T_V:

$$\left(\frac{\partial \zeta}{\partial t}\right)_{\mathrm{hdiff,4th}} = -K_{\mathrm{4th}}\left(\nabla^4 - \frac{4}{a^4}\right)\zeta \tag{3.2.24a}$$

$$\left(\frac{\partial D}{\partial t}\right)_{\mathrm{hdiff,4th}} = -K_{\mathrm{4th}}\nabla^4 D \tag{3.2.24b}$$

$$\left(\frac{\partial T_V}{\partial t}\right)_{\mathrm{hdiff,4th}} = -K_{\mathrm{4th}}\nabla^4\left[T_V - \frac{\partial \bar{T}_V}{\partial \bar{p}}p\right] = -K_{\mathrm{4th}}\nabla^4\left[T_V - \frac{\partial \bar{T}_V}{\partial \bar{p}}B(\eta)p_S\right] \tag{3.2.24c}$$

Here, K_{4th} is the diffusion coefficient for the fourth-order horizontal diffusion and a is the radius of the earth. Bars over variables indicate the global average on the η-surface. Angular momentum conservation does not allow the horizontal diffusion process to work on vorticity with total wave number 1 as shown by Eq. (3.2.24a). Diffusion for virtual temperature is modified to work on the constant pressure surface; otherwise, diffusion on a declining η-surface may produce spurious mixing along steep mountain slopes. K_{4th} is chosen so that the power spectrum of enstrophy coincides with that expected based on the two-dimensional turbulence theory.

To provide a sponge layer that absorbs waves incident on the upper boundary, second-order linear horizontal diffusion is applied to the divergence term D in layers above 30hPa:

$$\left(\frac{\partial D}{\partial t}\right)_{\mathrm{hdiff,2nd}} = -K_{\mathrm{2nd}}\nabla^2 D \tag{3.2.25a}$$

$$K_{\mathrm{2nd}} = K_0 \sin^2\left(\frac{\pi}{2}\frac{\ln p - \ln p_{\mathrm{btm}}}{\ln p_{\mathrm{top}} - \ln p_{\mathrm{btm}}}\right) \tag{3.2.25b}$$

Here, K_0 is the base diffusion coefficient for second-order horizontal diffusion, p_{top} is the pressure at the highest model level (0.01hPa), and p_{btm} is the pressure at the altitude where the sponge layer begins (30hPa). To suppress wave reflection at the upper boundary, K_{2nd} is gradually enhanced with height as shown by Eq. (3.2.25b). K_0 is determined experimentally so that spurious wave reflections at the upper boundary can be appropriately removed.

These fourth and second-order horizontal diffusion terms are calculated backward and implicitly in spectral forms as an independent step after semi-implicit time integration.

3.2.3   Radiation

The radiative heating rate is computed as the divergence of net radiation fluxes:

$$\left(\frac{\partial T}{\partial t}\right)_{\mathrm{rad}} = \frac{g}{C_p}\frac{\partial F}{\partial p} \tag{3.2.26}$$

where F ($= F^\uparrow - F^\downarrow$) is the net radiation flux, $F^\uparrow$ ($F^\downarrow$) is the upwelling (downwelling) radiation flux, g is the acceleration of gravity and C_p is the specific heat at the constant pressure of moist air.

Solving the radiative transfer equation is computationally very expensive. To reduce this burden, full radiation computation is performed only once an hour for longwave and shortwave on a coarser (reduced radiation) grid. The radiative heating rates associated with longwave and shortwave radiation are corrected for every time step using the surface temperature and the solar zenith angle, respectively.

3.2.3.1 Longwave Radiation

The two-stream radiation transfer method involving the absorption approximation approach (Yabu 2013) is adopted for longwave flux and cooling rate computation. The spectrum in the longwave region is divided into 11 bands as shown in Table 3.2.1.

Table 3.2.1: Band configuration for the longwave radiation scheme. The calculation approaches for absorption associated with atmospheric molecules are C-k (correlated k-distribution method) and S-k (k-distribution method with scaling approximation). Notation in each parenthesis denotes gas overlap assumption (pf: perfectly correlated; no: perfectly uncorrelated; pt: partly correlated; cg: combined gas). The number of sub-bands is also shown in each parenthesis.

Band Number	1	2	3a	3b	3c	4	5	6	7	8	9
Wavenumber (/cm)	25-340	340-540	540-620	620-720	720-800	800-980	980-1100	1100-1215	1215-1380	1380-1900	1900-3000
Major absorption gas											
H2O(Line)	C-k(16)		C-k(16,cg)			S-k(6)	S-k(6,pf)	S-k(16,pf)	S-k(4)	C-k(16)	S-k(6)
CO2											
O3							C-k(16)	C-k(16)			
H2O(Continuum)	S-k(16,pt)					S-k(6,pf)		S-k(16,pf)	S-k(4,pf)	S-k(16,pt)	S-k(6,pf)
Minor absorption gas											
CO2						S-k(6,pf)					
N2O			S-k(6,pf)						S-k(2,no)		
CH4								S-k(16,pf)	S-k(2,no)		
CFC-11,CFC-12,HCFC-22						S-k(6,pf)					
Number of sub-bands	16	16	16	16	16	6	16	16	16(=4x2x2)	16	6

In the two-stream method, downwelling (upwelling) radiation fluxes are calculated sequentially from the model top (surface) as follows:

$$F^{\downarrow}_{k-1/2} = 0 \qquad\qquad (k = k_{max} + 1) \qquad\qquad (3.2.27a)$$

$$F^{\downarrow}_{k-1/2} = F^{\downarrow}_{k+1/2} e^{-\tau_k/\mu} + B^{\downarrow}_k (1 - e^{-\tau_k/\mu}) \qquad\qquad (k = k_{max}, \cdots, 1) \qquad\qquad (3.2.27b)$$

$$F^{\uparrow}_{k-1/2} = B_s \qquad\qquad (k = 1) \qquad\qquad (3.2.27c)$$

$$F^{\uparrow}_{k-1/2} = F^{\uparrow}_{k-3/2} e^{-\tau_{k-1}/\mu} + B^{\uparrow}_{k-1} (1 - e^{-\tau_{k-1}/\mu}) \qquad\qquad (k = 2, \cdots, k_{max} + 1) \qquad\qquad (3.2.27d)$$

where $F^{\downarrow}_{k-1/2}$ ($F^{\uparrow}_{k-1/2}$) is the downwelling (upwelling) radiation flux at the half-integer level $k - 1/2$, τ_k is the optical thickness of the model layer k, $B^{\downarrow}_k$ ($B^{\uparrow}_k$) is the downward (upward) effective Planck flux (Chou *et al.* 2001) at the model layer k, B_s is the Planck flux at the surface and $1/\mu$ (= 1.66) is the diffusivity factor.

Depending on the absorber and the spectral band, absorption associated with atmospheric molecules is evaluated using one of two k-distribution methods (see Table 3.2.1). The correlated k-distribution method (Fu and Liou 1992) is applied to absorption dominant in the middle atmosphere. Absorption coefficients at 51 pressure levels between 1000 and 0.01 hPa are tabulated in advance based on the Line-By-Line calculation, and gas absorption data are derived from HITRAN2000 (Rothman *et al.* 2003). The k-distribution method with scaling approximation (Chou *et al.* 2001) is applied to absorption with a Lorentzian line shape assumed, and only one absorption coefficient at a specified pressure level (500 hPa) is prepared. This method is also applied to H$_2$O continuum absorption based on the MT-CKD model with scaling parameters from Zhong and Haigh (1995).

To handle the overlapping of gas absorption within each band, one of three assumptions (perfectly correlated, perfectly uncorrelated and partly correlated) (Zhang *et al.* 2003) is made other than that for CO$_2$ and H$_2$O in the 540–800 cm^{-1} region, which is handled using the direct combined gas mapping approach of Li and Barker (2005) (see Table 3.2.1).

Maximum-random cloud overlapping (Geleyn and Hollingsworth 1979) is assumed in the longwave radiation scheme, and is implemented to the two-stream method as per Li (2002). Cloud optical thickness is parameterized as per Lindner and Li (2000) for liquid droplets and as per Ebert and Curry (1992) for ice particles.

3.2.3.2 Shortwave Radiation

Shortwave scattering and absorption are modeled in two-stream formulation using the delta-Eddington approximation (Joseph et al. 1976; Coakley et al. 1983). The spectrum in the shortwave region is divided into 16 bands (10 in ultraviolet, 5 in visible and 1 in near-infrared) based on Freidenreich and Ramaswamy (1999), while absorption by water vapor in the near-infrared region is calculated via exponential-sum fitting of transmissions method with seven sub-bands based on Collins et al. (2006).

Assuming a plane-parallel atmosphere, diffuse radiation fluxes are derived from the following simultaneous equations (Meador and Weaver 1980):

$$\frac{dF^\uparrow}{d\tau} = \gamma_1 F^\uparrow - \gamma_2 F^\downarrow - \gamma_3 \omega_0 S_0 e^{-\tau/\mu_0} \tag{3.2.28a}$$

$$\frac{dF^\downarrow}{d\tau} = \gamma_2 F^\uparrow - \gamma_1 F^\downarrow + (1 - \gamma_3)\omega_0 S_0 e^{-\tau/\mu_0} \tag{3.2.28b}$$

where τ is the optical thickness, ω_0 is the single scattering albedo and S_0 is the incident solar irradiance in the direction μ_0 (the cosine of the solar zenith angle). The coefficients γ_i ($i = 1, \cdots, 3$) are given by

$$\gamma_1 = \frac{1}{4}[7 - \omega_0(4 + 3g)], \quad \gamma_2 = -\frac{1}{4}[1 - \omega_0(4 - 3g)], \quad \gamma_3 = \frac{1}{4}(2 - 3g\mu_0) \tag{3.2.29}$$

where g is the asymmetry factor. In the delta-Eddington method, solar optical properties such as τ, ω_0 and g are adjusted using the fraction of forward-scattering peak f:

$$\tau' = (1 - \omega_0 f)\tau, \quad \omega_0' = \frac{(1 - f)\omega_0}{1 - \omega_0 f}, \quad g' = \frac{g - f}{1 - f} \tag{3.2.30}$$

The shortwave radiation flux in each column is calculated using the Practical Independent Column Approximation (PICA; Nagasawa 2012) method, which is a simplified ICA approach based on Collins (2001). The total shortwave radiation flux F is given as a weighted average of the fluxes in each subcolumn as follows:

$$F = \frac{1}{A_{tot}} \sum_{i=1}^{N_{max}} A_i F_i \tag{3.2.31}$$

where A_{tot} is the total area of the relevant subcolumns, A_i is the fractional area of each subcolumn, F_i is the flux in each subcolumn and N_{max} is the maximum number of subcolumns. The binary cloud configuration in the column is given by cloud cover assuming maximum-random cloud overlapping.

The reflectance and transmittance of the layer are calculated as functions of the total optical thickness τ_{total}, the total single scattering albedo $\omega_{0\,\text{total}}$ and the total asymmetry factor g_{total} of the layer:

$$\tau_{\text{total}} = \tau_R + \tau_g + \tau_a + \tau_c \tag{3.2.32a}$$

$$\omega_{0\,\text{total}} = \frac{\tau_R + \omega_{0a}\tau_a + \omega_{0c}\tau_c}{\tau_R + \tau_g + \tau_a + \tau_c} \tag{3.2.32b}$$

$$g_{\text{total}} = \frac{g_a\omega_{0a}\tau_a + g_c\omega_{0c}\tau_c}{\tau_R + \omega_{0a}\tau_a + \omega_{0c}\tau_c} \tag{3.2.32c}$$

where the subscripts R, g, a and c denote molecular Rayleigh scattering, gaseous absorption, and Mie scattering/absorption caused by aerosols and clouds, respectively.

The cloud optical properties are parameterized following Dobbie et al. (1999) for liquid droplets and Ebert and Curry (1992) for ice particles.

3.2.3.3 Gas Concentrations and Aerosol Climatology

The radiatively active gases considered in the radiation scheme are water vapor, ozone, carbon dioxide, oxygen, methane, nitrous oxide, CFC-11, CFC-12 and HCFC-22. Prognostic water vapor concentrations are used for the troposphere, while climatological distribution based on Randel et al. (1998) is used for areas above it. The

Table 3.2.2: Values of the globally uniform gas concentration (unit is ppmv).

CO_2	O_2	CH_4	N_2O	CFC-11	CFC-12	HCFC-22
396	209490	1.824	0.3259	0.0003	0.0005	0.0002

three-dimensional monthly mean climatology of ozone concentration is derived from the latest MRI CCM2 reanalysis (Deushi and Shibata 2011). Other radiatively active gases have globally uniform concentrations as shown in Table 3.2.2.

In the radiation scheme, five aerosol types (sulfate, black carbon, organic carbon, sea salt and mineral dust) are considered (Yabu *et al.* 2017). The three-dimensional monthly mean climatology of aerosol mass concentration is derived from aerosol CTM calculation (see Section 3.9), and the optical properties of these aerosols are pre-computed via Mie scattering calculation. The climatological distribution of total-column values for aerosol optical depth (ATOD) is used in combination. Monthly mean ATOD climatology is derived from Moderate Resolution Imaging Spectroradiometer (MODIS), Multi-angle Imaging Spectro-Radiometer (MISR) and Ozone Monitoring Instrument (OMI) observations.

3.2.3.4 Cloud Properties

Two types of cloud are considered in the radiation scheme. One is stratiform cloud, whose properties (such as cloud cover, cloud water content and cloud ice content) are provided by the cloud scheme. The other is convective cloud, whose properties are diagnosed using the upward convective mass flux calculated in the convection scheme. The effective radius of cloud liquid droplets $r_{e,liq}$ [μm] is parameterized based on Martin *et al.* (1994) as follows:

$$r_{e,liq} = 10^4 \left(\frac{3CWC}{4\pi\rho_w k N_{TOT}} \right)^{1/3} \tag{3.2.33}$$

where CWC is the cloud water content [gm^{-3}], N_{TOT} is the number concentration of water cloud droplets [cm^{-3}], ρ_w is the density of water [gm^{-3}] and k is a constant. N_{TOT} is set as 100 and 300 cm^{-3} over ocean and land areas, respectively. The effective radius of cloud ice particles $r_{e,ice}$ [μm] depends on temperature T [K] and cloud ice content IWC [gm^{-3}] as follows (Sun 2001):

$$f = 1.2351 + 0.0105(T - 273.15)$$
$$a = 45.8966\,\text{IWC}^{0.2214}$$
$$b = 0.7957\,\text{IWC}^{0.2535}$$
$$r = 0.838167 f\,[a + b(T - 83.15)]$$
$$r_{e,ice} = \min(\max(r, 13), 130). \tag{3.2.34}$$

3.2.4 Cumulus Convection

The GSM employs a spectral mass-flux convective parametrization scheme based on Arakawa and Schubert (1974) and Moorthi and Suarez (1992). Prognostic closure based on Randall and Pan (1993) is used, although many modifications are made to the original. In addition, a triggering mechanism based on the DCAPE concept (Xie and Zhang 2000) is adopted to suppress excessive convective activity. Convective downdraft, convective momentum transport and mid-level convection are also included in the scheme.

3.2.4.1 Convective Effect on Large-scale Variables

The convective effect on large-scale variables is estimated using the following equations:

$$\left(\rho \frac{\partial \overline{s}}{\partial t} \right)_{conv} = \sum_n D_n^u(s_n^u - \overline{s}) + D^d(s^d - \overline{s}) + \left(\sum_n M_n^u - M^d \right) \frac{\partial \overline{s}}{\partial z} - L_i c - L_v e - \delta E_s \tag{3.2.35}$$

$$\left(\rho \frac{\partial \overline{h}}{\partial t}\right)_{\text{conv}} = \sum_n D_n^u(h_n^u - \overline{h}) + D^d(h^d - \overline{h}) + \left(\sum_n M_n^u - M^d\right)\frac{\partial \overline{h}}{\partial z} - L_i c - \delta E_h \tag{3.2.36}$$

where ρ is the density of air, s and h are dry and moist static energy, D is detrainment to the environment, L_v and L_i are the latent heat of vaporization and melting, e is the evaporation amount under the convective cloud base, and c is the melt amount. Details of δE_s and δE_h are provided in Subsection 3.2.4.2. The over-bar denotes an environmental value, the superscripts u and d indicate updraft and downdraft respectively, and the subscript n indicates each plume of an ensemble of convection. Multiple plumes are considered for updraft, and a single plume is calculated for downdraft.

The first terms on the right of Eqs. (3.2.35) and (3.2.36) represent detrainment from updraft to the environment, the second terms indicate detrainment from downdraft to the environment, the third represent compensating subsidence, and the fourth represent the melting effect below freezing level. The fifth term in Eq. (3.2.35) denotes the evaporation effect under the cloud base.

3.2.4.2 Cloud Model

Based on Arakawa and Schubert (1974), the ensemble effect of multiple cumulus types is considered.

The mass flux of each plume is expressed as

$$M_n = M_{Bn}(t)\eta_n(z) \tag{3.2.37}$$

where M_B is the mass flux at the cloud base and η is the normalized cloud mass flux, which is 1 at the cloud base. The details of M_B calculation are provided in Subsection 3.2.4.3.

The cloud base of each plume is fixed near 900 hPa in the model. Each type of cumulus is defined by the level of the cloud top, where the updraft cloud mass loses buoyancy and detrainment occurs. The vertical profile of the upward mass flux η is assumed to be a linear function of height z, as proposed by Moorthi and Suarez (1992), and can be expressed as

$$\eta_n = 1 + \lambda_n(z - z_b) \tag{3.2.38}$$

where λ is the entrainment rate and z_b is the cloud base height. λ is diagnosed using a condition in which each plume loses buoyancy at its cloud top.

Cloud water content in the updraft is converted to precipitation, and the conversion is formulated as an autoconversion scheme as proposed by Kessler (1969).

The mass flux below the cloud base is calculated based on Jakob and Siebesma (2003):

$$\frac{\partial \eta}{\partial z} = \frac{C}{z}\eta \tag{3.2.39}$$

where C is a constant set to 0.5.

The plume ascends with the entrainment rate obtained from Eq. (3.2.39) below the cloud base. Assuming the occurrence of convection to be associated with positive subgrid scale fluctuations of temperature and moisture, air with higher dry and moist static energy than the grid-mean environment is entrained into the plume. δE_s and δE_h in Eqs. (3.2.35) and (3.2.36) represent the entrainment of excess energy to the updraft below the cloud base.

3.2.4.3 Closure

Closure is based on Randall and Pan (1993), and numerous modifications are made to the original scheme. For deep convection, the following prognostic equation is used to calculate the upward mass flux at the cloud base M_B for each plume (the subscript n is omitted for simplicity):

$$\frac{dM_B}{dt} = \max\left(\frac{A - fA_0}{2\alpha}, 0\right)\min\left(\frac{\lambda}{\lambda_{\min}}, 1\right)\max(\lambda_{\max}, 0)\left(\frac{\Delta p}{\Delta p_{\text{eff}}}\right) - \frac{M_B}{2\tau_d} \tag{3.2.40}$$

where A denotes the cloud work function, A_0 is the average of observed cloud work functions as given by Lord and Arakawa (1980), Δp is the depth of model cloud top layer, Δp_{eff} is the effective depth of the cloud top, and τ_d is the time constant of cumulus kinetic energy decay. The parameter f is introduced to incorporate the effects of grid-scale vertical wind and convective inhibition. This is given by

$$f = \frac{\omega}{\omega_0} + \frac{A_i}{A_{i0}} + c \tag{3.2.41}$$

where ω denotes the vertical pressure velocity at the lowest level, A_i represents the work involved in lifting the parcel to the level of free convection, and ω_0, A_{i0} and c are empirically determined constants. The constraint $0 \leqq f \leqq 2$ is imposed to ensure realistic tendency of M_B. In order to suppress tall cumuli in dry conditions and incorporate the effects of turbulence in the planetary boundary layer, the parameter $\lambda_{\min}$ is defined as follows:

$$\lambda_{\min} = \max\left(\frac{0.9 - \text{RH}}{0.2}, \ 10^{-3}\right)\frac{0.3}{5l_0} \tag{3.2.42}$$

where RH denotes the vertical mean of relative humidity between the cloud base and the cloud top, and l_0 represents the mixing length of the planetary boundary layer. The parameter $\lambda_{\max}$ is introduced to suppress tall cumuli with unnaturally large entrainment rates, and is defined as

$$\lambda_{\max} = \min\left(\frac{\lambda - \lambda_2}{\lambda_1 - \lambda_2}, \ 1\right) \tag{3.2.43}$$

where $\lambda_1 = a_1/(z_t - z_b)$, $\lambda_2 = a_2/(z_t - z_b)$, z_t is the cloud top height, and a_1 and a_2 are empirically determined constants.

For shallow convection, a simplified version of Eq. (3.2.40) is adopted for closure.

3.2.4.4 Triggering Mechanism

The convective triggering mechanism proposed by Xie and Zhang (2000) known as the dynamic CAPE generation rate (DCAPE) is used in the cumulus parameterization. DCAPE is defined as follows:

$$\text{DCAPE} = \left(\text{CAPE}\left(T^*, q^*\right) - \text{CAPE}\left(T, q\right)\right)/\Delta t \tag{3.2.44}$$

where T is the temperature, q is the specific humidity, and (T^*, q^*) are (T, q) plus the change caused by overall large-scale advection over a certain time period Δt (the integration time step used in the model). These values are equivalent to (T, q) just after dynamics calculation. CAPE is defined as

$$\text{CAPE} = \int_{z_{\text{LFC}}}^{z_{\text{LNB}}} g\frac{T_v^u - T_v}{T_v}dz \tag{3.2.45}$$

where z_{LFC} and z_{LNB} are the height of the level of free convection and that of neutral buoyancy, respectively, g is the acceleration of gravity, and T_v is the virtual temperature. The superscript u denotes a lifted air parcel. Deep convection is prohibited when DCAPE does not exceed an empirically determined critical value.

3.2.4.5 Convective Downdraft

For reasons of economy, only one type of downdraft is assumed, while many types are considered in the updraft scheme.

Downdraft is initiated at the level where the net upward mass flux is reduced to half that at the cloud base. The downdraft mass flux M^d at the cloud base is given by,

$$M^d = 0.4M_B \tag{3.2.46}$$

where M_B is the net mass flux at the cloud base of updraft as calculated using Eq. (3.2.40).

Entrainment from the environment is assumed to occur above the cloud base, while detrainment is assumed to occur both above and below it. The entrainment and detrainment rates are set to the same constant value above the cloud base, so that the mass flux of downdraft is constant with height.

3.2.4.6 Mid-level Convection

A mid-level convection scheme is incorporated to represent cumulus convection with a cloud base on a frontal system in the extratropics. The height of the cloud base is given by the maximum moist static energy level in the vertical column, and the cloud top is defined as the level where an air mass rising from the cloud base with a constant entrainment rate loses buoyancy. Closure employs a simpler form of Eq. (3.2.40).

3.2.4.7 Convective Momentum Transport

Convective momentum transport is parameterized in a different way from heat and moisture transport. A multiple plume model is adopted both for updraft and downdraft. The entrainment and detrainment rates are set to the same value both for updraft and downdraft between the cloud base and the cloud top, making each mass flux constant with altitude. The magnitude of each updraft M_{cn}^u is set to the mass flux at the cloud base in the heat and moisture transport scheme as calculated using Eq. (3.2.40), and the magnitude of the downdraft is set to $0.4 \times M_{cn}^u$.

3.2.4.8 Melting and Re-evaporation of Precipitation

Melting of snow is calculated below freezing level, with formulation similar to that of the cloud scheme (Eq. (3.2.57)). Re-evaporation of precipitation is considered below the cloud base. Related calculation is based on the equation used in the cloud scheme (Eq. (3.2.59)) with a minor modification.

3.2.5 Clouds and Large-scale Precipitation

Clouds are prognostically determined in a fashion similar to that proposed by Smith (1990). The simple statistical approach proposed by Sommeria and Deardorff (1977) is adopted for the calculation of cloud amounts and their water content.

3.2.5.1 Cloud Scheme

Representing conserved quantities in phase transition between water vapor and cloud water, the total water content (water vapor and cloud water) q_w and the liquid water temperature T_L are defined as follows:

$$q_w = q_v + q_c \tag{3.2.47}$$

$$T_L = T - \frac{L}{C_p} q_c \tag{3.2.48}$$

where q_v is specific humidity, q_c is cloud water content, T is temperature, L is the latent heat of condensation and C_p is specific heat at a constant pressure. In each grid box, q_w is assumed to vary due to unresolved atmospheric fluctuations having a probability distribution function with a top-hat shape. The cloud fraction C is given by the part of the grid box where q_w exceeds the saturation specific humidity q_s, and cloud water content is given as the condensation amount in the grid box:

$$C = \frac{a_L \left(\overline{q_w} - q_s \left(T_L \right) \right) + \Delta q_w}{2 \Delta q_w} \tag{3.2.49a}$$

$$q_c = C^2 \Delta q_w \tag{3.2.49b}$$

$$a_L = \frac{1}{1 + \frac{L}{C_p} \left(\frac{\partial q_s}{\partial T} \right)_{T=T_L}} \tag{3.2.49c}$$

where Δq_w is the maximum local deviation from the grid-box mean total water content $\overline{q_w}$, the overbar denotes an average over the grid box, and C is under the constraint $0 \leq C \leq 1$. Δq_w is calculated as follows:

$$\Delta q_w = \frac{a_L}{2} \left(\overline{q_w'^2} - 2b \, \overline{q_w' s_l'} + b^2 \overline{s_l'^2} \right)^{\frac{1}{2}} \tag{3.2.50}$$

68

where $s_l = C_p T_L + gz$ is dry static energy, g is acceleration under gravity, z is height above the surface, $b = \left(\frac{\partial q_s}{\partial T}\right)_{T=T_L} / C_p$, and the prime denotes a deviation from the grid average. $\overline{q_w'^2}$, $\overline{q_w' s_l'}$, and $\overline{s_l'^2}$ are calculated using the level 2 turbulence closure model of Mellor and Yamada (see Subsection 3.2.7) in the boundary layer scheme. Δq_w is limited by q_s:

$$0.2A\, a_L\, q_s\,(T_L) \quad \leq \quad \Delta q_w \quad \leq \quad 0.5A\, a_L\, q_s\,(T_L) \tag{3.2.51}$$

$$A \quad = \quad \min\left(\frac{p_s - p}{p_s - 850}, 1\right) \tag{3.2.52}$$

where p_s is surface pressure and p is pressure.

3.2.5.2 Stratocumulus Scheme

For the representation of subtropical marine stratocumulus clouds, the stratocumulus scheme proposed by Kawai and Inoue (2006) is adopted to diagnose the cloud fraction C and the cloud water content q_c instead of the cloud scheme:

$$C = 12.0\left(-\frac{\partial \theta}{\partial p} - 0.07\right) \tag{3.2.53a}$$

$$q_c = 0.05\, a_L\, C\, q_s \tag{3.2.53b}$$

where θ is the potential temperature. This scheme works when the following three conditions in each model layer and two conditions near the surface are satisfied:

[in each model layer]

- $-\frac{\partial \theta}{\partial p} > 0.07$ [K/hPa] (just above the model layer)
- relative humidity ≥ 80 [%]
- model layer height below the 924 hPa level

[near the surface]

- $-\frac{\partial \theta}{\partial p} < 0.01$ [K/hPa]
- not completely covered with sea ice

The first condition in each model layer represents the formation of marine stratocumulus clouds under a strong inversion layer, and the second and third prevent the false representation of stratocumulus clouds over dry area and shallow convection area, respectively. The conditions near the surface prevents the false representation of stratocumulus clouds over land or sea ice during the night.

In the cloud scheme and the stratocumulus scheme, liquid (ice) cloud is assumed to be present when the temperature is above $0°C$ (below $-15°C$). Between $-15°C$ and $0°C$, mixed-phase cloud is assumed to be present and the mixing ratio changes in a linear fashion with temperature.

3.2.5.3 Cloud Ice Fall and Conversion to Precipitation

The prognostic equation for cloud water content is as follows:

$$\frac{\partial q_c}{\partial t} = C_g + I - O \tag{3.2.54}$$

where C_g represents the generation rate of clouds in the grid box, I is the inflow from the upper layer, and O is the downward outflow. C_g is calculated using the results described in Subsection 3.2.5.1 or Subsection 3.2.5.2.

For ice-only cloud, I and O are calculated based on Kawai (2005). Small cloud particles ($\leq 100 \, \mu$m) fall into the lower layer, while large ones ($> 100 \, \mu$m) fall to the surface immediately as snow:

$$O = \frac{v_{cice} q_c}{\Delta z} + D_{I2S} q_c \tag{3.2.55}$$

where Δz is the layer thickness, v_{cice} is the terminal velocity of a small ice particle in cloud, and D_{I2S} is the conversion rate from ice cloud to snow. The first term on the right becomes I in the next layer down.

For mixed-phase cloud or water-only cloud, parameterization for the rate of conversion from cloud water to precipitation P follows the scheme proposed by Sundqvist (1978):

$$
\begin{aligned}
P &= \frac{1}{\tau_p} q_c \left[1 - \exp\left\{ -\left(\frac{q_c}{C q_c^{\text{crit}}} \right)^2 \right\} \right] \\
&= O
\end{aligned}
\tag{3.2.56}
$$

where τ_p represents a characteristic time scale for the conversion of cloud droplets into raindrops and snowflakes, and q_c^{crit} is the critical cloud water content at which the release of precipitation becomes efficient. In this case, I is not considered because raindrops and snowflakes are assumed to fall to the surface immediately. The coalescence process (collection of cloud droplets by raindrops falling through a cloud) and the Bergeron-Findeisen effect (enhancement of precipitation release in clouds containing a mixture of droplets and ice crystals) are modeled following Sundqvist *et al.* (1989).

3.2.5.4 Melting and Evaporation

The snow melting rate M is parameterized using the same method as ECMWF (2014):

$$M = 0.5 \frac{C_p}{L_m} \frac{T_w - T_0}{\tau_m} \tag{3.2.57}$$

$$\tau_m = \frac{7200}{1 + 0.5 (T_w - T_0)} \tag{3.2.58}$$

where T_w is the wet-bulb temperature, T_0 is the melting temperature, L_m is the latent heat of fusion, and τ_m is the relaxation time of melting. Based on Kessler (1969) and Tiedtke (1993), the evaporation rate E for large-scale precipitation is parameterized as

$$E = b \frac{1}{\tau_e} (q_s - q_v) \left\{ \left(\frac{p}{p_s} \right)^{1/2} \frac{1}{5.09 \times 10^{-3}} \frac{P_l}{b} \right\}^{0.577} \tag{3.2.59}$$

$$\frac{1}{\tau_e} = 5.44 \times 10^{-4} \tag{3.2.60}$$

where b is the clear-sky precipitation fraction (set to 0.5), τ_e is the relaxation time of evaporation, and P_l is the local precipitation rate.

3.2.6 Surface Turbulent Fluxes

Surface fluxes are represented with bulk formula based on Monin–Obukhov (M–O) similarity theory, with momentum flux F_m, heat flux F_h and specific humidity flux F_q expressed as follows:

$$F_m = \overline{(w' \mathbf{v}')}_s = -C_m |\mathbf{v}_1| \mathbf{v}_1 \, , \tag{3.2.61}$$

$$F_h = \overline{(w' \theta')}_s = -C_h |\mathbf{v}_1| (\theta_1 - \theta_s) \, , \tag{3.2.62}$$

$$F_q = \overline{(w' q')}_s = -C_h |\mathbf{v}_1| (q_1 - q_s) \, . \tag{3.2.63}$$

Here $\mathbf{v} = (u, v)$ represents horizontal wind, θ is potential temperature and q is specific humidity, and the subscripts "1" and "s" indicate variables at the lowest level of the model grid and at the ground surface, respectively. C_m and C_h are exchange coefficients for momentum and heat.

According to M–O similarity theory, the exchange coefficients are defined as follows:

$$\frac{z_1}{L} \frac{\left[\log\left(\frac{z_1+z_{0m}}{z_{0h}}\right) - \Psi_h\left(\frac{z_1+z_{0m}}{L}\right) + \Psi_h\left(\frac{z_{0h}}{L}\right)\right]}{\left[\log\left(\frac{z_1+z_{0m}}{z_{0m}}\right) - \Psi_m\left(\frac{z_1+z_{0m}}{L}\right) + \Psi_m\left(\frac{z_{0m}}{L}\right)\right]^2} = \frac{gz_1}{|\mathbf{v}_1|^2} \frac{2(\theta_{v1} - \theta_{vs})}{(\theta_1 + \theta_s)} \quad , \tag{3.2.64}$$

$$C_m = \frac{\kappa^2}{\left[\log\left(\frac{z_1+z_{0m}}{z_{0m}}\right) - \Psi_m\left(\frac{z_1+z_{0m}}{L}\right) + \Psi_m\left(\frac{z_{0m}}{L}\right)\right]^2} \quad , \tag{3.2.65}$$

$$C_h = \frac{\kappa^2}{\left[\log\left(\frac{z_1+z_{0m}}{z_{0m}}\right) - \Psi_m\left(\frac{z_1+z_{0m}}{L}\right) + \Psi_m\left(\frac{z_{0m}}{L}\right)\right]\left[\log\left(\frac{z_1+z_{0m}}{z_{0h}}\right) - \Psi_h\left(\frac{z_1+z_{0m}}{L}\right) + \Psi_h\left(\frac{z_{0h}}{L}\right)\right]} \quad , \tag{3.2.66}$$

where κ is von Kármán's constant (= 0.4), g is the standard acceleration due to gravity (= 9.80665 [m/s^2]), z_1 is the height of the lowest level of the model grid above the ground, and θ_v is the virtual potential temperature, while z_{0m} and z_{0h} are the surface momentum and heat roughness lengths, respectively. Eq. (3.2.64) gives Obukhov length L from the prognostic variables on right. The stability functions Ψ_m and Ψ_h are parameterized by Beljaars and Holtslag (1991) as follows:

$$x \equiv (1 - 16\xi)^{\frac{1}{4}} \tag{3.2.67}$$

$$\Psi_m(\xi) = \begin{cases} \dfrac{\pi}{2} - 2\arctan(x) + \log\dfrac{(1+x)^2(1+x^2)}{8} & \xi < 0 \\ -\dfrac{2}{3}\left(\xi - \dfrac{5}{0.35}\right)e^{-0.35\xi} - \xi - \dfrac{2}{3}\dfrac{5}{0.35} & \xi \ge 0 \end{cases} \quad , \tag{3.2.68}$$

$$\Psi_h(\xi) = \begin{cases} 2\log\dfrac{1+x^2}{2} & \xi < 0 \\ -\dfrac{2}{3}\left(\xi - \dfrac{5}{0.35}\right)e^{-0.35\xi} - \left(1 + \dfrac{2}{3}\xi\right)^{\frac{3}{2}} - \dfrac{2}{3}\dfrac{5}{0.35} + 1 & \xi \ge 0 \end{cases} \quad . \tag{3.2.69}$$

Over land grids, surface parameters are determined using the land model on each grid in consideration of vegetation type, soil conditions, and snow cover (Subsection 3.2.10). Over ocean grids, surface fluxes are calculated separately for the different subgrid surface fractions. Tiling between open water and sea ice is used with the coupling approach suggested by Best $et~al.$ (2004).

Surface wind stress depends on oceanic waves excited by surface winds. Roughness length and wind-induced stress are iteratively calculated in the model. Following the method of Beljaars (1995), surface roughness lengths over open sea (ice-free ocean) are determined from Charnock's relation (Charnock 1955):

$$z_{0m} = \frac{0.11\nu}{u_*} + \frac{\alpha}{g}u_*^2 \quad ,$$
$$z_{0h} = \frac{0.62\nu}{u_*} \quad , \tag{3.2.70}$$

where $u_*\left(\equiv \sqrt{|\overline{(w'\mathbf{v}')_s}|}\right)$ is the friction velocity, ν is the kinematic viscosity of air (= 1.5×10^{-5}m^2/s) and α is the Charnock coefficient (= 0.020). The surface roughness lengths over sea ice are fixed at 0.001m for momentum and 0.0005m for heat.

3.2.7　Boundary layer (turbulent transport)

A hybrid approach between turbulence kinetic energy (TKE) closure and eddy diffusivity (ED) type scheme is employed to parameterize vertical turbulent transports of momentum, heat and moisture in the atmosphere. The TKE scheme used is the level 2 turbulence closure approach of Mellor and Yamada (1974, 1982), and the

ED–type scheme involves the use of stability functions based on Han and Pan (2011). Turbulent transports are expressed as

$$\overline{w'\mathbf{v}'} = -\max(K_m^{TKE}, K_m^{ED})\frac{\partial \mathbf{v}}{\partial z} ,\tag{3.2.71}$$

$$\overline{w's_L'} = -\max(K_h^{TKE}, K_h^{ED})\frac{\partial s_L}{\partial z} ,\tag{3.2.72}$$

$$\overline{w'q_w'} = -\max(K_h^{TKE}, K_h^{ED})\frac{\partial q_w}{\partial z} ,\tag{3.2.73}$$

where $s_L(\equiv C_pT + gz - Lq_c)$ is the liquid water static energy, $q_w(\equiv q + q_c)$ is the total water content, the superscripts "TKE" and "ED" indicate the scheme types for calculating diffusion coefficients K, and the subscripts "m" and "h" indicate momentum and heat, respectively.

Following mixing-length theory, the diffusion coefficients of both schemes can be written as

$$K_m = l^2 \left|\frac{\partial \mathbf{v}}{\partial z}\right| f_m ,\tag{3.2.74}$$

$$K_h = l^2 \left|\frac{\partial \mathbf{v}}{\partial z}\right| f_h ,\tag{3.2.75}$$

where f_m and f_h are stability functions and the mixing length l is given according to Blackadar (1962) as

$$l = \frac{\kappa z}{1 + \kappa z/l_0},\tag{3.2.76}$$

where κ is von Kármán's constant (= 0.4).

In the TKE scheme, the mixing length l_0 is calculated from sub-grid scale orographic variances and the planetary boundary layer depth. l_0 is a constant equal to 50 m in the ED–type scheme.

The stability functions in the ED type scheme are functions of the gradient Richardson number R_i, given as

$$f_m^{ED} = \begin{cases} \dfrac{1 + 2.1R_i}{(1 + 5R_i)^{1.5}} & R_i \geq 0 \\ 1 - \dfrac{8R_i}{1 + 1.746\sqrt{-R_i}} & R_i < 0 \end{cases} ,\tag{3.2.77}$$

$$f_h^{ED} = \begin{cases} \dfrac{1}{(1 + 5R_i)^{1.5}} & R_i \geq 0 \\ 1 - \dfrac{8R_i}{1 + 1.286\sqrt{-R_i}} & R_i < 0 \end{cases} .\tag{3.2.78}$$

Those of the TKE scheme can be written as follows:

$$f_m^{TKE} = S_M\sqrt{B_1 S_M(1 - R_f)},\tag{3.2.79}$$

$$f_h^{TKE} = S_H\sqrt{B_1 S_M(1 - R_f)},\tag{3.2.80}$$

$$S_M = A_1 F_1 \frac{RF_1 - R_f}{A_2 F_2(RF_2 - R_f)}S_H,$$

$$S_H = 3A_2\frac{(\gamma_1 + \gamma_2)(RF_c - R_f)}{1 - R_f},$$

$$R_f = RI_1\left(\hat{R}_i + RI_2 - \sqrt{\hat{R}_i(\hat{R}_i - RI_3) + RI_2^2}\right),$$

$$RF_1 = B_1\frac{\gamma_1 - C_1}{F_1}, \quad RF_2 = B_1\frac{\gamma_1}{F_2}, \quad RF_c = \frac{\gamma_1}{(\gamma_1 + \gamma_2)},$$

$$RI_1 = \frac{1}{2}\frac{A_2 F_2}{A_1 F_1}, \quad RI_2 = B_1\gamma\frac{(\gamma_1 - C_1)}{F_1}\frac{A_1 F_1}{A_2 F_2}, \quad RI_3 = 4B_1\frac{\gamma_1}{F_2}\frac{A_1 F_1}{A_2 F_2} - 2RI_2,$$

$$F_1 = B_1(\gamma_1 - C_1) + 2A_1(3 - 2C_2) + 3A_2(1 - C_2), \quad F_2 = B_1(\gamma_1 + \gamma_2) - 3A_1(1 - C_2),$$

$$\gamma_1 = \frac{1}{3} - 2\frac{A_1}{B_1}, \quad \gamma_2 = \frac{B_2}{B_1}(1 - C_3) + 2\frac{A_1}{B_1}(3 - 2C_2),$$

where $A_1(= 1.0)$, $A_2(= 0.58)$, $B_1(= 24.0)$, $B_2(= 11.0)$, $C_1(= 0.13)$, $C_2(= 0.6)$, and $C_3(= 0.14)$ are the closure constants of the TKE scheme. The modified gradient Richardson number $\hat{R}_i$ used instead of R_i is defined after the method of Smith (1990):

$$\hat{R}_i = g \left\{ \tilde{\beta}_s \frac{\partial s_L}{\partial z} + \tilde{\beta}_Q \frac{\partial q_w}{\partial z} \right\} \Big/ \left| \frac{\partial \mathbf{v}}{\partial z} \right|^2, \tag{3.2.81}$$

where $\tilde{\beta}_s$ and $\tilde{\beta}_Q$ are buoyancy parameters in terms of the cloud-conserved quantities s_L and q_w, respectively.

3.2.8 Sub-grid Orography

The effect of orographic drag from sub-grid orography on atmospheric flow is separately parametrized depending on scales of unresolved orography. Gravity wave drag (GWD) from sub-grid orography with scales larger than 5 km (the minimum scale for vertically propagating gravity waves under typical conditions), and blocked flow drag (BFD) associated with the sub-grid orography are based on Lott and Miller (1997), and turbulent orographic form drag (TOFD) caused by sub-grid orography with scales smaller than this is parametrized in line with Beljaars *et al.* (2004a). For numerical stability, BFD and TOFD tendencies are implicitly computed via a tridiagonal solver in the boundary layer scheme by passing the linear coefficients, and the GWD tendency is passed to the solver as a forcing term (Subsection 3.2.8.5).

3.2.8.1 Turbulent Orographic Form Drag

TOFD formulation is based on the spectra of topography over North America and related integrals in the wavenumber space. An approximated equation is used for simplicity, and TOFD involves explicit application of drag on model levels in the equation for horizontal wind u (m s^{-1})

$$\frac{\partial u}{\partial t} = \frac{\partial}{\partial z} \frac{\tau_x}{\rho} = -C_{\text{tofd}} u|u|, \tag{3.2.82}$$

$$C_{\text{tofd}} = \alpha \beta C_{\text{md}} C_{\text{corr}} 2.109 e^{-(z/1500)^{1.5}} a_2 z^{-1.2}$$

where τ_x is stress (N m^{-2}) in the x-direction, ρ is atmospheric density (kg m^{-3}), z is geopotential height (m). $\alpha = 24$ and $\beta = 1$ are a shear-dependent parameter and a shape factor, respectively. $C_{\text{md}} = 0.005$ is a drag coefficient, $C_{\text{corr}} = 0.6$ is a correction parameter, $a_2 = a_1 k^{n_1-n_2}$, $a_1 = \sigma_{\text{flt}}^2 (I_H k_{\text{flt}}^{n_1})^{-1}$, $k_1 = 0.003$ (m^{-1}), $n_1 = -1.9$, $n_2 = -2.8$, $k_{\text{flt}} = 0.00035$ (m^{-1}), $I_H = 0.00102$ (m^{-1}) and σ_{flt} (m) is the standard deviation of filtered sub-grid orography. The same equation also holds for meridional wind v (m s^{-1}). For numerical stability, the equation is solved implicitly and simultaneously in the vertical diffusion scheme (Subsection 3.2.8.5).

The standard deviation of filtered sub-grid orography for TOFD, σ_{flt}, is calculated from two filtered fields where different scales are removed from a global $30'' \times 30''$ orographic source dataset (Kanehama *et al.* 2023b) (see Subsection 3.2.12). A smoothing filter is defined in the grid-point space by

$$h(r) = \begin{cases} \frac{1}{\Delta} & \text{for} \quad r \leq \Delta/2 - \delta \\ \frac{1}{2\Delta} + \frac{1}{2\Delta} \cos\left\{ \frac{\pi(r - \frac{\Delta}{2} + \delta)}{2\delta} \right\} & \text{for} \quad \Delta/2 - \delta < r < \Delta/2 + \delta \\ 0 & \text{for} \quad r \geq \Delta/2 + \delta \end{cases} \tag{3.2.83}$$

where r is radial distance (m), Δ is filter width (m) and δ is filter edge width (m). The parameter Δ controls extracting scales, and δ is applied to smooth data around the filter edge. To extract the necessary scales, the filter is applied twice to the source dataset. Filtering with $\Delta_1 = 2$ and $\delta_1 = 1$ is applied first to remove smaller scales smaller than 2 km (h_2), and with $\Delta_2 = 20$, $\delta_2 = 1$ is applied to extract scales larger than 20 km (h_{20}). The

smoothing functions with these parameters are displayed in Figure 3.2.1. The standard deviation of filtered orography σ_{flt} is calculated as

$$\sigma_{\text{flt}} = \sqrt{\sum_i w_i (d_i - \overline{d})^2 \bigg/ \sum_i w_i} \qquad (3.2.84)$$

where $d = h_2 - h_{20}$ and $\overline{d} = \sum_i w_i d_i / \sum_i w_i$, $w_i = \cos\phi$ is latitudinal weight, with ϕ being latitude, and summation over i is taken over all points within a model grid box. A map of the filtered standard deviation for TOFD at TQ959 is shown in Figure 3.2.2
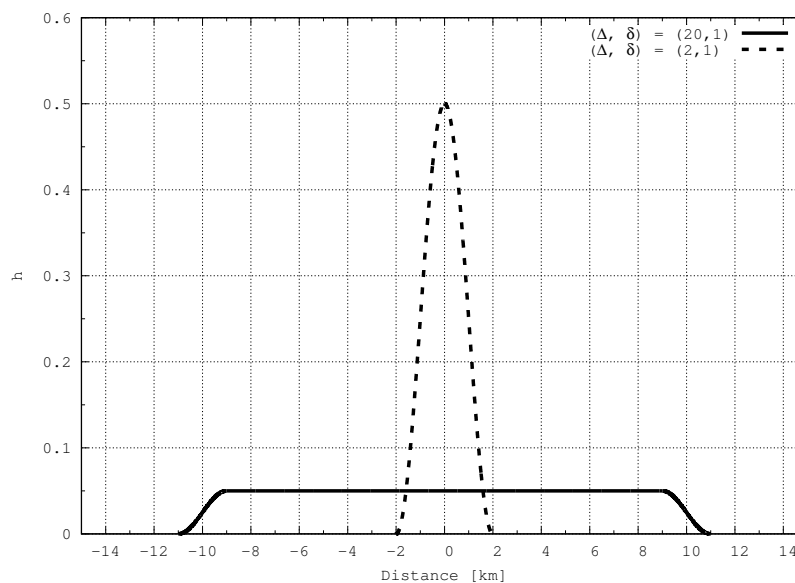
Figure 3.2.1: Shape of smoothing functions defined in Eq. (3.2.83) with the values of $(\Delta, \delta) = (20, 1)$ for the straight line and $(\Delta, \delta) = (2, 1)$ for the dotted line.
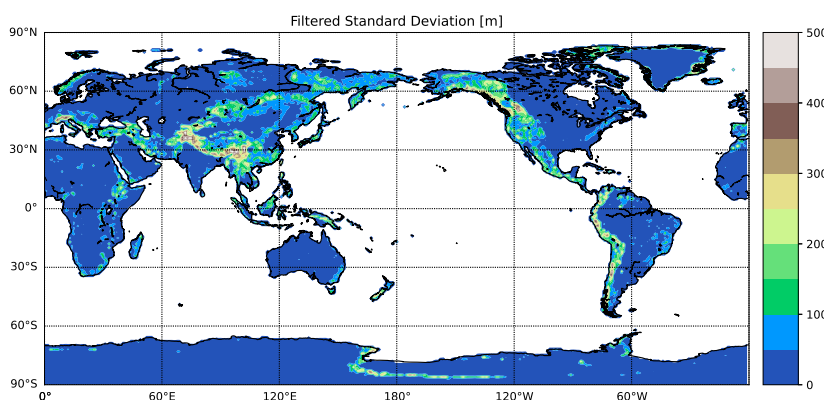
Figure 3.2.2: Filtered standard deviation [m] for TOFD at TQ959. Only land grid points are plotted.

3.2.8.2   Blocked Flow Drag

In the sub-grid scale orographic (SSO) drag scheme, it is assumed that the effect of sub-grid orography on atmospheric flow is equivalently represented by the effect of one elliptic mountain (Baines and Palmer 1990).

The scheme deals with two regimes, one is gravity wave drag exerted by topography, transporting momentum upwards and depositing momentum when breaking or filtering at a critical level. The other is a flow-blocking drag caused by flow going around, rather than over, orography. These two regimes are separated using non-dimensional mountain height as outlined below.

In the SSO scheme, it is assumed that flow is lateral when the non-dimensional mountain height is sufficiently high. This corresponds to high atmospheric stability, low incident flow speed, or mountain terrain high enough to suppress the flow crossing the elliptic mountain top. The maximum flow height associated with the blocking height Z_{blk} (m) is evaluated to satisfy inequality between non-dimensional mountain height and the critical value $H_{n_{\text{crit}}}$

$$\int_{Z_{\text{blk}}}^{H} \frac{N}{u_p} dz \geq H_{n_{\text{crit}}} \tag{3.2.85}$$

where N is Brunt-Vaisala frequency (s^{-1}), u_p is wind speed in the direction of incident flow (m s^{-1}), and z is geopotential height. H (m) is a statistical mountain height representing the peak sub-grid orography height, and is set as 3μ based on the standard deviation of sub-grid orography μ (m), and $H_{n_{\text{crit}}}$ is 0.5. Eq. (3.2.85) is evaluated from the top, and Z_{blk} is determined as the first level that satisfying this formula. The blocked flow drag D_{blk} is directly applied to model levels and formulated as

$$D_{\text{blk}}(z) = -C_d \max\left(5 - \frac{1}{r^3}, 0\right) \rho \frac{\sigma}{2\mu} \left(\frac{Z_{\text{blk}} - z}{z + \mu}\right)^{1/2} (B\cos^2\psi + C\sin^2\psi) \frac{u|u|}{2} \tag{3.2.86}$$

where C_d is a drag coefficient of 2. r is the aspect ratio of the elliptic mountain as seen from incident flow, ρ is air density, σ is the orographic slope along the short elliptic axis and ψ is the angle (rad) between incident flow with the angle φ and the principal axis of the elliptic with the angle θ, i.e., $\psi = \theta - \varphi$. Following Phillips (1984), B and C are

$$B = 1 - 0.18\gamma - 0.04\gamma^2, \quad C = 0.48\gamma + 0.30\gamma^2 \tag{3.2.87}$$

where γ is the elliptic aspect ratio. The aspect ratio seen from the incident flow r is formulated as

$$r = \sqrt{\frac{\cos^2\psi + \gamma^2\sin^2\psi}{\gamma^2\cos^2\psi + \sin^2\psi}} \tag{3.2.88}$$

The tendency of blocked flow drag is defined by

$$\frac{\partial u}{\partial t} = \frac{D_{\text{blk}}}{\rho} \tag{3.2.89}$$

The same equation applies for meridional wind v as well as zonal wind u. For numerical stability, it is solved implicitly and simultaneously in the vertical diffusion scheme (Subsection 3.2.8.5).

3.2.8.3 Gravity Wave Drag

The gravity wave drag part of the SSO scheme in Lott and Miller (1997) is similar to that proposed by Palmer et al. (1986), but is modified to represent the effects of anisotropic mountains (Baines and Palmer 1990). As flow under the Z_{blk} level is blocked by sub-grid elliptic mountains and is assumed to not cross mountain tops, the amplitude of gravity wave drag exerted by elliptic mountains is equal to the effective mountain height $H_{\text{eff}} = H - Z_{\text{blk}}$. The factor $n_{\text{eff}} = 1$ is applied to adjust gravity wave stress, i.e., $H_{\text{eff}} = n_{\text{eff}}(H - Z_{\text{blk}})$. Following Phillips (1984), gravity wave surface stress (τ_1, τ_2) parallel and perpendicular to incident flow can be formulated as

$$(\tau_1, \ \tau_2) = \rho_l|u_l|N_l\left(\frac{H_{\text{eff}}}{3}\right)^2 \frac{\sigma}{\mu} G\left\{B\cos^2\psi_l + C\sin^2\psi_l, \ (B - C)\sin\psi_l\cos\psi_l\right\} \tag{3.2.90}$$

where $G = 0.6$ is a function of mountain sharpness and the subscript l denotes the low-level mean between μ to 2μ. Note that Eq. (3.2.90) involves division by 9 rather than 4 as originally proposed in Lott and Miller (1997) so as to scale Eq. (3.2.90) with H being able to reach 3μ at its maximum when Z_{blk} is zero.

τ_{sfc}, the magnitude of stress at the wave generation level, is

$$\tau_{sfc} = \rho_l |u_l| N_l \left(\frac{H_{eff}}{3}\right)^2 \frac{\sigma}{\mu} G(D1^2 + D2^2)^{1/2}$$

$$D1 = B\cos^2\psi_l + C\sin^2\psi_l$$

$$D2 = (B - C)\sin\psi_l\cos\psi_l$$

(3.2.91)

For momentum deposit, the GWD scheme incorporates critical level filtering and wave saturation in upward propagation. Unless gravity waves encounter these processes, waves are assumed to propagate upward conservatively. When the background wind changes sign in propagating upward from the wave generation level, waves are assumed to reach a critical level and overall wave stress is deposited to the background.

The wave saturation process is implemented with comparison of surface stress (Eq. (3.2.91)) and saturated stress as per Palmer *et al.* (1986) and Iwasaki *et al.* (1989). Saturated stress τ_{sat} is estimated using the background Richardson number $R_i = N^2 / \left(\frac{\partial u}{\partial z}\right)^2$ and the local Richardson number $R_{i,loc}$. Assuming wave phase difference, the relationship between R_i and $R_{i,loc}$ is

$$R_{i,loc} = R_i \left(\frac{1 - \alpha}{(1 + R_i^{1/2}\alpha)^2}\right)$$

(3.2.92)

where $\alpha = N|\delta z|/V$, $|\delta z|$ is gravity wave amplitude (m) and V is wind speed (m s^{-1}) at a particular level in the direction of gravity wave stress. $R_{i,loc} = 0.25$ when the amplitude of gravity waves is saturated, and solving Eq. (3.2.92) with the saturated amplitude $|\delta z|_{sat}$ gives

$$|\delta z|_{sat} = \frac{V}{N} \left\{ 2(R_i^{-\frac{1}{2}} + 2)^{\frac{1}{2}} - (R_i^{-\frac{1}{2}} + 2) \right\}$$

(3.2.93)

Thus saturated flux τ_{sat} is

$$\tau_{sat} = \rho |u| N \left(\frac{H_{sat}}{3}\right)^2 \frac{\sigma}{\mu} G(D1^2 + D2^2)^{1/2}$$

(3.2.94)

with the effective amplitude H_{sat} as the saturated amplitude $H_{sat} = |\delta z|_{sat}$. τ_{sfc} and τ_{sat} are compared at each half level $k + 1/2$, and the residual momentum flux $\Delta\tau = \tau_{sfc} - \tau_{sat}$ is considered to be deposited to the background at the full level k if the condition $\tau_{sfc} > \tau_{sat}$ is satisfied. τ_{sat} is set as a new value for gravity wave stress propagating vertically. Otherwise, τ_{sfc} is considered to conservatively propagate vertically. The deposited momentum flux $\Delta\tau$ is distributed over a width equivalent to the diagnosed vertical wavelength λ_z (m) of hydrostatic gravity waves (Vosper 2015; Epifanio and Qian 2008).

$$\lambda_z = 2\pi \frac{u_1}{N}$$

(3.2.95)

where u_1 (m s^{-1}) is the wind component parallel to low-level wind. The tendency is

$$\frac{\partial u}{\partial t} = -\frac{1}{\rho} \frac{\partial \tau_\lambda}{\partial z}$$

(3.2.96)

where τ_λ is the sum of distributed deposited momentum flux. Distributing deposited momentum flux also increases numerical stability by inhibiting the GWD scheme to produce extremely large drag at a single level.

3.2.8.4 Ancillary Fields for Blocked Flow Drag and Gravity Wave Drag

In the Lott and Miller (1997) scheme, sub-grid orography is assumed to be represented by one elliptic mountain with standard deviation μ, orographic slope along the short axis σ, an aspect ratio γ and a long-axis angle θ.

As the scales included in SSO schemes are larger than 5 km (the minimum scale allowing vertical gravity wave propagation in typical conditions), scales smaller than this are removed by averaging the 30" (approx. 1 km) source dataset to a 2'30" resolution h_{org}, (approx. 5 km). The deviation of elevation (h) in the averaged 2'30" data from mean orography is defined as $h = h_{org} - h_m$, with h_m being grid-box mean orography, i.e., $h_m = \overline{h_{org}}$. Overlines indicate the grid-box mean, with orography linearly interpolated into 2'30" grid boxes in consideration of differences.

The parameters γ and θ are derived using variables K, L and M

$$K = \frac{1}{2}\left\{\overline{\left(\frac{\partial h}{\partial x}\right)^2} + \overline{\left(\frac{\partial h}{\partial y}\right)^2}\right\}, \; L = \frac{1}{2}\left\{\overline{\left(\frac{\partial h}{\partial x}\right)^2} - \overline{\left(\frac{\partial h}{\partial y}\right)^2}\right\}, \; M = \overline{\frac{\partial h}{\partial x}\frac{\partial h}{\partial y}} \tag{3.2.97}$$

Horizontal derivatives are computed in the grid-point space using adjacent grids in the latitudinal direction. However, in the longitudinal direction, equidistant points are computed via linear interpolation at each grid point in consideration of derivatives because the distance becomes smaller toward higher latitudes. The principal axis angle θ is computed using

$$\theta = \frac{1}{2}\arctan(M/L) \tag{3.2.98}$$

Applying coordinate transform with respect to θ gives coordinates along the short and long elliptic axes as

$$x' = x\cos\theta + y\sin\theta, \; y' = y\cos\theta - x\sin\theta \tag{3.2.99}$$

and the transformed coordinates involves introduction of new K', L' and M' values

$$K' = K, \; L' = (L^2 + M^2)^{1/2} \text{ and } M' = 0$$

The aspect ratio γ is defined as

$$\gamma^2 = \overline{\left(\frac{\partial h}{\partial y'}\right)^2} \Big/ \overline{\left(\frac{\partial h}{\partial x'}\right)^2} \tag{3.2.100}$$

$$= \frac{K' - L'}{K' + L'} = \frac{K - (L^2 + M^2)^{1/2}}{K + (L^2 + M^2)^{1/2}}$$

The orographic slope along the short-axis σ is defined by

$$\sigma^2 = \overline{\left(\frac{\partial h}{\partial x'}\right)^2} \tag{3.2.101}$$

and the standard deviation of sub-grid orography μ is computed as

$$\mu = \sqrt{\sum_i w_i(h_i - \overline{h})^2 \Big/ \sum_i w_i} \tag{3.2.102}$$

where $\overline{h} = \sum_i w_i h_i / \sum_i w_i$. Maps of the four parameters at TQ959 are shown in the Figure 3.2.3.

3.2.8.5 Joint Implicit Calculation

For numerical stability, Eq. (3.2.82) and Eq. (3.2.89) are solved implicitly, meaning that the absolute wind speed $|u|$ is taken from the current time step and the u and v components are evaluated at the next time step. The coefficient for the component at the new time level is passed to a tridiagonal implicit solver in the boundary layer and solved implicitly to increase consistency among multiple processes involved and further enhance numerical stability via time integration. The tendency for gravity wave drag is also passed to the solver as a forcing term so that the fast processes can adjust among multiple processes. By solving simultaneously, the

tendencies calculated via the solver in the boundary layer scheme include the planetary boundary layer (pbl), blocked flow drag (bfd), turbulent orographic form drag (tofd) and gravity wave drag (gwd). Among these, the tendency of gravity wave drag as a forcing term can be subtracted from total tendency. Accordingly, the implicitly computed tendency can be separated as

$$\left(\frac{\partial u}{\partial t}\right)_{\text{pbl+bfd+tofd}} = \left(\frac{\partial u}{\partial t}\right)_{\text{pbl+gwd+bfd+tofd}} - \left(\frac{\partial u}{\partial t}\right)_{\text{gwd}} \tag{3.2.103}$$

3.2.9 Non-orographic Gravity Wave Drag

The parameterization of non-orographic gravity wave drag follows the scheme proposed by Scinocca (2003). Assuming hydrostatic gravity waves in the absence of rotation, the vertical flux of momentum directed into the ϕ azimuth $\tilde{F}$ is expressed as follows:

$$\rho\tilde{F} = \rho A \frac{\tilde{c}-\tilde{U}}{N}\left(\frac{\tilde{c}-\tilde{U}}{\tilde{c}}\right)^{2-p} \frac{1}{1+\left[\frac{m^*(\tilde{c}-\tilde{U})}{N}\right]^{s+3}} \tag{3.2.104}$$

where,

$$A = Cm^{*3}\frac{N_0^{2-p}-f^{2-p}}{2-p} \tag{3.2.105}$$

ρ is density, $m^*(= 2\pi/2000 \text{ [1/m]})$ is the characteristic vertical wavenumber, N is the Brunt-Väisälä frequency, f is the Coriolis parameter, $p(=1.5)$ and $s(=1)$ are constants, $\tilde{c} = c - U_0^\phi$ and $\tilde{U} = U^\phi - U_0^\phi$, with c as the ground based phase speed and U^ϕ as the velocity in the direction of the azimuth ϕ, with the subscript 0 referring to the launch level.

The launch level is 450 hPa and the total launch momentum flux F_0 (corresponding to the integrated C in the phase speed direction) is formulated as a function of the latitude y [°]:

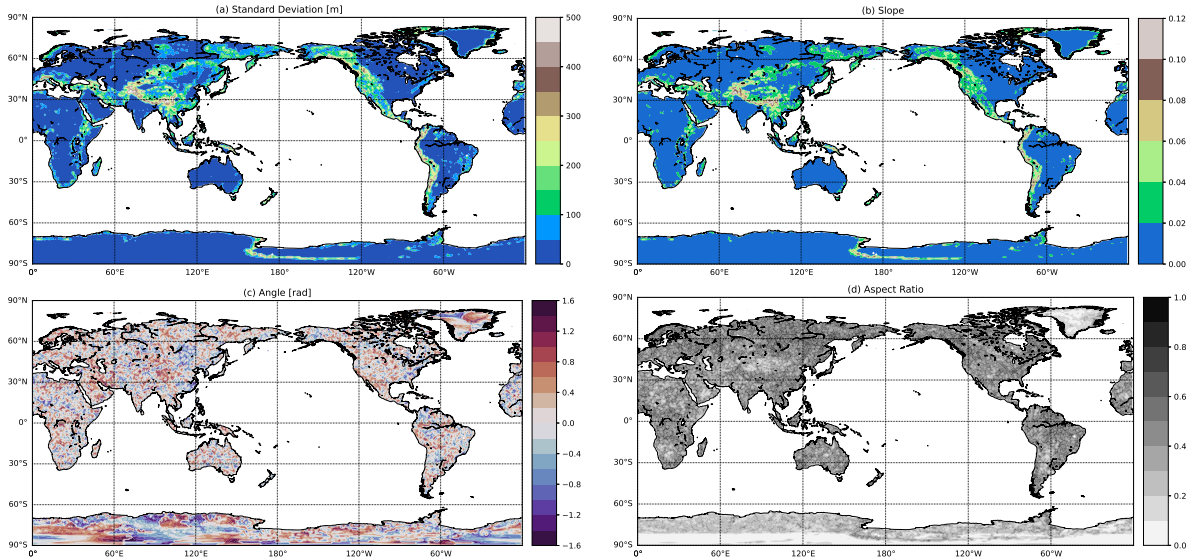$$F_0 = \rho_0 F_{\text{launch,bs}}\ \eta \tag{3.2.106}$$

Figure 3.2.3: The four parameters used in blocked flow drag and gravity wave drag parametrizations at TQ959, (a) standard deviation [m], (b) orographic slope, (c) angle [rad] and (d) aspect ratio. Note that only land grid points are plotted.

$$\eta = 1 - \left(1 - R_{\text{eq}}\right)\exp\left(-\left(\frac{y}{2w_{\text{eq}}}\right)^2\right) - \left(1 - R_{\text{pl}}\right)\exp\left(-\left(\frac{y - 90\text{sgn}(y)}{2w_{\text{pl}}}\right)^2\right) \quad (3.2.107)$$

$$R_{\text{eq}} = \frac{\rho_0 F_{\text{launch,eq}}}{\rho_0 F_{\text{launch,bs}}}, \ R_{\text{pl}} = \frac{\rho_0 F_{\text{launch,pl}}}{\rho_0 F_{\text{launch,bs}}} \quad (3.2.108)$$

where $\rho_0 F_{\text{launch,bs}} = 3.2 \times 10^{-3}$ Pa, $\rho_0 F_{\text{launch,eq}} = 1.8 \times 10^{-3}$ Pa, $\rho_0 F_{\text{launch,pl}} = 0.6 \times 10^{-3}$ Pa, $w_{\text{eq}} = 10°$ and $w_{\text{pl}} = 7.5°$.

The momentum fluxes are discretized in four equally spaced azimuths (north, south, west and east) and 50 phase speed bins in the range of 0.25 to 2000 m/s.

As momentum deposition processes, critical level filtering and nonlinear saturation are considered. In critical level filtering calculation, when $\tilde{c} - \tilde{U} < 0$ (assuming that waves encounter the critical level), the momentum flux is deposited to the mean flow in this layer. In nonlinear saturation calculation, when the upward propagating momentum flux $\rho\tilde{F}$ exceeds the saturated momentum flux $\rho\tilde{F}^{sat}$, the excess momentum flux $(\rho\tilde{F} - \rho\tilde{F}^{sat})$ is deposited to the mean flow. The saturated momentum flux is expressed as follows:

$$\rho\tilde{F}^{sat} = \rho C^* A \frac{\tilde{c} - \tilde{U}}{N}\left(\frac{\tilde{c} - \tilde{U}}{\tilde{c}}\right)^{2-p} \quad (3.2.109)$$

where $C^*(=10)$ is the tuning parameter introduced by McLandress and Scinocca (2005). These vertical momentum flux depositions are calculated at each level for each azimuthal direction and phase speed. To reduce the computational cost, parameterization is performed only once an hour.

3.2.10   Land Surface Processes

The land surface model in the GSM employs a two-layer energy balance scheme based on the Simple Biosphere scheme (SiB; Sellers *et al.* 1986; Sato *et al.* 1989). It has evolved to a complex representation for snow and soil, with reference to Oleson *et al.* (2010)

The model is composed of vegetation canopy, snow and soil components, each of which has its own variables of temperature, water and ice content. Canopy air space is used to express paths of heat and water transfer. Figure 3.2.4 shows heat and water flows in an analogy of an electric circuit.

3.2.10.1   Fluxes

The main role of the land surface model is to provide lower boundary conditions of fluxes to the atmospheric model. The zonal and meridional momentum fluxes $(\tau_x, \tau_y) \equiv \overline{(w'v')}_s$, sensible heat flux $H \equiv \overline{(w'\theta')}_s$, and water vapor flux $E \equiv \overline{(w'q')}_s$ are based on bulk formulae, as detailed in Subsection 3.2.6. Among these, τ_x and τ_y can be computed simply using the atmospheric wind velocity v_1, whereas determination of H and E requires the surface temperature and specific humidity values provided by the land surface model. This model in the GSM defines the values as "canopy air space temperature $T_a (= \theta_s)$ and specific humidity q_a", where sensible heat and water vapor fluxes from vegetation canopy and ground surface are connected.

Sensible heat H is balanced by the sum of sensible heats from the canopy H_c and the ground surface H_g, since canopy air space is assumed to have negligible heat and water vapor capacities,

$$H = H_c + H_g \quad (3.2.110)$$

Similarly, water vapor E is balanced by the sum of evaporations from the canopy E_c^e, the ground surface E_g^e and bare soil E_{bs}, as well as transpiration from the canopy E_c^t and the ground surface E_g^t

$$E = E_c^e + E_c^t + E_g^e + E_g^t + E_{bs} \quad (3.2.111)$$

These fluxes are determined with canopy temperature T_c and ground surface temperature T_g. Here, T_g represents grass or bare soil temperature, but is regarded as snow surface temperature when the ground surface is covered with snow.
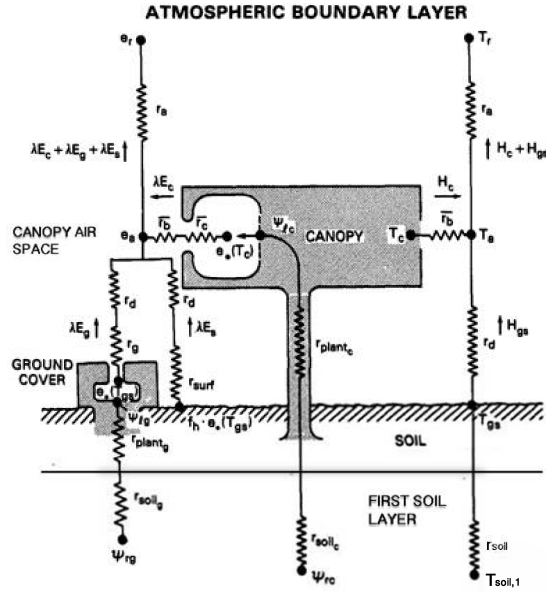
ATMOSPHERIC BOUNDARY LAYER

Figure 3.2.4: Schematic illustration of the land surface model (modified from Sellers *et al.* (1986)). Details are provided in the original paper.

3.2.10.2 Radiation and Albedo

The net radiation fluxes at the canopy R_c^n and the ground surface R_g^n are estimated based on the radiation balance equations

$$R_c^n = (1 - \alpha_c) S_{atm}^{\downarrow} + L_c^{\downarrow} \tag{3.2.112}$$

$$R_g^n = (1 - \alpha_g) S_{atm}^{\downarrow} + L_g^{\downarrow} \tag{3.2.113}$$

where α is the albedo, and $S_{atm}^{\downarrow}$ and $L^{\downarrow}$ are downward shortwave and longwave radiation from the atmosphere, respectively. In (3.2.112) and (3.2.113), R_c^n and R_g^n can be estimated using the albedos.

The surface albedo α_s can be determined as an average of the canopy albedo α_c and the ground albedo α_g, weighted by the fraction of canopy cover f_c

$$\alpha_s = f_c \alpha_c + (1 - f_c) \alpha_g \tag{3.2.114}$$

Similarly, the ground albedo α_g is an average of the grass albedo α_{grs} and the bare soil albedo α_{bs}, weighted by the fraction of grass cover f_{grs} in snow-free areas. When the ground is covered with snow, f_{grs} is set to zero, and α_{bs} is replaced by the value for snow α_{sn}

$$\alpha_g = \begin{cases} f_{grs} \alpha_{grs} + (1 - f_{grs}) \alpha_{bs} & \text{(snow-free)} \\ \alpha_{sn} & \text{(snow-covered)} \end{cases} \tag{3.2.115}$$

α_c and α_{grs} are calculated with radiative transfer equations (Sellers *et al.* 1986) for leaf and stem area. α_{bs} is provided from climatological data of the MODIS albedo product (Schaaf *et al.* 2002) and modified using the solar zenith angle and soil moisture near the soil surface. α_{sn} evolves with time, and is corrected using the solar zenith angle.

3.2.10.3 Energy and Water Balances

The prognostic equations for T_c and T_g are given as

$$C_c \frac{\partial T_c}{\partial t} = R_c^n - H_c - L_{vap} E_c \qquad (3.2.116)$$

$$C_g \frac{\partial T_g}{\partial t} = R_g^n - H_g - L_{vap} E_g - G_g \qquad (3.2.117)$$

where the subscripts c and g denote canopy and ground surface, respectively, C is heat capacity, R^n net radiation, L_{vap} latent heat of vaporization, G_g ground surface heat flux, and $E_c \equiv E_c^e + E_c^t$, $E_g \equiv E_g^e + E_g^t + E_{bs}$.

Water storage on canopy leaves M_c and grass leaves M_g, which are sources of evaporation, are predicted by

$$\frac{\partial M_c}{\partial t} = P_{i,c} - P_{d,c} - E_c^e \qquad (3.2.118)$$

$$\frac{\partial M_g}{\partial t} = P_{i,g} - P_{d,g} - E_g^e \qquad (3.2.119)$$

where P_i is precipitation intercepted by leaves, and P_d water drip falling from leaves. The difference between these two values, $I_{cept} = P_{i,c} + P_{i,g} - (P_{d,c} + P_{d,g})$, represents interception by canopy and grass. When T_c (T_g) is below the freezing point of water, M_c (M_g) represents ice on canopy or grass leaves.

3.2.10.4 Snow

Snow temperature T_{sn} is predicted based on the principle of energy conservation and Fourier's law of heat conduction

$$C_{sn} \frac{\partial T_{sn}}{\partial t} = \frac{\partial G_{sn}}{\partial z} \qquad (3.2.120)$$

$$G_{sn} = -\lambda_{sn} \frac{\partial T_{sn}}{\partial z} \qquad (3.2.121)$$

where the subscript sn denotes snow, G is heat flux (positive downward), z snow depth from the snow surface, and λ thermal conductivity. Using a multi-layer model, a snow column is discretized into up to four layers (Figure 3.2.5). The top boundary condition the ground surface heat flux, while the bottom boundary condition is conductive heat flux with the first soil layer

$$G_{sn,0} = G_g \qquad (3.2.122)$$

$$G_{sn,k_{max}} = \Lambda_{sn,k_{max}} \left(T_{sn,k_{max}} - T_{sl,1} \right) \qquad (3.2.123)$$

where the subscript sl denotes soil, and Λ is a thermal conduction coefficient. For integration in time t, implicit methods are adopted and tri-diagonal matrices are solved.

Snow mass M_{sn} is predicted based on the snow mass balance equation

$$\frac{\partial M_{sn}}{\partial t} = S_{fall} + \left(S_{frst} - S_{sub} \right) + \left(S_{frz} - S_{melt} \right) \qquad (3.2.124)$$

where S_{fall} is snowfall reaching the snow surface, including ice drip falling from leaves, S_{frst} frost, S_{frz} freezing, S_{sub} sublimation, and S_{melt} snowmelt.

Liquid water content in snow W_{sn} is predicted using

$$\frac{\partial W_{sn}}{\partial t} = \left(Q_{sn,infl} - Q_{sn,drng} \right) + \left(S_{dew} - S_{evap} \right) - \left(S_{frz} - S_{melt} \right) \qquad (3.2.125)$$

where $Q_{sn,infl}$ is infiltration into snow including rainfall and water drip falling from leaves, $Q_{sn,drng}$ gravitational drainage from the bottom, and S_{dew} liquid dew, S_{evap} evaporation. Snow mass and snow water content are predicted using the same k_{max} layers as those for the snow temperature. When snow water content in a layer exceeds the layer's holding capacity, excess water is moved to the underlying layer. Snow depth data from Snow Depth Analysis (see Section 2.8) are used to set the initial value of snow water equivalent.
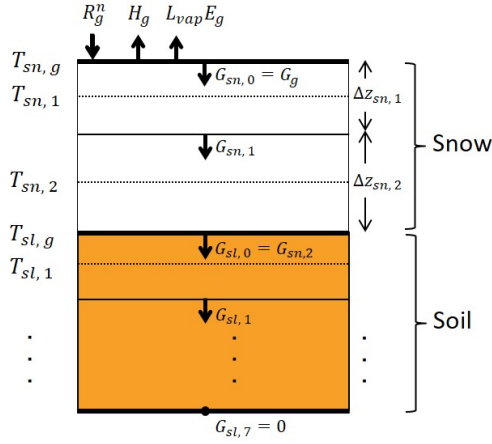
Figure 3.2.5: Schematic diagram of numerical discretization used to solve for snow temperatures $T_{sn,k}$ with two snow layers on top of soil. The subscripts sn, sl and k denote snow, soil and the k-th layer, respectively.
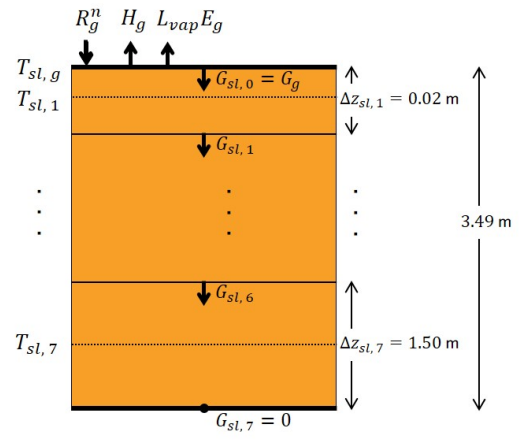
Figure 3.2.6: Schematic diagram of numerical discretization used to solve for soil temperatures $T_{sl,k}$ in snow-free areas.

3.2.10.5 Soil

Soil temperature T_{sl} is predicted in the same way as snow temperature, and soil is discretized into seven layers (Figure 3.2.6) of soil thicknesses $\Delta z_{sl,1-7}$ (m) = (0.02, 0.05, 0.12, 0.3, 0.5, 1.0, 1.5). The boundary conditions are

$$G_{sl,0} = \begin{cases} G_g & \text{(snow-free)} \\ \Lambda_{sl,k_{max}} \left(T_{sn,k_{max}} - T_{sl,1} \right) & \text{(snow-covered)} \end{cases} \tag{3.2.126}$$

$$G_{sl,7} = 0 \tag{3.2.127}$$

Soil moisture is predicted using Richard's equation, and root extraction for transpiration is also considered. The prognostic equation for the degree of saturation W is as follows:

$$\frac{\partial W}{\partial t} = \frac{1}{\rho_{wtr} \, \theta_{sat}} \left(-\frac{\partial Q}{\partial z} - S^t \right) \tag{3.2.128}$$

where ρ_{wtr} is water density, θ_{sat} soil porosity, Q water flux caused by differences in matric potential and gravitational potential, and S^t root extraction for transpiration. The top water flux is $Q_{infl} - E_{bs}$, where Q_{infl} is infiltration into soil including precipitation, drip falling from leaves and snowmelt, and the bottom is gravitational drainage Q_{drng}.

Surface runoff R_{off} and gravitational drainage Q_{drng} are counted as total runoff R_{total}

$$R_{total} = R_{off} + Q_{drng} \tag{3.2.129}$$

$$= T_{fall} - \left(Q_{infl} - Q_{drng} \right) - \left(Q_{sn,infl} - Q_{sn,drng} \right) \tag{3.2.130}$$

where

$$R_{off} = T_{fall} - Q_{infl} - \left(Q_{sn,infl} - Q_{sn,drng} \right) \tag{3.2.131}$$

$$T_{fall} = P_g - I_{cept} \tag{3.2.132}$$

P_g is gross rainfall, and T_{fall} throughfall reaching the ground surface. Q_{infl} is limited due to the maximum surface infiltration capacity.

3.2.10.6 Datasets

The climatological data of base soil albedo is derived from the MODIS albedo product[2] of NASA (Schaaf *et al.* 2002).

Each grid point on land is classified by a specific vegetation type provided from GLC2000[3] (Global Land Cover 2000; Bartholomé and Belward 2005) of the European Commission's Joint Research Center (JRC). The LAI (Leaf Area Index) is based on the MODIS LAI product[4] of NASA (Myneni *et al.* 2002). Fractions of canopy and grass covers are calculated using the 1 km MODIS-based Maximum Green Vegetation Fraction of USGS (Broxton *et al.* 2014a), the 1 km Tree Cover Continuous Fields product of GLCF (DeFries *et al.* 2000), and the Cropland and Pasture Area fraction[5] of EarthStat (Ramankutty *et al.* 2008).

The initial condition for soil moisture below the fourth soil layer is given by climatological data calculated using an offline model with the atmospheric forcing dataset of GSWP3 (Global Soil Wetness Project Phase 3; Kim 2017)[6]. The soil property is from HWSD (Harmonized World Soil Database; FAO *et al.* 2012).

3.2.11 Parallelization

In the GSM, Open Multiprocessing (OpenMP) is employed for shared memory parallelization, and the Message Passing Interface (MPI) is used for distributed memory parallelization. A two-dimensional decomposition method is adopted for parallelization among processes.

Figure 3.2.7 shows the schematic design of parallelization. There are five computational stages, and appropriate decompositions are selected in each stage. The base is the Grid stage. The Fourier and Legendre stages are used for calculating spherical harmonic transformation, and the Wavenumber stage is used for calculating Helmholtz equations in the semi-implicit scheme. The Horizontal Advection stage is used in the implementation of the semi-Lagrangian advection scheme.

At the Grid stage, since all vertical levels exist in a same rank for the computation of physical processes and non-linear terms of dynamical processes, variable arrays are decomposed into east-west and north-south directions. North-south decomposition follows a cyclic order, and is applied in such a way that the order of ranking is reversed alternately. This helps to mitigate load imbalances associated with physical parameterization and the number of grid points, since their computational loads depend mainly on latitudinal zones. At the Fourier stage, since all east-west grid points exist in a same rank for the performance of Fourier transformation, variable arrays are decomposed into north-south and vertical directions. At the Legendre stage, since all north-south grid points exist in a same rank for the performance of Legendre transformation, variable arrays are decomposed into vertical and longitudinal wavenumber directions. At the Wavenumber stage, since all vertical levels exist in a same rank for solving Helmholtz equations in the semi-implicit scheme, variable arrays are decomposed into longitudinal and total wavenumber directions. Communication among these four stages can be performed independently within each subset based on the provision of two restrictions for the number of decompositions: 1) the number of decompositions for the east-west direction, the vertical direction and the total wavenumber direction must be the same, and 2) the number of decompositions for the north-south direction and the longitudinal wavenumber direction must be the same.

At the Horizontal Advection stage, variable arrays are decomposed into vertical and north-south directions. To reduce the amount of communication relating to halo regions, the number of decompositions for the north-south direction is made as small as possible. Unlike communication in the stages described above, global communication is required for interaction between the Grid stage and the Horizontal Advection stage.

---

[2]https://search.earthdata.nasa.gov/search
[3]http://forobs.jrc.ec.europa.eu/products/glc2000/glc2000.php
[4]https://search.earthdata.nasa.gov/search
[5]http://www.earthstat.org/cropland-pasture-area-2000/
[6]http://hydro.iis.u-tokyo.ac.jp/GSWP3/index.html, https://www.isimip.org/gettingstarted/details/4/
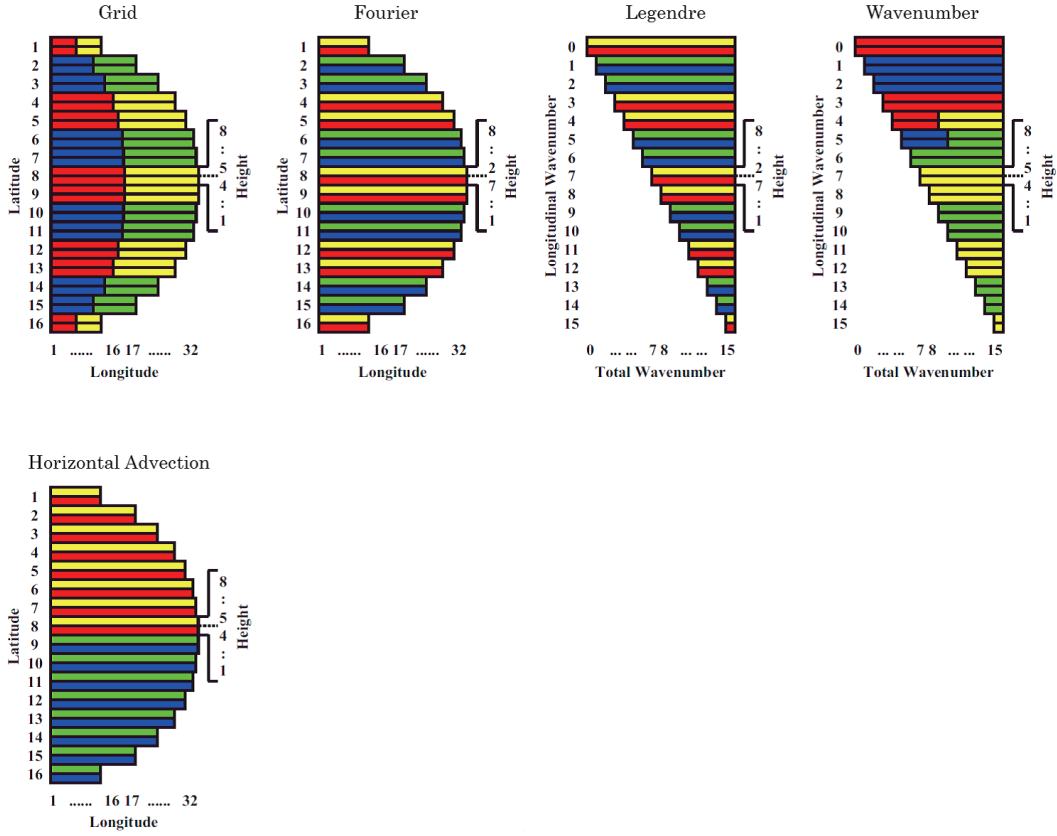
Figure 3.2.7: Schematic design of the parallelization. The number of processes used is assumed to be 4 in this example. Colors in the figure represent the rank for the computation in that area; red is rank 0, yellow is rank 1, blue is rank 2 and green is rank 3.

3.2.12 Surface Specifications

3.2.12.1 Orography

Model orography in the GSM is based on combined Global 30 Arcsecond lat-lon grid elevation orographic data generated using an average operation from the MERIT DEM (Yamazaki and D. Ikeshima 2017) dataset covering the 90° N – 60° S region and the RAMP2 (Liu *et al.* 2015) dataset covering 60° S – 90° S (Kanehama *et al.* 2023c). These combined elevation data are interpolated onto the reduced Gaussian grid after smoothing by multiplying the spectral coefficients by

$$f(n) = \left\{ \left(1 + df \left(\frac{n(n+1)}{N(N+1)} \right)^2 \right) \left(1 + 4.0 \left(\frac{n(n+1)}{N(N+1)} \right)^8 \right) \right\}^{-1}, \tag{3.2.133}$$

where n is the total wavenumber, N is the truncation total wavenumber, and $df = 0.866033186407302$ is a tunable smoothing parameter.

3.2.12.2 Grid Type

Land-ocean distribution is determined in reference to the Global Land Cover Characteristics (GLCC) database (Loveland *et al.* 2000) compiled by USGS and others. Model grid sections in which the land area ratio is more than 49% in GLCC are regarded as land grids in the GSM to keep the same global ocean area ratio as

GLCC. Grids not defined as land are sea (ocean) types and can have two tiles fractions (open water and ice). Inland water grids are treated as sea. Meanwhile, each land grid has a particular vegetation type based on the Global Land Cover 2000 database provided by the European Commission's Joint Research Centre in 2003. See Subsection 3.2.10 for the surface properties of land grids.

3.2.12.3   Sea and Lake Surfaces

On sea grids in the GSM, sea surface temperature (SST) and sea ice concentration (SIC) are given as boundary conditions minimally affected by the atmosphere. The amount of change in these variables during the time-integration of the model is equivalent to the time interpolated variation in daily climatological data.

On lake grids, monthly climatology based on the MODIS/Aqua product (Wan 2014) is used for water surface temperature. Lake ice concentration (LIC) is diagnosed from the surface temperature (T) using

$$
\text{LIC} = \begin{cases} 0 & T \geq 273.15 \\ 1 - \exp(0.1(T - 273.15)) & T < 273.15 \,. \end{cases}
$$

(3.2.134)

The direct beam albedo α_B of water surfaces is basded on Briegleb $et\ al.$ (1986):

$$
\alpha_B = \frac{0.026}{(\mu^{1.7} + 0.065)} + 0.15(\mu - 0.1)(\mu - 0.5)(\mu - 1.0) \,,
$$

(3.2.135)

where μ is the cosine of the solar zenith angle. The diffused albedo α_D is constant (= 0.06).

3.2.12.4   Sea and Lake Ice

The ice fraction is modelled as a slab with open water underneath and a skin temperature for thermal contact with the lowest part of the atmosphere. Sea ice parameterization involves (i) a fixed slab depth (with a constant volume regardless of melting), (ii) homogeneous and constant slab material properties, and (iii) climatological snow accumulation on the ice. Ice heat transfer is assumed to obey the Fourier law of diffusion:

$$
(\rho C)\frac{\partial T_{ice}}{\partial t} = \frac{\partial}{\partial z}\left(\lambda\frac{\partial T_{ice}}{\partial z}\right) \,,
$$

(3.2.136)

where $\rho C = 1.93 \times 10^6$ [Jm^{-3}K^{-1}] is volumetric ice heat capacity, T_{ice} is ice temperature, and $\lambda = 2.03$ [Wm^{-1}K^{-1}] is ice thermal conductivity. As a sea ice boundary condition, the temperature at the bottom of the slab is given as $T_{ice} = 271.51$K. The temperature at the top of the slab is diagnosed from the net heat flux at the top skin. The lake ice boundary condition at the bottom is the temperature of frozen water ($T_{ice} = 273.15$K), and the top boundary condition is the same as for sea ice. In the GSM, the ice slab is vertically discretized into four layers, with the temperature at each level solved via implicit time-integration.

The effect of snow over ice on the surface albedo is climatologically parameterized based on Hunke and Lipscomb (2006). The albedos of ice (α_{ice}) and snow (α_{snw}) depend on the surface temperature T_{skin}:

$$
\alpha_{ice} = \begin{cases} \alpha_{ice0} & T_{skin} < 272.15 \\ \alpha_{ice0} - 0.075(T - 272.15) & T_{skin} \geq 272.15 \end{cases} \,,
$$

$$
\alpha_{snw} = \begin{cases} \alpha_{snw0} & T_{skin} < 272.15 \\ \alpha_{snw0} - k(T_{skin} - 272.15) & T_{skin} \geq 272.15 \end{cases} \,,
$$

(3.2.137)

where T_{skin} is the surface temperature, α_{ice0} for visible is 0.78 and for near infrared is 0.36, α_{snw0} and k are 0.98 and 0.1 for visible, and 0.7 and 0.15 for near infrared. The total albedo is the area-weighted average of ice and snow albedos.

3.2.13   Initial Conditions

Initial conditions of subsystems such as the atmosphere and land are required for GSM time integration. The specifications of these are detailed in Table 3.2.3, where the term "forecast guess" represents the use of forecast variables with a lead time of six hours. However, land and snow variables are adjusted via snow analysis for consistency.

Table 3.2.3: Initial Conditions of GSM

Subsystem	Variable	Origin
Atmosphere	Zonal wind	4D-Var global objective analysis (see Section 2.5)
	Meridional wind	
	Temperature	
	Specific humidity	
	Surface pressure	
	Cloud water content	Forecast guess
	Diagnosed cloud water content in convection updraft	
	Cloud cover of stratiformis and convective cloud	
	Convective mass flux at cloud base	
Land surface	Grass (or bare soil) temperature	Forecast guess
	Canopy temperature	
	Liquid and ice water content on vegetation	
Land soil	Temperature	
	Liquid and ice water content in voids	Soil moisture analysis (see Section 2.9) and Climatological values in the deep layers
Snow	Snow water equivalent	Snow analysis (see Subsection 2.8.1)
	Temperature	Forecast guess
	Density	
	Liquid water content in voids	
	Albedo	
	Age	
Sea ice	Ice concentration	Sea ice analysis (see Section 5.6)
	Temperature	Forecast guess
Sea surface	Sea surface temperature	SST analysis (see Section 5.2)
	Friction velocity	Forecast guess
Lake ice	Temperature	Forecast guess

3.2.14 Forecast Performance

Figure 3.2.8 shows the root mean square error (RMSE) for 24-, 72- and 120-hour forecasts of 500 hPa geopotential height against analysis in the Northern Hemisphere extra-tropics. Dashed lines indicate monthly means, and solid lines represent 12-month running means. There are decreasing trends in RMSEs corresponding to GSM changes (see Subsection 3.2.1), although the impact of the changes in recent years has been relatively small.

Tropical cyclone (TC) track predictions are verified against the best track as analyzed by JMA's RSMC Tokyo - Typhoon Center. The mean position error of GSM TC track predictions in the western North Pacific (Figure 3.2.9) exhibits a gradual reduction from 1996 to 2022 due to GSM improvements, but considerable inter-annual variations are seen in 72-hour forecast errors and elsewhere.
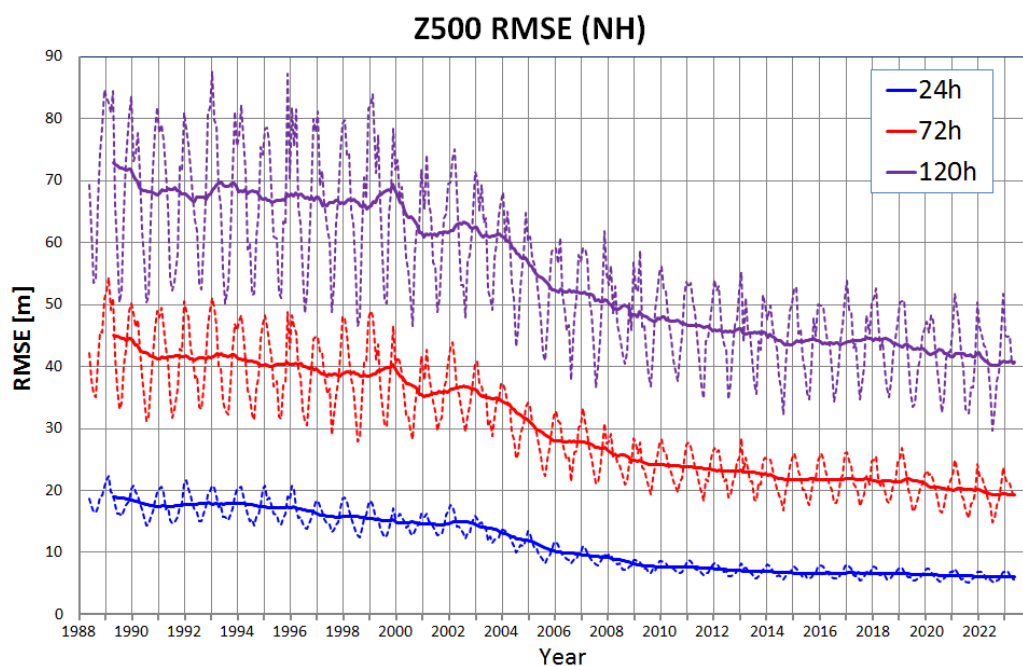

Figure 3.2.8: Root mean square error of GSM 500 hPa geopotential height (Z500) predictions against analysis in the Northern Hemisphere extra-tropics (20°N − 90°N). Dashed lines indicate monthly means, and solid lines represent running means calculated for the previous 12 months.
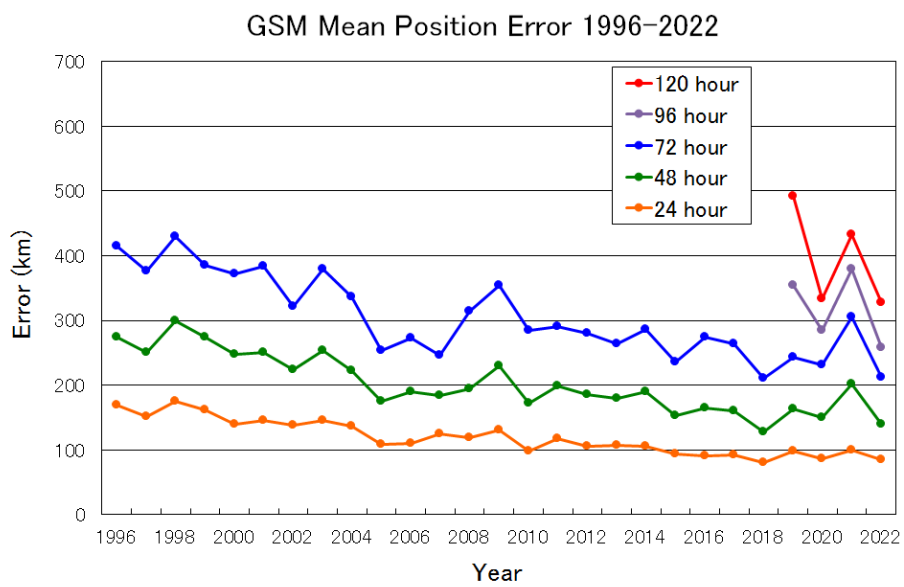
GSM Mean Position Error 1996–2022

Figure 3.2.9: Mean position error of GSM TC track predictions in the western North Pacific from 1996 to 2022. The lines represent 24- (orange), 48- (green), 72- (blue), 96- (purple), and 120-hour forecasts (red).

3.3 Global Ensemble Prediction System

3.3.1 Introduction

The Global Ensemble Prediction System (Global EPS), which has been operational since January 2017, produces forecasts with lead times of up to 34 days to support the issuance of Five-day Tropical Cyclone (TC) Forecasts, One-week Forecasts, Two-week Temperature Forecasts, Early Warning Information on Extreme Weather, and One-month Forecasts. The system took over the roles of JMA's previous Typhoon EPS, One-week EPS and One-month EPS (JMA 2013, 2017; Yamaguchi et al. 2014; Hirai et al. 2014), thereby helping to reduce computational cost and focus resource development on a single EPS. The Typhoon EPS and One-week EPS were replaced by the Global EPS in January 2017, and the system inherited the roles of the One-month EPS in March 2017. In March 2019, initial perturbations of the Global EPS were upgraded to incorporate the usage of perturbations from the six-hour forecast ensemble based on the Local Ensemble Transform Kalman Filter (LETKF) of the previous analysis instead of analysis perturbations (Ota et al. 2019). In March 2020, a major upgrade in the Global EPS was implemented, which incorporated improvements in the forecast model, a two-tiered sea surface temperature (SST) approach and direct application of initial perturbations from JMA's hybrid data assimilation system (Yamaguchi et al. 2020). In March 2021, another major upgrade was implemented to incorporate more levels in the forecast model, increased ensemble size and improved initial perturbations (Yamaguchi et al. 2021). In March 2022, the effective horizontal resolution of the forecast model was enhanced to approximately 27 km for forecasts of up to 18 days, and to 40 km thereafter, with the introduction of a quadratic grid. SST boundary conditions were also upgraded (Yamaguchi et al. 2022; Sekiguchi et al. 2022). The forecast model was further upgraded in March 2023, with a two-tiered SST approach expanded to the whole globe (Ota et al. 2023; Yamaguchi et al. 2023).

3.3.2 System

3.3.2.1 Configuration, and Initial and Boundary Conditions

The specifications of the Global EPS are shown in Table 3.3.1.

A low-resolution version of JMA's Global Spectral Model (GSM; Section 3.2) is used in the EPS. Accordingly, the dynamical framework and physical processes involved are essentially identical to those of the GSM except for a lower horizontal resolution, which is further reduced after a lead time of 18 days. Unperturbed initial conditions are based on interpolation of the global analysis field (Section 2.5). A two-tiered SST approach (Takakura and Komori 2020) combining anomaly-fixed SSTs (Subsection 3.2.12) with SST prediction from the Seasonal EPS (Section 3.4) is used for the lower-boundary condition. Sea ice concentration (SIC) for the lower-boundary condition is the climatological value with the daily analysis anomaly. For the first 14 forecast days, SIC anomaly and sea ice extent anomaly are largely maintained. Thereafter, the SIC anomaly is adjusted to maintain the sea ice extent anomaly.

When a forecast is used for issuing Two-week Temperature Forecasts, Early Warning Information on Extreme Weather and One-month Forecasts, systematic biases estimated from hindcast experiments (Subsection 3.3.6.3) are removed.

3.3.2.2 Ensemble Size, Forecast Range and Frequency

The Global EPS, which consists of 50 perturbed members and a control, is run daily with initial times of 00, 06, 12 and 18 UTC. 00 UTC has a forecast range of 11 days, with data used for One-week Forecasts. The 12 UTC run on Tuesdays and Wednesdays is extended to 34 days and on other days to 18 days. After the 18-day lead time, the ensemble size is reduced to 25 per initial time. A 50-member ensemble is composed using lagged averaged forecasting (LAF; Hoffman and Kalnay 1983) from 25-member ensemble forecasts with two consecutive initial times. The 12 UTC runs are also used for daily Two-week Temperature Forecasts, and for Early Warning Information on Extreme Weather issued on Mondays and Thursdays when high probability in data for seven-day averages of very high/very low temperatures or heavy snow is expected for the week starting five to eight days ahead of issuance. A 50-member lagged ensemble with a one-month forecast range is used

Table 3.3.1: JMA Global EPS specifications

Start of operation (Latest major implementation)	January 2017 (March 2023)
Initial time	00, 06, 12 and 18 UTC
Forecast range	Initial time 00 UTC: 11 days Initial time 12 UTC: 34 days on Tuesdays and Wednesdays, 18 days otherwise Initial time 06 and 18 UTC: 132 hours
Ensemble size	Forecasts up to 18 days: 51 members Longer forecasts: 25 members (50-member lagged ensemble with 2 initial times)
Model type	GSM (an atmospheric general circulation model)
Horizontal resolution	Forecasts up to 18 days: Spectral triangular 479 (TQ479), reduced Gaussian grid system, roughly equivalent to $0.25° \times 0.25°$ (27 km) in latitude and longitude Longer forecasts: Spectral triangular 319 (TQ319), reduced Gaussian grid system, roughly equivalent to $0.375° \times 0.375°$ (40 km) in latitude and longitude
Vertical resolution (model top)	128 stretched sigma pressure hybrid levels (0.01 hPa)
Integration time step	Forecasts up to 18 days: 600 seconds Longer forecasts: 720 seconds
Initial perturbation generator	SV method, LETKF and LAF method
Initially perturbed area	Global
Model ensemble method	Stochastic physics scheme
Surface boundary conditions	SST: Two-tiered SST
Surface boundary perturbations	SST perturbations

for One-month Forecasts issued on Thursdays. Runs initialized at 06 and 18 UTC with a forecast range of 132 hours are used for Five-day Tropical Cyclone Forecasts in addition to runs with initial times at 00 and 12 UTC.

3.3.3   Initial Ensemble Perturbations

The initial perturbation of the Global EPS is generated by adding perturbations calculated using the singular vector (SV) method (Buizza and Palmer 1995) and the LETKF (Hunt *et al.* 2007) approach. The subsections below describe these methods and outline how atmospheric ensemble initial perturbations are generated.

3.3.3.1   Local Ensemble Transform Kalman Filter

Initial perturbations based on the LETKF are generated using 50 of the 100-member ensemble of hybrid 4D-Var global analysis, each of which is a six-hour forecast valid at the initial time from previous runs of the LETKF analysis ensemble (Section 2.5). These 50 are recentered to a zero ensemble mean and inflated using the same coefficient as hybrid 4D-Var global analysis. The initial perturbations from the LETKF are then multiplied by a factor of 0.85 to avoid overestimation upon addition to initial perturbations from the SV method.

3.3.3.2 Singular Vector Method

The SV method involves extraction of atmospheric growing modes as the SVs of the linearized low-resolution model. Table 3.3.2 summarizes the specifications of SV calculation for the Global EPS. The tangent-linear and adjoint models of JMA's 4D-Var system (Section 2.5) as of March 2021 generate SVs, although the resolution, fourth-order horizontal diffusion and cumulus convection parameterization of the models are modified from those of the originals. The models involve full dynamical core and physical processes including surface turbulent fluxes, vertical turbulent transports, gravity wave drag, long-wave radiation, cloud and large-scale precipitation, and cumulus convection. SVs based on tangent-linear and adjoint models incorporating full physical processes are called moist SVs, while those based on models incorporating simplified physical processes involving surface fluxes and vertical diffusion are called dry SVs.

Table 3.3.2: SV calculation specifications

Resolution	Spectral triangular truncation 63 (TL63), 40 levels		
Norm	Moist total energy		
Target area	Northern hemisphere (30 – 90°N)	Southern hemisphere (90 – 30°S)	Tropics (30°S – 30°N)
Physical process	Simplified physics		Full physics
Optimization time	48 hours		24 hours
Number of perturbations	25		

1. SV Definition

   SV calculations are conducted for the Northern Hemisphere (30 – 90°N), the tropics (30°S – 30°N) and the Southern Hemisphere (90 – 30°S). Dry SVs with 48-hour optimization are computed for the Northern Hemisphere and the Southern Hemisphere, while moist SVs with a 24-hour optimization time are computed for the tropics.

2. Norm of SV Calculation

   The norm for evaluating the growth rate of dry and moist SVs is based on a total energy norm that includes a specific humidity term (Ehrendorfer *et al.* 1999):

$$
\begin{aligned}
(x, Ey) \;=\; & \frac{1}{2} \int_0^1 \int_S \left[U_x U_y + V_x V_y + \frac{c_p}{T_r} T_x T_y \right. \\
& \left. + w_q \frac{L_c^2}{c_p T_r} q_x q_y \right] dS \left(\frac{\partial p}{\partial \eta} \right) d\eta + \frac{1}{2} \int_S \left[\frac{R_d T_r}{P_r} P_x P_y \right] dS.
\end{aligned}
\tag{3.3.1}
$$

   Here, U_x, V_x, T_x, q_x and P_x are the zonal wind, meridional wind, temperature, specific humidity and surface pressure components of the state vector x, respectively. The left-hand side of Eq. (3.3.1) is an inner product of state vectors x and y with a weighting of norm operator E. c_p is the specific heat of dry air at a constant pressure, L_c is the latent heat of condensation, and R_d is the gas constant for dry air. $T_r = 300$ K is a reference temperature, $P_r = 800$ hPa is a reference pressure, and w_q is a constant (here 0.04). $\int dS$ is the horizontal integration for the whole globe, and $\int \left(\frac{\partial p}{\partial \eta} \right) d\eta$ gives the vertical integration from the surface to the model top. Horizontal integration is performed over each target area instead of the whole globe at the end of the optimization time. The norm at the initial time is also vertically integrated with a weight dependent on the model level; all terms are neglected above the 31st model level, and the specific humidity term is neglected above the 9th model level. When the surface pressure is 1,000 hPa, the 31st and 9th model levels correspond to around 50 and 750 hPa, respectively. This suppresses initial perturbation with a large peak of energy in the upper stratosphere and confines initial specific humidity perturbation in the lower troposphere.

3. Generation of SV-based Perturbations

SV-based perturbations are linear combinations of SVs. A total of 50 SVs are generated for the Northern Hemisphere and Southern Hemisphere, and 35 for the tropics. SVs with extremely high growth rates and those with large humidity perturbations over desert areas in low latitudes are discarded, as their modes do not grow appropriately in the Global EPS. The SVs are transformed in a variance minimum rotation (Yamaguchi *et al.* 2009) to generate 25 SV-based perturbations for each targeted area. The perturbations for both hemispheres are scaled so that related amplitudes of temperature at the 15th model level (or the 6th model level for the tropics) in the targeted area are 0.21 K (or 0.20 K for the tropics). When the surface pressure is 1,000 hPa, the 15th and 6th model levels correspond to around 500 and 850 hPa, respectively. The perturbations for the three targeted areas are linearly combined to create global perturbations.

Initial conditions for 50 perturbed members are generated by adding or subtracting the 25 SV-based perturbations from the analysis.

3.3.4 Perturbed Physics

The stochastic physics scheme (Buizza *et al.* 1999b) is used for perturbed members to represent model uncertainties in physical parameterizations. This scheme represents random errors associated with physical processes as follows:

$$\frac{\partial \mathbf{x}}{\partial t} = F(\mathbf{x}) + \alpha(\lambda, \phi, t) P(\mathbf{x}). \tag{3.3.2}$$

Here, t, $\mathbf{x}$, $F(\mathbf{x})$ and $P(\mathbf{x})$ represent time, the set of forecast variables, the overall tendency of the forecast model and the tendency of parameterized physical processes at latitude λ and longitude ϕ, respectively. The random variable $\alpha(\lambda, \phi, t)$ is expressed via a triangularly truncated spherical harmonics expansion (Berner *et al.* 2009) with a truncation wave number of 20. It has a time correlation of six hours based on a first-order autoregressive process. The average of α is set as zero. Its value is limited to a specific range (-0.7 to 0.7) to avoid excessive perturbation, and its value in the stratosphere is also set as zero.

3.3.5 Sea Surface Temperature and Related Perturbations

The SST boundary condition of the Global EPS combines anomaly-fixed SSTs (Subsection 3.2.12) from JMA analysis (Subsection 5.2.1) and SST prediction from the Seasonal EPS (Section 3.4) using a two-tiered approach (Takakura and Komori 2020) in which an anomaly-fixed value covers the entire globe for up to 6 days and is linearly relaxed to the bias-corrected ensemble mean of the Seasonal EPS from 6 to 11 days.

SST perturbations (Hotta and Ota 2019) are then generated and added to the SST of perturbed members. The perturbation of the anomaly-fixed SST for the member i (ΔSST_i^f) in the forecast from the initial time T_0 is constructed as

$$\Delta SST_i^f \left(T_0; t_f \right) = \alpha \left[SSTA \left(T_i + \Delta T + t_f \right) - SSTA \left(T_i \right) \right] \tag{3.3.3}$$

where *SSTA* is the SST anomaly from the daily climatology, t_f is the forecast lead time and T_i is a past date randomly sampled from the range within ± 29 days from the calendar date of the initial time. ΔT and α are tunable parameters, and are set as 1 day and 1.0, respectively. Perturbation of SST prediction from the Seasonal EPS is the same as that of the anomaly-fixed SST, except α is set as 0.85 because the RMSE of SST prediction from the Seasonal EPS is smaller than that of the anomaly-fixed SST in the tropics and subtropics. SST perturbation is set as 0 where the maximum sea ice concentration on T_0, T_i and $T_i + \Delta T + t_f$ is above a certain threshold (0.001) to prevent the use of excessively large perturbations.

3.3.6 Performance

The performances of each EPS product are described below. For the sake of completeness, the period before Global EPS operation is also incorporated.

3.3.6.1 Typhoon Forecasting

Typhoon forecasting is supported by the Global EPS, as it was previously by the Typhoon EPS. The results of related verification are provided in the Annual Report on Activities of the RSMC Tokyo – Typhoon Center [7].

Ensemble TC tracks derived from the EPS enable JMA forecasters to integrate TC track forecast uncertainty into their operational processes. Strike probability data, which indicate the chances of a TC center passing within 120 km of a grid point, are routinely produced as a form of probabilistic guidance. Figure 3.3.1 shows the reliability of this probability data for the coming five days [8].
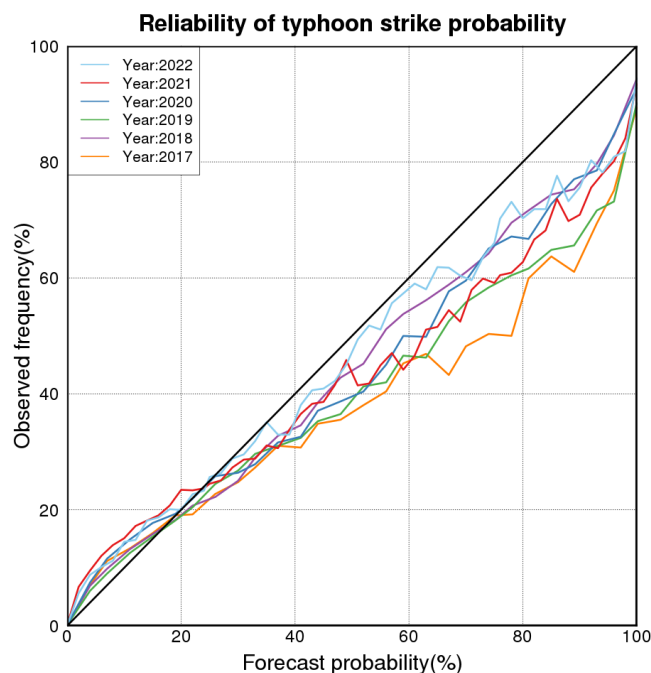

Figure 3.3.1: Reliability diagram for probabilistic typhoon-position forecasts as derived from the EPS for 2017 (yellow), 2018 (purple), 2019 (green), 2020 (blue), 2021 (red) and 2022 (light blue). RSMC Tropical Cyclone Best Track information was referenced as observation data.

3.3.6.2 One-week Forecasting

One-week forecasting is now supported by the Global EPS rather than the previous One-week EPS. The results of related verification are provided on the website of the WMO Lead Centre for EPS Verification[9].

Figure 3.3.2 shows a time-series representation of monthly-averaged RMSEs for the 500-hPa geopotential height ensemble mean forecast against analysis for the Northern Hemisphere (NH; 20 – 90°N). Figure 3.3.3 compares RMSEs of ensemble means, unperturbed members and the spread of the ensemble averaged for the periods of DJF (December/January/February) 2021/2022 and JJA (June/July/August) 2022. A higher level of skill is observed for ensemble means than for unperturbed members, especially for longer lead times. For shorter forecast lead times, the spread is almost the same size as that for the ensemble mean RMSE; however, as the forecast lead time increases, values tend to fall slightly. Figure 3.3.4 shows the Brier skill score (BSS) for 500-hPa geopotential height probabilistic forecasts in the NH. The reference forecast for the skill score is the climatological probability given by the frequency derived from analysis fields for each month. Since the start of operation, performance has improved annually in ensemble mean forecasts and probabilistic forecasts.

---

[7]https://www.jma.go.jp/jma/jma-eng/jma-center/rsmc-hp-pub-eg/annualreport.html

[8]The 2021 result was calculated using forecast data only for the period from April to December to maintain verification data consistency,
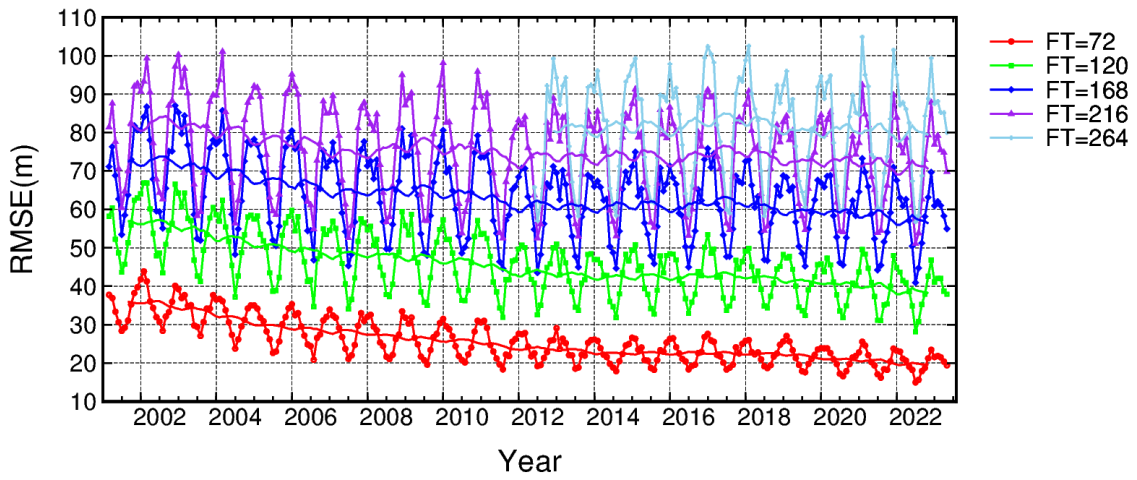
Figure 3.3.2: Time-series representation of ensemble mean scores for the EPS (where the score is the monthly average RMSE of the ensemble mean) for Northern Hemisphere (20 – 90°N) 500-hPa geopotential height forecasts with lead times of 72 (red), 120 (green), 168 (dark blue), 216 (violet) and 264 (light blue) hours from March 2001 to May 2023. 13-month running means are also shown.
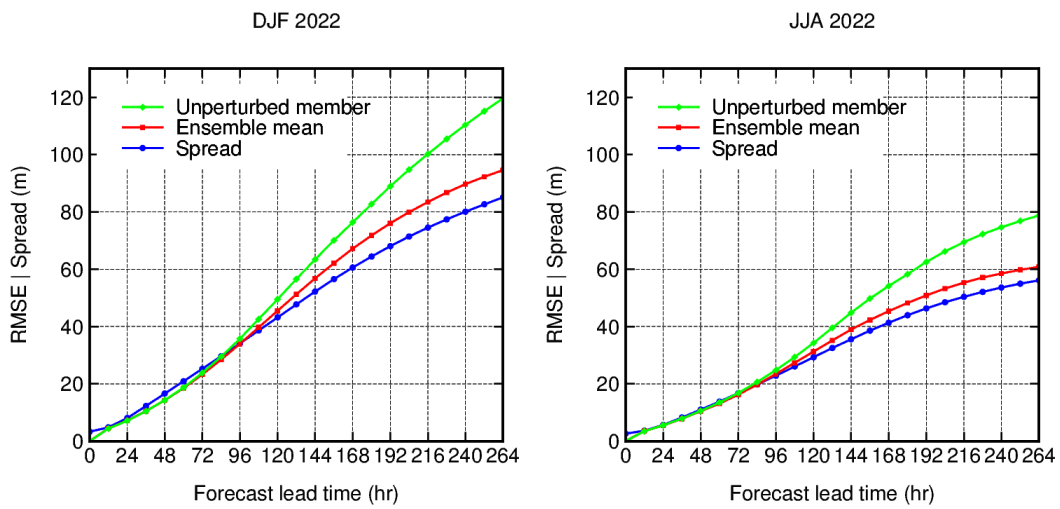

Figure 3.3.3: RMSEs for Northern Hemisphere (20 – 90°N) 500-hPa geopotential height forecasts for the ensemble mean (red) and the unperturbed member (green) for DJF 2021/2022 and JJA 2022 from the EPS. The spread of the ensemble (blue) is also shown.
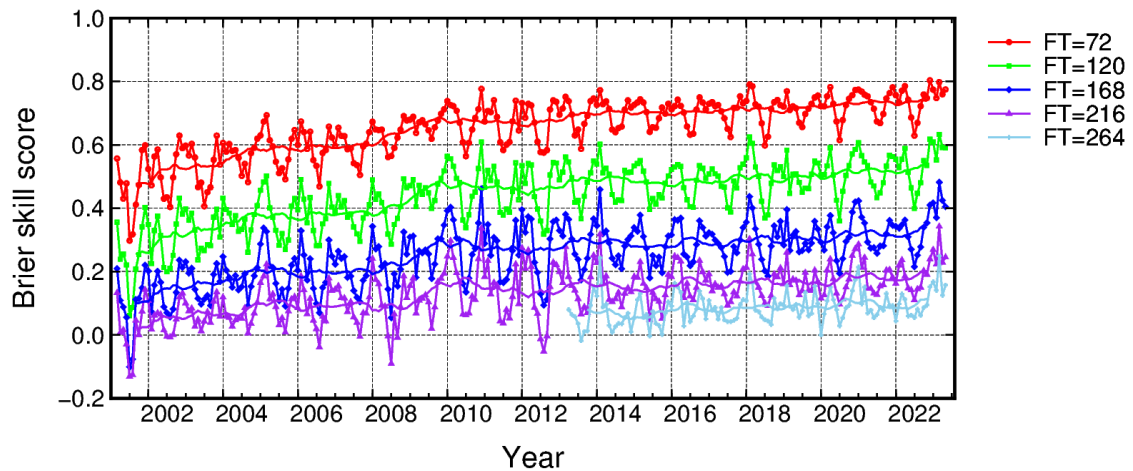
94

Figure 3.3.4: As per Figure 3.3.2, but for Brier skill score with probabilistic forecasts of 500-hPa geopotential height negative anomalies with magnitudes less than one climatological standard deviation from JMA's EPS.

3.3.6.3 One-month Forecasting

One-month forecasting is now supported by the Global EPS rather than the previous One-month EPS. The results of prediction skill evaluation based on hindcast experiments and real-time forecasts are provided on the Tokyo Climate Center website[10]. Hindcast experiments covering the period from 1991 to 2020 with 13 ensemble members were conducted using atmospheric initial conditions produced from JRA-3Q (Section 2.11). Initial perturbations were created from a combination of initial and evolved SVs. For computational efficiency, perturbations from LETKF application in real-time operation were not adopted.

The skill of ensemble mean forecasts was evaluated using the Anomaly Correlation Coefficient (ACC) and the RMSE for selected areas with respect to several physical variables. Probabilistic forecast skill was also evaluated based on BSS, Reliability Skill Score, Resolution Skill Score and Relative Operating Characteristics (ROCs).

Figure 3.3.5 shows a time-series representation of NH 500-hPa geopotential height ACC for ensemble mean forecasts averaged for days 2 – 29 (the running mean of 52 forecasts) based on operational forecasting conducted from 1997 to 2022. Skill exhibits a rising trend with fluctuations corresponding to El Niño Southern Oscillation (ENSO). Table 3.3.3 shows ROC areas of 2-m temperature (T2m) and 500-hPa geopotential height (Z500) anomalies based on hindcast experiments verified against JRA-3Q analysis, and indicates that skill for the tropics is higher than for the extratropics in all forecasts from each initial season.

---

as the ensemble size of the Global EPS was increased in March 2021.

[9] http://epsv.kishou.go.jp/EPSv/

[10] https://www.data.jma.go.jp/tcc/tcc/index.html

Table 3.3.3: ROC areas of 28-day (from day 3 to day 30) mean 2-m temperature (T2m) and 500-hPa geopotential height (Z500) anomaly prediction for positive anomaly events in the Northern Hemisphere (NH; 20 – 90°N), the tropics (20°S – 20°N), and the Southern Hemisphere (SH; 90 – 20°S) based on hindcast experiments covering the period from 1991 to 2020. The figures in the table are multiplied by 100.

T2m

Init	NH	Tropics	SH
DJF	81.9	86.2	80.6
MAM	79.3	84.3	78.7
JJA	79.6	83.5	78.1
SON	79.5	84.2	79.3

Z500

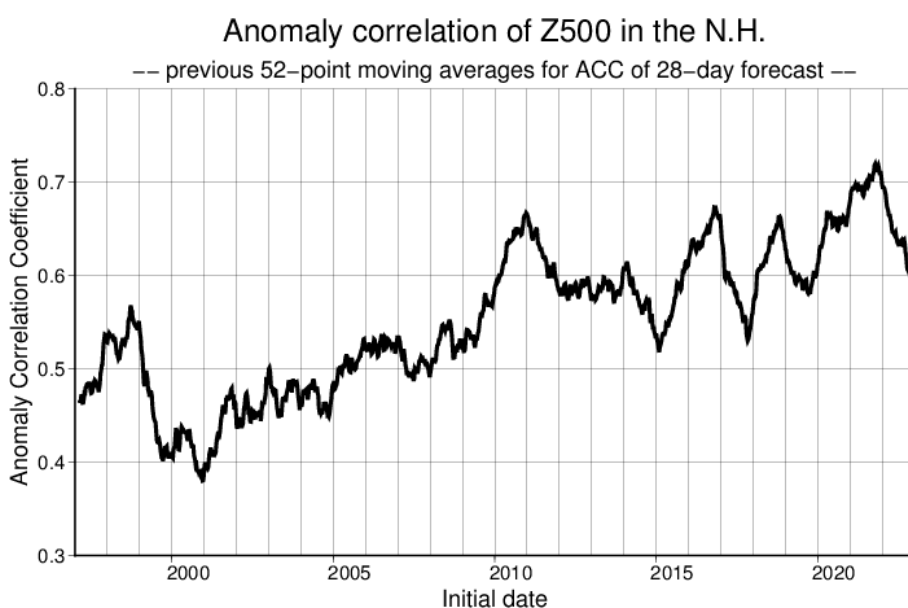| Init	NH	Tropics	SH
DJF	80.3	92.2	76.5
MAM	76.2	91.3	74.7
JJA	75.9	88.1	75.6
SON	74.9	89.0	77.8

Figure 3.3.5: Time-series representation for the Northern Hemisphere (NH; 20 – 90°N) 500-hPa geopotential height anomaly correlation coefficient in ensemble mean forecasts averaged over 28 days from day 2 to day 29 (the running mean of 52 forecasts) based on operational forecasting conducted from 1997 to 2022.

3.4 Seasonal Ensemble Prediction System

3.4.1 Introduction

JMA operates the Seasonal EPS to support a wide range of seasonal forecast products, including three-month forecasts, warm- and cold-season forecasts, and El Niño outlooks. JMA began operating an ensemble prediction system with an atmosphere-ocean coupled model in July 1998 with and objective limited to El Niño outlooks. Since February 2010, seasonal forecasts have also been covered by upgraded systems (Takaya *et al.* 2017). The latest major update was introduced in February 2022. This section describes the details of the latest JMA/MRI-CPS3 (referred to simply as CPS3) (Hirahara *et al.* 2023).

3.4.2 System Configuration

3.4.2.1 Forecast Model

The CPS3 forecast model is an atmosphere/land/ocean/sea-ice coupled type (Table 3.4.1).

The atmosphere/land model is based on a low-resolution version of JMA's Global Spectral Model as of March 2020 (GSM2003; Yonehara *et al.* 2020; JMA 2019), with a horizontal resolution of TL319 (triangular truncation at total wavenumber 319 with a linear grid), which corresponds to approximately 55-km grid spacing, and 100 vertical levels with the model top at 0.01 hPa. In CPS3, several schemes were upgraded from GSM2003 to improve representation of atmosphere/ocean climatology and sub-seasonal to inter-annual variability. Refinements for the cumulus convection scheme included treating the dissipation time scale of kinetic energy separately for shallow and deep cumulus clouds. The cumulus entrainment rate is modified to take into account empirical dependence on altitude and humidity, rather than being constant in the vertical direction (Bechtold *et al.* 2008; Komori *et al.* 2020), and the lower limit of it is proportional to the depth of the planetary boundary layer (Tokioka *et al.* 1988). The stratocumulus scheme is triggered when the conditions proposed by Kawai *et al.* (2017) are met (Chiba and Kawai 2021). Gustiness near the sea surface is parameterized with downdrafts generated by deep convection (Redelsperger *et al.* 2000) and boundary layer free convection (Godfrey and Beljaars 1991). The skin sea surface temperature (SST) scheme, which solves the heat budget in the upper few meters of the ocean in consideration of diurnal changes in the vertical water temperature profile and the surface skin layer in radiative equilibrium, is introduced by expanding Zeng and Beljaars (2005). A fractional land ratio is introduced to consider sub-grid-scale water surfaces. The thermodynamic lake scheme is also adopted to predict lake ice formation and lake temperature variations through water phase changes and heat transfer among water, ice and snow. Calculation of solar zenith angles (Hogan and Hirahara 2016) and treatment of surface albedo (Hogan and Bozzo 2015) for shortwave radiation are also adopted. A monthly climatology of ozone concentration calculated from 1981 – 2010 MRI-CCM2 reanalysis is used (Subsection 3.9.1, Deushi and Shibata 2011). Greenhouse gas concentrations are based on observations conducted up to 2016 and on the Coupled Model Intercomparison Project phase 6 (CMIP6) emission scenario SSP2-RCP4.5 (Van Vuuren *et al.* 2011) thereafter. A three-dimensional monthly aerosol concentration climatology (Yabu *et al.* 2017) is used both for re-forecasts and operational forecasts, and CPS3 provides a mode allowing evaluation of the direct radiative effect from volcanic aerosols in the event of eruptions.

The ocean/sea-ice component is the Meteorological Research Institute Community Ocean Model version 4.6 (MRI.COM; Tsujino *et al.* 2017). For CPS3, the model is configured to cover the whole globe with the tripolar grid of Murray (1996) at a horizontal resolution of 0.25 x 0.25° . This resolution is sufficient to

Table 3.4.1: JMA Seasonal EPS specifications

Last update	February 2022
Initial Time	00 UTC, every day
Forecast Range	up to seven months
Ensemble Size	5 members per start date
Forecast Model	GSM coupled with the Meteorological Research Institute Community Ocean Model (MRI.COM)
Horizontal Resolution	GSM: Spectral triangular 319 (TL319) reduced Gaussian grid system, equivalent to approximately 55km MRI.COM: 0.25 x 0.25° in latitude and longitude
Vertical Resolution (model top)	GSM: 100 stretched sigma pressure hybrid levels (0.01 hPa) MRI.COM: 60 levels
Initial perturbation method	Atmosphere: BGM method and LAF method Ocean: Perturbations calculated using 4DVAR minimization history and LAF method
Model perturbation method	Stochastic physics scheme for the atmosphere

resolve Tropical Instability Waves, which promote heat exchange between the equator and its north and south, providing negative feedback to the Pacific equatorial SST during El Niño Southern Oscillation (ENSO) periods (Vialard *et al.* 2001; An 2008). A z* vertical coordinate (Adcroft and Campin 2004) is used to accurately capture flow along steep seafloor topography. The sea ice model deals with sea ice advection, formation, growth, and melting using five ice-thickness categories (Tsujino *et al.* 2017).

The atmosphere and ocean models are integrated at different time steps, with a simple coupler (Yoshimura and Yukimoto 2008) absorbing the difference and exchangeing sea surface temperature, sea ice cover and sea surface fluxes (radiation, latent and sensible heat, momentum and fresh water) between the models every hour.

Atmospheric conditions are initialized with the Japanese Reanalysis for Three Quarters of a Century (JRA-3Q-provisional, Kosaka *et al.* 2024) for re-forecast, and the JMA Global Analysis (GA) for operational forecast, in which atmospheric conditions are updated with a shorter time delay. CPS3 has a different land-sea mask from this analysis and a unique lake scheme that requires initialization. To fill the gaps between these differences while avoiding initial shock, offline surface simulation is separately run with JRA-3Q forcing and GA (for operational forecasts only). Oceanic and sea ice initial conditions are from the ocean data assimilation system (MOVE-G3; Fujii *et al.* 2023, Section 5.3).

3.4.2.2   Ensemble Size, Forecast Range and Frequency

To represent uncertainties in the initial condition, CPS3 adopts a combination of the Lagged Average Forecast (LAF; Hoffman and Kalnay 1983) method and the initial perturbation method described below. CPS3 runs a control member and four perturbed members from an initial time of 00 UTC every day up to seven months. Operational products for seasonal forecasting and El Niño outlooks at JMA are composed of 51 members (involving 3 members and 17 start dates). Atmospheric initial perturbations are generated via the Breeding of Growing Modes (BGM) method (Chikamoto *et al.* 2007). Oceanic initial perturbations are generated using 4DVAR minimization history, with which daily analysis error covariance can be approximated (Niwa and Fujii 2020). To represent physical processes in the model, a stochastic physics scheme (Yonehara and Ujiie 2011; Buizza *et al.* 1999b) is applied to perturbed ensemble members (Subsection 3.3.4).

3.4.2.3   BGM Method

Atmospheric perturbation breeding is performed separately for the Northern Hemisphere (NH; 20 – 90°N), the tropics (20°S – 20°N) and the Southern Hemisphere (SH; 20 – 90°S). First, perturbed and unperturbed initial conditions are integrated up to 24 hours. Then, the difference between perturbed and unperturbed fields is normalized so that the area-averaged root mean square difference for 500-hPa geopotential height over the NH and SH (200-hPa velocity potential for the tropics) is equal to 14.5 (20.0) % of the climatological variance. The normalized perturbations are subsequently orthogonalized to each other and added to the analysis to create the next set of initial perturbations. In CPS3, the NH, SH and tropical initial perturbations are combined and added to/subtracted from JRA-3Q (re-forecast) and GA (operational forecast).

3.4.3   Performance

The forecast skill of CPS3 is evaluated in line with the World Meteorological Organization (WMO) Global Data Processing and Forecasting System manual (WMO 2019). To verify performance, a 30 year hindcast for 1991 – 2020 was performed with forecast model identical to the operational application, except for an ensemble size of 10 rather than 51.

Figure 3.4.1 shows the Anomaly Correlation Coefficients (ACCs) for use between ensemble mean forecasts and Merged satellite and in-situ data Global Daily SSTs (MGDSSTs, Kurihara *et al.* 2006) in NINO.3 (5°S – 5°N, 150 – 90°W), NINO.WEST (0° – 15°N, 130 – 150°E) and IOBW (20°S – 20°N, 40 – 100°E). CPS3 effectively reproduces inter-annual modes of variability in tropical oceans, which are the primary known basis for seasonal predictability. The Relative Operating Characteristic (ROC) areas of 2-m temperature (T2m) anomalies and 500-hPa geopotential height (Z500) anomalies are shown in Table 3.4.2. Skill for the tropics is superior to that for the NH and SH.
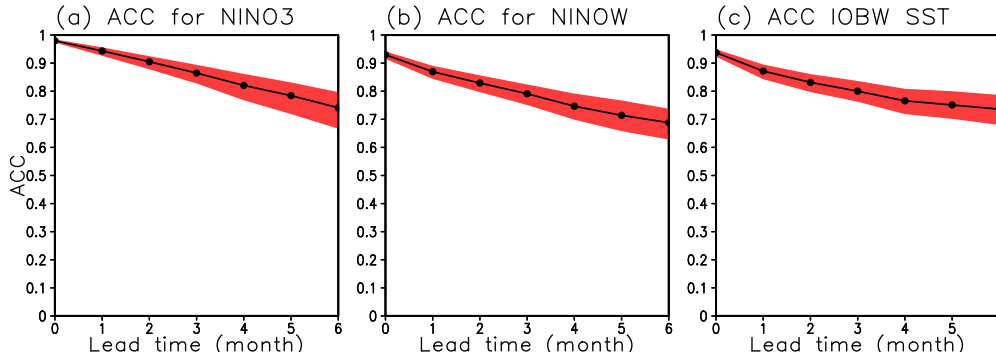
Figure 3.4.1: ACC for MGDSSTs in (a) NINO.3 (5°S – 5°N, 150 – 90°W), (b) NINO.WEST (0° – 15°N, 130 – 150°E) and (c) IOBW (20°S – 20°N, 40 – 100°E). Shading indicates a 95% confidence interval estimated using the bootstrap method (1,000 samples).

Table 3.4.2: ROC areas of three-month mean (JJA and DJF) T2m and Z500 for positive anomaly events (upper tercile) in the NH, the tropics and the SH. Statistics are based on hindcast experiments for 1991 – 2020. The numbers in the table are multiplied by 100. The initial months are May (10-member LAFs from April 11 and 26) for JJA and November (10-member LAFs from October 13 and 28) for DJF.

T2m	NH	Tropics	SH
JJA(Initial:May)	66.8	77.2	66.3
DJF(Initial:Nov)	67.3	80.9	67.4

Z500	NH	Tropics	SH
JJA(Initial:May)	68.1	90.2	64.9
DJF(Initial:Nov)	66.8	90.0	67.8

Other verification scores can be found on the Tokyo Climate Center website (https://www.data.jma.go.jp/tcc/tcc/products/model/hindcast/CPS3/index.html).

3.5 Meso-Scale Model (JMA-MSM2206)

3.5.1 Introduction

The meso-scale numerical prediction system has been operated since March 2001 to provide information for disaster prevention and aviation safety. The Meso-Scale Model (MSM) was initially a hydrostatic spectral model, producing 18-hour forecasts every 6 hours at 00, 06, 12 and 18 UTC. The domain covered Japan and its surrounding areas (3,600 km × 2,880 km) at a horizontal resolution of 10 km with 40 vertical layers.

In September 2004, the MSM was replaced with a non-hydrostatic grid model (JMA-NHM; Saito *et al.* 2006, 2007) with retention of similar general configurations in areas such as resolution, forecast time and forecast frequency. In March 2006, resolution and operation frequency were enhanced to produce 15-hour forecasts at 00, 03, 06, 09, 12, 15, 18 and 21 UTC with 5-km horizontal-grid spacing and 48 vertical layers. After subsequent model updates, the forecast period of the MSM was extended to 39 hours for all eight daily operations with an enlarged domain (4,080 km × 3,300 km) in 2013. The forecast period was extended to 51 hours at 00 and 12 UTC in March 2019, and subsequently to 78 hours at 00 and 12 UTC in June 2022. The extension of the forecast period and the model domain supported improved provision of useful information for disaster prevention and aviation operations with a two-day lead time.

In February 2017, the new-generation nonhydrostatic model ASUCA (Ishida *et al.* 2009, 2010, 2022) was incorporated into the operational MSM following its application for LFM usage in January 2015 (Aranami *et al.* 2015). The development of ASUCA was begun in 2007 after the development and widespread adoption of new nonhydrostatic equations allowing conservation of mass as well as sophisticated numerical methods

in computational fluid dynamics. Efficient operation of numerical models on scalar multi-core architecture was also required against a background of rapid expansion in the market for massive scalar computers in the supercomputer field (Hara *et al.* 2012).

ASUCA has great potential to meet these demands. In the model, flux-form fully compressible governing equations are adopted and discretized using the finite volume method to guarantee mass conservation. The three-stage Runge-Kutta scheme (Wicker and Skamarock 2002) is employed for time integration, leading to better computational stability, even with a longer time-step interval, than the JMA-NHM. Improvement of parallelization and coding methods yields more effective computation on massive scalar multi-core architecture.

Physical processes equivalent to or better than those of the JMA-NHM are implemented via the use of the Physics Library [11] , in which various subroutines related to physical processes are collected as vertical one-dimensional models with unified coding and interface rules (Hara *et al.* 2012; Hara 2015). This simple one-dimensional realization helps to improve computational efficiency, especially on scalar computers, and facilitates efficient development of physical processes such as evaluation of the straightforward responses of specific processes of interest via idealized single-column model experiments.

As described above, the MSM was significantly upgraded with the introduction of ASUCA in February 2017, updating of cloud microphysics, cloud fractions and land process in March 2020, and a layer-number was increase from 76 to 96 in March 2022. A one-dimensional ocean mixed-layer model predicting sea surface temperature (SST) was also introduced to represent SST cooling related to wind stress over ocean. Here Subsection 3.5.2 describes general configurations, Subsection 3.5.3 outlines the design of the dynamical core, and other subsections detail physical processes such as cloud physics, convective parameterization and radiation. Improvement of parallelization in ASUCA is described in Subsection 3.5.11, and forecast performance evaluation is detailed in Subsection 3.5.12.

3.5.2   General Configuration

The current ASUCA-based MSM is operated eight times a day, providing 78-hour forecasts at 00 and 12 UTC and 39-hour forecasts at 03, 06, 09, 15, 18 and 21 UTC. Its forecast domain is a rectangular flat area of 4,080 km × 3,300 km covering Japan and its surroundings, with a grid spacing of 5 km. The domain configuration is identical to that of 4D-Var Meso-scale Analysis (MA; see Section 2.6) as depicted in Figure 2.6.2. The rectangular plane is determined via a Lambert conformal conic map projection of the Earth's sphere with a map scale factor applied to correct plane expansion or shrinkage associated with projection from the sphere. Hybrid terrain following the relevant coordinates is adopted for the vertical coordinate to reduce the influences of topography as height increases (Subsection 3.5.3). The lowest atmospheric layer is 10 m above the surface, and the model top is at 37,500 m with 96 layers at intervals increasing from 20 m at the bottom to approximately 915 m at the top.

The prognostic variables are horizontal and vertical momentum, mass-virtual potential temperature, total mass density, density of water vapor and hydrometeors (cloud water, cloud ice, rain, snow and graupel), ground temperature, soil water and four of the second-order moments of turbulent fluctuations (including turbulent kinetic energy). The model is operated with a 100/3-second time step.

Initial conditions for the model are generated via MA. Lateral boundary conditions come from the latest available GSM (Section 3.2) forecast with a 3- or 6-hour time lag. Thus, for example, the MSM at 03 and 06 UTC has lateral boundaries from the GSM initiated at 00 UTC.

The model terrain setting relies on the GTOPO30 data set, which is a global digital elevation model with a horizontal grid spacing of 30 arc seconds developed by the U.S. Geological Survey's EROS Data Center (EDC). To avoid computational instability related to steep slopes on terrain, smoothing is performed so that the valid resolution of the terrain adopted in the model is 1.5 times as coarse as that of the model itself.

The Global Land Cover Characteristics (GLCC) data set, also provided by EDC, is used to determine the land-sea attributes of all grids in the model. To alleviate discontinuities in surface wind and temperature fields around coastlines, a tiling approach is introduced in which land/sea sub-grid effects can be considered in surface flux evaluation. Surface-related parameters such as heat capacity, thermal conductivity and roughness are also

---

[11] The term ASUCA in this section refers to an NWP model incorporating physical processes from the Physics Library. The term sometimes refers only to the related dynamical core in a more narrow sense.

based on land use as described by the GLCC data set. The National Land Numerical Information data set provided by Japan's Ministry of Land, Infrastructure, Transport and Tourism is also referenced for parameters over Japan. Albedo and initial values of soil moisture are prescribed from monthly mean climatology.

Grids on land are further classified in terms of snow presence, and sea grids may be covered with ice. This gives a total of four surface categories: land, snow-covered land, sea and ice-covered sea. Snow-covered areas are analyzed using the high-resolution snow depth analysis system (Subsection 2.8.2), and ice-covered areas are identified from sea ice analysis conducted by the Office of Marine Prediction under JMA's Atmosphere and Ocean Department. As described previously, surface-related parameters are essentially based on land use without assumption of snow- or ice-covered areas. Accordingly, the parameters for these covered grid areas need to be modified with corresponding values.

3.5.3 Dynamics

3.5.3.1 Basic Equations

The governing equations used in the MSM consist of non-hydrostatic, fully compressible equations on spherical curvilinear orthogonal and hybrid terrain-following coordinates with the shallow assumption. The equations are described in flux form.

1. Momentum equations

   The equations of motion are described as

$$
\frac{\partial}{\partial t}\left(\frac{1}{J}\rho u\right) + \frac{\partial}{\partial \xi}\left(\frac{1}{J}\rho u U\right) + \frac{\partial}{\partial \eta}\left(\frac{1}{J}\rho u V\right) + \frac{\partial}{\partial \zeta}\left(\frac{1}{J}\rho u W\right)
$$
$$
+ \gamma R_d \pi \left\{ \frac{1}{J}\xi_x \frac{\partial}{\partial \xi}(\rho\theta_m)' + \frac{1}{J}\eta_x \frac{\partial}{\partial \eta}(\rho\theta_m)' + \frac{1}{J}\zeta_x \frac{\partial}{\partial \zeta}(\rho\theta_m)' \right\} \tag{3.5.1}
$$
$$
= -\sum_\alpha \frac{\partial}{\partial \zeta}\left(\frac{1}{J}\rho u q_\alpha W_{t_\alpha}\right) - \frac{1}{J}\rho v \Gamma - \frac{1}{J}\rho v f + \frac{1}{J}F_{\rho u},
$$

$$
\frac{\partial}{\partial t}\left(\frac{1}{J}\rho v\right) + \frac{\partial}{\partial \xi}\left(\frac{1}{J}\rho v U\right) + \frac{\partial}{\partial \eta}\left(\frac{1}{J}\rho v V\right) + \frac{\partial}{\partial \zeta}\left(\frac{1}{J}\rho v W\right)
$$
$$
+ \gamma R_d \pi \left\{ \frac{1}{J}\xi_y \frac{\partial}{\partial \xi}(\rho\theta_m)' + \frac{1}{J}\eta_y \frac{\partial}{\partial \eta}(\rho\theta_m)' + \frac{1}{J}\zeta_y \frac{\partial}{\partial \zeta}(\rho\theta_m)' \right\} \tag{3.5.2}
$$
$$
= -\sum_\alpha \frac{\partial}{\partial \zeta}\left(\frac{1}{J}\rho v q_\alpha W_{t_\alpha}\right) + \frac{1}{J}\rho u \Gamma + \frac{1}{J}\rho u f + \frac{1}{J}F_{\rho v},
$$

$$
\frac{\partial}{\partial t}\left(\frac{1}{J}\rho w\right) + \frac{\partial}{\partial \xi}\left(\frac{1}{J}\rho w U\right) + \frac{\partial}{\partial \eta}\left(\frac{1}{J}\rho w V\right) + \frac{\partial}{\partial \zeta}\left(\frac{1}{J}\rho w W\right)
$$
$$
+ \gamma R_d \pi \left\{ \frac{1}{J}\zeta_z \frac{\partial}{\partial \zeta}(\rho\theta_m)' \right\} + \left(\frac{\rho'}{J} - \frac{\pi'}{\pi}\frac{\overline{\rho}}{J}\right)\mathfrak{g} \tag{3.5.3}
$$
$$
= -\sum_\alpha \frac{\partial}{\partial \zeta}\left(\frac{1}{J}\rho w q_\alpha W_{t_\alpha}\right) + \frac{1}{J}F_{\rho w},
$$

where

$$
\Gamma = u\frac{m_2}{m_1}\frac{\partial m_1}{\partial \eta} - v\frac{m_1}{m_2}\frac{\partial m_2}{\partial \xi}. \tag{3.5.4}
$$

Here, J is the Jacobian of coordinate transformation from Cartesian coordinates (x, y, z) to generalized coordinates (ξ, η, ζ), defined as

$$J \equiv \begin{vmatrix} \xi_x & \xi_y & \xi_z \\ \eta_x & \eta_y & \eta_z \\ \zeta_x & \zeta_y & \zeta_z \end{vmatrix},$$

(3.5.5)

where, $(\partial\xi/\partial x)_{y,z}$ - a metric of coordinate transformation - is described as ξ_x, and the same description applies to other metrics. A limitation for vertical coordinate to satisfy $\xi_z = \zeta_z = 0$ is introduced, enabling utilization of the Split-Explicit time integration scheme (see Subsection 3.5.3.3). (u, v, w) and (U, V, W) represent velocity components in Cartesian coordinates and generalized coordinates, respectively. $\gamma = C_p/C_v$, where C_p and C_v are the specific heat of dry air at constant pressure and constant volume, respectively. R_d is the gas constant for dry air, and ρ is the total mass density defined as

$$\rho = \rho_d + \rho_v + \rho_c + \rho_r + \rho_i + \rho_s + \rho_g,$$

(3.5.6)

where the subscripts d, v, c, r, i, s and g represent dry air, water vapor, cloud water, rain, cloud ice, snow and graupel, respectively.

π is the Exner function defined by

$$\pi = \left(\frac{p}{p_0}\right)^{\frac{R_d}{C_p}}.$$

(3.5.7)

The overlined variables $\overline{\rho}$, $\overline{\rho\theta_m}$ and $\overline{\pi}$ represent the hydrostatic state as

$$\gamma R_d \overline{\pi} \frac{1}{J} \zeta_z \frac{\partial}{\partial\zeta}\left(\overline{\rho\theta_m}\right) + \frac{\overline{\rho}g}{J} = 0,$$

(3.5.8)

and the variables with prime ρ', $(\rho\theta_m)'$ and π' represent perturbation from the hydrostatic state. g is gravity acceleration, and f is the Coriolis parameter. q_α is the ratio of the density of water substances α to the total mass density $(\alpha = v, c, r, i, s, g)$. $W_{t\alpha}$ is the terminal fall velocity of water substance α. θ_m is defined as

$$\theta_m \equiv \theta\left(1 + \left(\frac{1-\epsilon}{\epsilon}\right)q_v - q_c - q_r - q_i - q_s - q_g\right),$$

(3.5.9)

where ϵ is the ratio of R_d to the gas constant for water vapor. $F_{\rho u}$, $F_{\rho v}$ and $F_{\rho w}$ are terms of the surface friction.

Lambert conformal projection is employed, and the map factors m_1 and m_2 (for the x and y directions) are given by

$$m_1 = m_2 = m = \left(\frac{\cos\varphi}{\cos\varphi_1}\right)^{a-1}\left(\frac{1+\sin\varphi_1}{1+\sin\varphi}\right)^a,$$

(3.5.10)

where φ is the latitude of the relevant point, $\varphi_1 = 30°$, $\varphi_2 = 60°$ and a is given by

$$a = \ln\left(\frac{\cos\varphi_1}{\cos\varphi_2}\right)\bigg/ \ln\left\{\frac{\tan\left(45° - \dfrac{\varphi_1}{2}\right)}{\tan\left(45° - \dfrac{\varphi_2}{2}\right)}\right\}.$$

(3.5.11)

The hybrid terrain-following vertical coordinate which is based on the same approach as the η coordinate (Simmons and Burridge 1981) is adopted to reduce the influences of topography as height increases (Ishida 2007). The vertical coordinate ζ is transformed using the equation:

$$z = \zeta + z_s h(\zeta),$$

(3.5.12)

where z is the height and z_s is the surface height. The function $h(\zeta)$ is given by,

$$h(\zeta) = \frac{b\left\{1 - \left(\frac{\zeta}{z_T}\right)^n\right\}}{b + \left(\frac{\zeta}{z_T}\right)^n}, \quad b = \frac{\left(\frac{z_l + z_h}{2z_T}\right)^n}{1 - 2\left(\frac{z_l + z_h}{2z_T}\right)^n},$$

(3.5.13)

where z_T is the model top, $z_l = 2000$m, $z_h = 12000$m and $n = 3$, respectively.

2. Continuity equations

The continuity equation is described as follows:

$$\frac{\partial}{\partial t}\left(\frac{1}{J}\rho'\right) + \frac{\partial}{\partial \xi}\left(\frac{1}{J}\rho U\right) + \frac{\partial}{\partial \eta}\left(\frac{1}{J}\rho V\right) + \frac{\partial}{\partial \zeta}\left(\frac{1}{J}\rho W\right) = -\sum_\alpha \frac{\partial}{\partial \zeta}\left(\frac{1}{J}\rho q_\alpha W_{t_\alpha}\right) + \frac{1}{J}F_\rho,$$

(3.5.14)

where F_ρ is the tendency by water vapor flux from the surface.

3. Prognostic equation of potential temperature

The thermodynamic equation is described as

$$\frac{\partial}{\partial t}\left(\frac{1}{J}(\rho\theta_m)'\right) + \frac{\partial}{\partial \xi}\left(\frac{1}{J}\rho\theta_m U\right) + \frac{\partial}{\partial \eta}\left(\frac{1}{J}\rho\theta_m V\right) + \frac{\partial}{\partial \zeta}\left(\frac{1}{J}\rho\theta_m W\right) = \frac{1}{J}\left(\rho_d + \frac{\rho_v}{\epsilon}\right)Q_\theta,$$

(3.5.15)

where Q_θ is the diabatic heating.

4. Prognostic equation of water substances

The prognostic equations for the density of water substances are described as

$$\frac{\partial}{\partial t}\left(\frac{1}{J}\rho q_\alpha\right) + \frac{\partial}{\partial \xi}\left(\frac{1}{J}\rho q_\alpha U\right) + \frac{\partial}{\partial \eta}\left(\frac{1}{J}\rho q_\alpha V\right) + \frac{\partial}{\partial \zeta}\left(\frac{1}{J}\rho q_\alpha(W + W_{t_\alpha})\right) = \frac{1}{J}F_{\rho\alpha},$$

(3.5.16)

where $F_{\rho\alpha}$ is source or sink term and tendency by flux from the surface for $\alpha = v$.

5. State equation

The state equation is

$$p = R_d \pi \rho \theta_m.$$

(3.5.17)

103

3.5.3.2 Spatial discretization

The grid structures of the model are the Arakawa C type in the horizontal direction and the Lorenz type in the vertical direction. The equations are spatially discretized using the finite volume method (FVM) to conserve total mass throughout the whole domain in consideration of lateral boundary inflow and outflow. The third-order upwind scheme with the flux limiter function proposed by Koren (1993) is employed to calculate horizontal and vertical advection terms for monotonicity in order to prevent numerical oscillation, and enhance computational efficiency.

3.5.3.3 Time integration

The Runge-Kutta (RK3) scheme (Wicker and Skamarock 2002) is adopted for system time integration. The terms responsible for sound waves and gravity waves are treated using a split-explicit time integration scheme with a short time step. Other time-splitting methods are also used to treat vertical advection associated with strong wind and vertical advection of water substances with high terminal velocity such as rain or graupel.

1. Split-Explicit (HE-VI) Scheme

   The horizontally explicit and vertically implicit (HE-VI) scheme (Klemp *et al.* 2007) is employed. RK3 scheme is also used for the short time step of HE-VI. Forward time integrations with the short time step $\Delta\tau$ are used for the horizontal momentum equations:

$$\left(\frac{1}{J}\rho u\right)^{\tau+\Delta\tau} = \left(\frac{1}{J}\rho u\right)^{\tau} - \gamma R_d \pi^t \left\{ \frac{1}{J}\xi_x \frac{\partial}{\partial\xi}(\rho\theta_m)'^{\tau} + \frac{1}{J}\eta_x \frac{\partial}{\partial\eta}(\rho\theta_m)'^{\tau} + \frac{1}{J}\zeta_x \frac{\partial}{\partial\zeta}(\rho\theta_m)'^{\tau} \right\}\Delta\tau + R_u^t \Delta\tau, \quad (3.5.18)$$

$$\left(\frac{1}{J}\rho v\right)^{\tau+\Delta\tau} = \left(\frac{1}{J}\rho v\right)^{\tau} - \gamma R_d \pi^t \left\{ \frac{1}{J}\xi_y \frac{\partial}{\partial\xi}(\rho\theta_m)'^{\tau} + \frac{1}{J}\eta_y \frac{\partial}{\partial\eta}(\rho\theta_m)'^{\tau} + \frac{1}{J}\zeta_y \frac{\partial}{\partial\zeta}(\rho\theta_m)'^{\tau} \right\}\Delta\tau + R_v^t \Delta\tau, \quad (3.5.19)$$

   where

$$R_u = -\frac{\partial}{\partial\xi}\left(\frac{1}{J}\rho uU\right) - \frac{\partial}{\partial\eta}\left(\frac{1}{J}\rho uV\right) - \frac{\partial}{\partial\zeta}\left(\frac{1}{J}\rho uW\right) + \frac{1}{J}F_u', \quad (3.5.20)$$

$$R_v = -\frac{\partial}{\partial\xi}\left(\frac{1}{J}\rho vU\right) - \frac{\partial}{\partial\eta}\left(\frac{1}{J}\rho vV\right) - \frac{\partial}{\partial\zeta}\left(\frac{1}{J}\rho vW\right) + \frac{1}{J}F_v', \quad (3.5.21)$$

   and $\frac{1}{J}F_u'$ and $\frac{1}{J}F_v'$ are the right hand side of Eq. (3.5.1) and Eq. (3.5.2), respectively. Backward time integrations are used for equations of vertical momentum, potential temperature and density:

$$\left(\frac{1}{J}\rho w\right)^{\tau+\Delta\tau} = \left(\frac{1}{J}\rho w\right)^{\tau} - \left\{ \gamma R_d \pi^t \frac{1}{J}\zeta_z \frac{\partial}{\partial\zeta}(\rho\theta_m)'^{\tau+\Delta\tau} + \frac{\rho'^{\tau+\Delta\tau}}{J}\mathfrak{g} - \frac{\pi''^t}{\overline{\pi}}\frac{\overline{\rho}}{J}\mathfrak{g} \right\}\Delta\tau + R_w^t \Delta\tau, \quad (3.5.22)$$

$$\begin{aligned}\left(\frac{1}{J}(\rho\theta_m)'\right)^{\tau+\Delta\tau} &= \left(\frac{1}{J}(\rho\theta_m)'\right)^{\tau} - \left\{ \frac{\partial}{\partial\zeta}\left(\frac{1}{J}\zeta_z \theta_m^{\tau}(\rho w)^{\tau+\Delta\tau}\right) \right\}\Delta\tau \\ &\quad - \left\{ \frac{\partial}{\partial\xi}\left(\frac{1}{J}\theta_m^{\tau}\widetilde{(\rho U)}\right) + \frac{\partial}{\partial\eta}\left(\frac{1}{J}\theta_m^{\tau}\widetilde{(\rho V)}\right) + \frac{\partial}{\partial\zeta}\left(\frac{1}{J}\theta_m^{\tau}\widetilde{(\rho W)}\right) \right\}\Delta\tau + \frac{1}{J}F_{\rho\theta_m}^t \Delta\tau,\end{aligned} \quad (3.5.23)$$

$$\left(\frac{1}{J}\rho'\right)^{\tau+\Delta\tau} = \left(\frac{1}{J}\rho'\right)^{\tau} - \left\{\frac{\partial}{\partial\zeta}\left(\frac{1}{J}\zeta_z(\rho w)^{\tau+\Delta\tau}\right)\right\}\Delta\tau$$
$$- \left\{\frac{\partial}{\partial\xi}\left(\frac{1}{J}\widetilde{(\rho U)}\right) + \frac{\partial}{\partial\eta}\left(\frac{1}{J}\widetilde{(\rho V)}\right) + \frac{\partial}{\partial\zeta}\left(\frac{1}{J}\widetilde{(\rho W)}\right)\right\}\Delta\tau + \frac{1}{J}F'_\rho\Delta\tau, \quad (3.5.24)$$

where

$$R_w = -\frac{\partial}{\partial\xi}\left(\frac{1}{J}\rho wU\right) - \frac{\partial}{\partial\eta}\left(\frac{1}{J}\rho wV\right) - \frac{\partial}{\partial\zeta}\left(\frac{1}{J}\rho wW\right) + \frac{1}{J}F'_w, \quad (3.5.25)$$

and $\frac{1}{J}F'_w$, $\frac{1}{J}F'_\rho$ and $\frac{1}{J}F_{\rho\theta_m}$ are the right hand side of Eq. (3.5.3), Eq. (3.5.14) and Eq. (3.5.15), respectively, and

$$\widetilde{(\rho U)} = \xi_x(\rho u)^{\tau+\Delta\tau} + \xi_y(\rho v)^{\tau+\Delta\tau}, \quad (3.5.26)$$
$$\widetilde{(\rho V)} = \eta_x(\rho u)^{\tau+\Delta\tau} + \eta_y(\rho v)^{\tau+\Delta\tau}, \quad (3.5.27)$$
$$\widetilde{(\rho W)} = \zeta_x(\rho u)^{\tau+\Delta\tau} + \zeta_y(\rho v)^{\tau+\Delta\tau}. \quad (3.5.28)$$

Here, we can exclude $(\rho w)^{\tau+\Delta\tau}$ from Eq. (3.5.26) - Eq. (3.5.28) due to the limitation for vertical coordinate to satisfy $\xi_z = \zeta_z = 0$ as mentioned in Subsection 3.5.3.1, which enables the vertical implicit treatment of Eq. (3.5.22) - Eq. (3.5.24). Eliminating $\left(\frac{1}{J}(\rho\theta_m)'\right)^{\tau+\Delta\tau}$ and $\left(\frac{1}{J}\rho'\right)^{\tau+\Delta\tau}$ from Eq. (3.5.22) using Eq. (3.5.23) and Eq. (3.5.24), we obtain the one dimensional Helmholtz type equation of $\omega \equiv \left(\frac{1}{J}\rho w\right)^{\tau+\Delta\tau}$ as

$$-\Delta\tau^2\gamma R_d\pi^t\frac{1}{J}\zeta_z\frac{\partial}{\partial\zeta}\left(J\frac{\partial}{\partial\zeta}(\zeta_z\theta_m^\tau\omega)\right) - \Delta\tau^2 g\frac{\partial}{\partial\zeta}(\zeta_z\omega) + \omega = R, \quad (3.5.29)$$

where

$$R = \left(\frac{1}{J}\rho w\right)^\tau - \gamma R_d\pi^t\Delta\tau\frac{1}{J}\zeta_z\frac{\partial}{\partial\zeta}\left\{(\rho\theta_m)'^\tau + JR'_{\theta_m}\Delta\tau\right\} - \Delta\tau g\left(\frac{1}{J}\rho'^\tau + R'_\rho\Delta\tau\right) + R'_w\Delta\tau, \quad (3.5.30)$$

and

$$R'_w = \frac{\pi'^t}{\bar{\pi}}\frac{\bar{\rho}}{J}g + R_w = -\left(1 - \frac{\pi^t}{\bar{\pi}}\right)\frac{\bar{\rho}}{J}g + R_w, \quad (3.5.31)$$

$$R'_{\theta_m} = -\left\{\frac{\partial}{\partial\xi}\left(\frac{1}{J}\theta_m^\tau\widetilde{(\rho U)}\right) + \frac{\partial}{\partial\eta}\left(\frac{1}{J}\theta_m^\tau\widetilde{(\rho V)}\right) + \frac{\partial}{\partial\zeta}\left(\frac{1}{J}\theta_m^\tau\widetilde{(\rho W)}\right)\right\} + \frac{1}{J}F_{\rho\theta_m}^t, \quad (3.5.32)$$

$$R'_\rho = -\left\{\frac{\partial}{\partial\xi}\left(\frac{1}{J}\widetilde{(\rho U)}\right) + \frac{\partial}{\partial\eta}\left(\frac{1}{J}\widetilde{(\rho V)}\right) + \frac{\partial}{\partial\zeta}\left(\frac{1}{J}\widetilde{(\rho W)}\right)\right\} + \frac{1}{J}F_\rho^t. \quad (3.5.33)$$

Considering $W = 0$ at the upper and lower boundary and $u = 0$, $v = 0$ at the lower boundary, upper and lower boundary conditions are given by $\omega = 0$.

2. Time splitting of vertical advection

Using RK3 as a time integration scheme and a flux limiter function as an advection scheme, the CFL condition of 3-dimensional advection is given by

$$C_\xi + C_\eta + C_\zeta < 1.25, \tag{3.5.34}$$

where C_ξ, C_η and C_ζ are the Courant number in the ξ, η and ζ direction, respectively. As this condition can be hard to fulfill with typhoons characterized by stormy horizontal winds and strong updrafts, time splitting of vertical advection is adopted in consideration of computational efficiency and the model's memory alignment with vertical indices placed innermost.

In the time splitting method, each RK3 stage is divided into substeps depending on the relevant Courant numbers. As each RK3 stage can be regarded as a forward time integration with the time steps of $\Delta t/3$, $\Delta t/2$ and Δt, respectively (as shown in Figure 3.5.1), these time steps are used to evaluate the Courant numbers for each stage. For each column, the number of substeps N is set to satisfy

$$C_\xi + C_\eta + \frac{C_\zeta}{N} < 1.25, \tag{3.5.35}$$

at each RK3 stage. When time splitting is invoked, the forward form integration at each RK3 stage is replaced with RK3 (i.e., RK3 is nested in the original RK3 time integration) as shown in Figure 3.5.2. This involves greater computational cost, but produces the desired higher stability.

① $\phi^* = \phi^n + F^n \frac{1}{3} \Delta t$

② $\phi^{**} = \phi^n + F^* \frac{1}{2} \Delta t$

③ $\phi^{n+1} = \phi^n + F^{**} \Delta t$
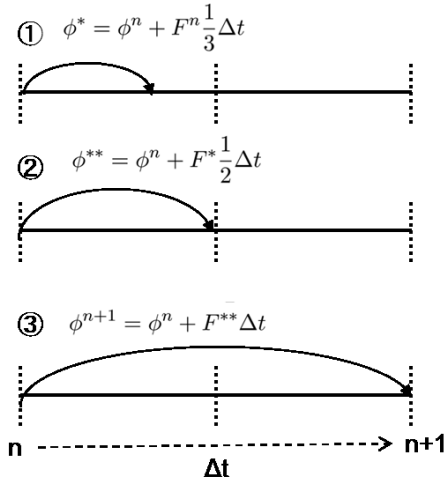
Figure 3.5.1: Schematic of RK3 time integration scheme.
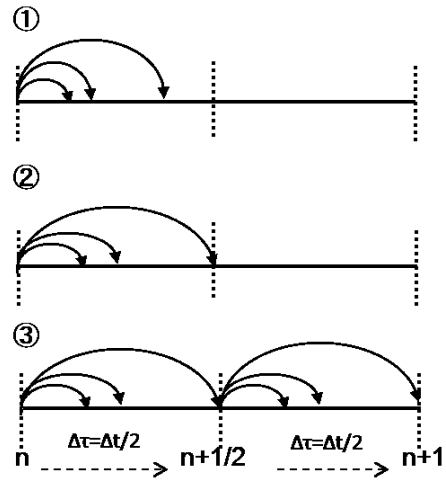
Figure 3.5.2: Schematic of time-splitting of vertical advection. The case needs to split ③ stage into 2 substeps.

When time-splitting is invoked, fields are updated using the horizontal flux F_ξ and F_η first, and the vertical flux F_ζ is then evaluated with the integrated field as follows.

$$\phi^{H*} = \phi^n - \left(\frac{\partial}{\partial \xi} F_\xi{}^n + \frac{\partial}{\partial \eta} F_\eta{}^n \right) \Delta \tau, \tag{3.5.36}$$

$$\phi^{n+1} = \phi^{H*} - \left(\frac{\partial}{\partial \zeta} F_\zeta{}^{H*} \right) \Delta \tau. \tag{3.5.37}$$

3. Time splitting of vertical advection of water substances

To stabilize integration for the vertical advection of water substances with high terminal velocity, a time splitting method is adopted. The short time step $\Delta\tau_1$ for sedimentation is determined from the Courant number $C_{t\zeta}$ as follows.

$$\Delta\tau_1 = \begin{cases} \Delta t & (\max(C_{t\zeta}) \le 1) \\ \beta\dfrac{\Delta t}{\max(C_{t\zeta})} & (\max(C_{t\zeta}) > 1), \end{cases} \tag{3.5.38}$$

where

$$C_{t\zeta} = (W^n + W_{t\alpha}^n)\Delta t/\Delta\zeta. \tag{3.5.39}$$

Here, W^n is W at the time level n, β is a parameter for determining the short time step, and $c = 0.9$ is used.

After time integration with $\Delta\tau_1$, the residual time step is $\Delta t' = \Delta t - \Delta\tau_1$. The next short time step $\Delta\tau_2$ is decided from the Courant number $C_{tz}' = (W^n + W_{t\alpha}^{n+\tau_1})\Delta t'/\Delta\zeta$ and the time integration with $\Delta\tau_2$ is calculated. This procedure is repeated until no residual time step is left.

3.5.3.4 Boundary Conditions

Rayleigh damping,

$$D_R = -n(x, y, z)\{\phi - \phi_{EXT}\}, \quad n(x, y, z) = max\left(\frac{D}{m_L}, \frac{D}{m_U}\right), \tag{3.5.40}$$

is added near the lateral and upper boundaries to the time tendencies of horizontal and vertical momentum, potential temperature and the mixing ratio of water vapor, where ϕ is the prognostic variable and ϕ_{EXT} is the value of the external model. m_L and m_U represent coefficients that determine the 1/e-folding time for the lateral and upper boundaries, respectively, while $m_L = 250$ seconds and $m_U = 125$ seconds. The location-based function D is unity at the boundary and decreases with subsequent grid point distance.

3.5.4 Cloud Microphysics

An explicit three-ice bulk microphysics scheme (Ikawa and Saito 1991) based on Lin *et al.* (1983) is incorporated. The scheme predicts the mixing ratios of water vapor and five hydrometeors designated by q_x where x denotes categories defined as v for water vapor, w for cloud water, r for rain, i for cloud ice, s for snow, and g for graupel. The cloud microphysical processes simulated in this scheme are illustrated in Figure 3.5.3 (see Table 3.5.1 for a list of symbols used in the figure). In this scheme, some basic cloud microphysical processes (e.g., nucleation of cloud particles, conversion from cloud particles to precipitation particles) are parameterized because the related processes occur within a shorter time than the integration time step. However, most of the cloud microphysical processes can be applied directly to calculation related to the size distribution assumed in each hydrometeor category.

The number-weighted mean of the temporal tendency of one cloud microphysical variable ϕ relating to one cloud microphysical process in each particle gives the grid-mean temporal tendency of ϕ as

$$\frac{d\phi}{dt} = \int_0^\infty \frac{d\phi_0(D)}{dt}n(D)\,dD, \tag{3.5.41}$$

where $\frac{d\phi_0(D)}{dt}$ is the temporal tendency of ϕ relating to one cloud microphysical process in a particle with diameter D, and $n(D)\,dD$ is the number of particles per unit volume of air with diameters from D to $D + dD$. Hydrometeor size distribution therefore significantly affects time tendency of cloud microphysical variables relating to cloud microphysical processes.

3.5.4.1   Mass-size Relationships

The mass-size relationships represent particle mass m_x as a function of particle diameter D_x for determination of mixing ratios or mass weighted-mean variables. For example, the mixing ratio q_x is generally formulated as

$$q_x = \frac{1}{\rho_a} \int_0^\infty m_x(D_x) n_x(D_x) dD_x, \tag{3.5.42}$$

where ρ_a is the density of air.

The mass-size relationship ($m_x(D_x)$) with the power-law is formulated as

$$m_x(D_x) = a_x D_x^{b_x}. \tag{3.5.43}$$

For the category of cloud ice and snow, a_x and b_x (x for i and s) are set to $0.0185 \text{kg m}^{-1.9}$ and 1.9 respectively (Brown and Francis 1995). Particle sphericity ($b_x = 3$) is assumed in the hydrometer categories of graupel, rain and cloud water, and density is constant in each category (ρ_x). Accordingly, the mass-size relationship is formulated as

$$m_x(D_x) = \frac{\pi}{6}\rho_x D_x^{\,3}. \tag{3.5.44}$$

3.5.4.2   Size Distribution Functions

1. **Rain, cloud ice and graupel**
   The size distributions of rain, cloud ice and graupel are assumed to follow an exponential function:

$$n_x(D_x) = N_{0x} \exp(-\lambda_x D_x), \tag{3.5.45}$$

where N_{0x} is the intercept and λ_x is the slope parameter of the size distribution. Accordingly, the moment formula for rain, cloud ice and graupel is calculated as

$$M_x(p) = \int_0^\infty D_x^{\,p} n_x(D_x) \, dD_x = N_{0x} \frac{\Gamma(1+p)}{\lambda_x^{1+p}}, \tag{3.5.46}$$

where Γ is the gamma function and $M_x(p)$ is the p-th moment of $n_x(D_x)$. The number concentration N_x is the 0-th moment of $n_x(D_x)$, and is therefore calculated as

$$N_x = \int_0^\infty n_x(D_x) \, dD_x = M_x(0) = \frac{N_{0x}}{\lambda_x}. \tag{3.5.47}$$

The mixing ratio q_x is calculated using $m_x(D_x)$ as

$$q_x = \frac{1}{\rho_a} \int_0^\infty m_x(D_x) n_x(D_x) \, dD_x = \frac{aN_{0x}}{\rho_a} \frac{\Gamma(1+b_x)}{\lambda_x^{1+b_x}}. \tag{3.5.48}$$

The intercepts N_{0x} are assumed to be constant or dependent only on temperature for cloud ice. The slope parameter is therefore expressed:

$$\lambda_x = \left(\frac{a_x N_{0x} \Gamma(1+b_x)}{\rho_a q_x} \right)^{\frac{1}{1+b_x}}. \tag{3.5.49}$$

2. **Snow**
   The size distribution function itself is not directly used for snow, but moments are parameterized based on Field *et al.* (2007) as follows:

$$M_s(p) = \int_0^\infty D_s^{\,p} n_s(D_s) \, dD_s = A(p) \exp\left[B(p) T_c\right] M_s^{c(p)}(2), \tag{3.5.50}$$

$$A(p) = \exp\left[13.6 - 7.76p + 0.479p^2\right], \tag{3.5.51}$$

$$B(p) = -0.0361 + 0.0151p + 0.00149p^2, \qquad (3.5.52)$$

$$C(p) = 0.807 + 0.00581p + 0.0457p^2, \qquad (3.5.53)$$

where T_c is the temperature in celsius (°C).

The number concentration N_s, the 0-th moment of $n_s(D_s)$, is calculated as

$$N_s = M_s(0) = A(0)\exp[B(0)\,T_c]\,M_s^{c(0)}(2). \qquad (3.5.54)$$

Based on (3.5.43), the mixing ratio q_s is

$$q_s = \frac{1}{\rho_a}\int_0^\infty m_s(D_s)n_s(D_s)\,dD_s = \frac{1}{\rho_a}a_s M_s(b_s) = \frac{1}{\rho_a}a_s A(b_s)\exp[B(b_s)(T_c)]\,M_s^{c(b_s)}(2). \qquad (3.5.55)$$

Accordingly, the second moment $M_s(2)$ is calculated as

$$M_s(2) = \left[\frac{\rho_a q_s}{a_s}\frac{1}{A(b_s)\exp[B(b_s)\,T_c]}\right]^{\frac{1}{c(b_s)}}. \qquad (3.5.56)$$

3. **Cloud water**

As cloud water is assumed to be monodisperse, its size distribution follows the δ-function:

$$n_w(D_w) = N_w\delta(D_w - \overline{D_w}), \qquad (3.5.57)$$

where $\delta(x)$ satisfies the equation $\int_{-\infty}^\infty \delta(x - a)f(x)\,dx = f(a)$ and $\overline{D_w}$ represents the diameter of the monodisperse particle. The moment formula for cloud water is given by

$$M_w(p) = N_w\overline{D_w}^p. \qquad (3.5.58)$$

The number concentration of cloud water N_w is always assumed to be constant and is set to 1.0×10^8 m^{-4} in this scheme.

The mixing ratio is calculated as

$$q_w = \frac{\rho_w}{\rho_a}\frac{\pi}{6}M_w(3) = \frac{\rho_w}{\rho_a}\frac{\pi}{6}N_w\overline{D_w}^3. \qquad (3.5.59)$$

The diameter is therefore determined as

$$\overline{D_w} = \left(\frac{6\rho_a q_w}{\pi\rho_w N_w}\right)^{\frac{1}{3}}. \qquad (3.5.60)$$

3.5.4.3 Fall Velocity and Sedimentation

The simple power law is adopted for the fall velocity-size relationship ($U_x(D_x)$) given by

$$U_x(D_x) = \alpha_{ux}D_x^{\beta_{ux}}\left(\frac{\rho_0}{\rho_a}\right)^{\gamma_{ux}}, \qquad (3.5.61)$$

where ρ_0 is the density of the reference air, and α_{ux}, β_{ux} and γ_{ux} are constants in each hydrometeor category. The forecast model for the MSM calculates sedimentation processes for hydrometers in its dynamical core. The cloud microphysics scheme diagnoses mass-weighed mean fall velocities as terminal velocities W_{tx}:

$$W_{tx} = \frac{\int_0^\infty U_x(D_x)m_x(D_x)n_x(D_x)\,dD_x}{\int_0^\infty m_x(D_x)n_x(D_x)\,dD_x}. \qquad (3.5.62)$$

The cloud microphysics scheme passes W_{tx} to the dynamical core.

Table 3.5.2 shows the characteristics of each hydrometeor class. More information on the treatment of each cloud microphysical process in this scheme can be found in the references.

Table 3.5.1: List of symbols in Figure 3.5.3

Notation	Description
	Production terms
p_a__ppp_b	Production of category "a" converted from category "b" via the process "ppp"
p_a__ppp_a_b	Growth of category "a" based on capture of category "b" via the process "ppp"
p_a__ppp_b_c	Generation of category "a" based on category "b" capturing category "c" via the process "ppp"
	Categories by hydrometeor
v	Water vapor
w	Cloud water
r	Rain
i	Cloud ice
s	Snow
g	Graupel
	Cloud microphysical processes
evp	Evaporation
cnd	Condensation
aut, cn	Conversion
ac	Accretion
mlt	Melting
nud	Nucleation
dep	Deposition
sub	Sublimation
frz	Freezing

Table 3.5.2: Assumed hydrometeor parameters and characteristics

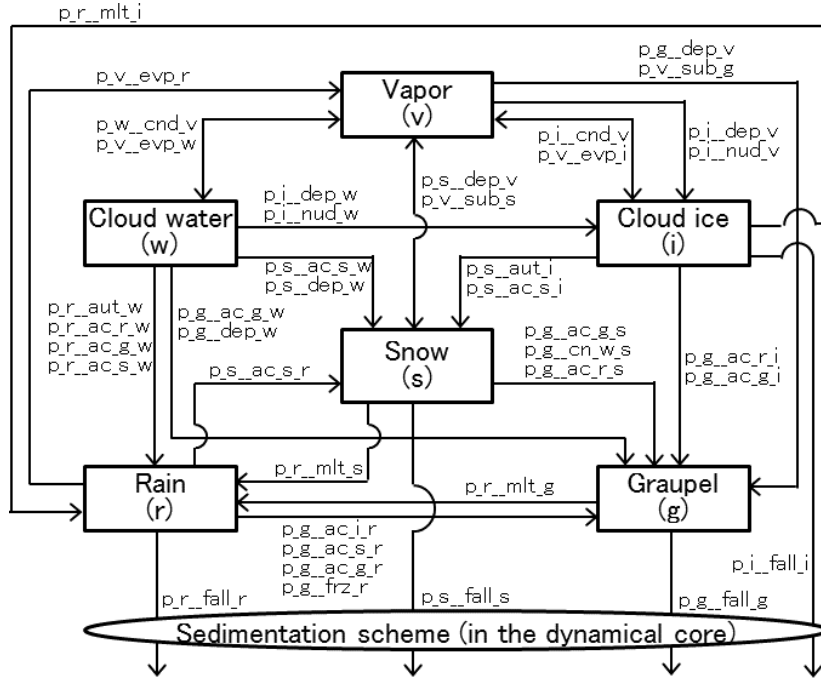| Variable	Rain q_r[kg kg^{-1}]	Snow q_s[kg kg^{-1}]	Graupel q_g[kg kg^{-1}]	Cloud ice q_i[kg kg^{-1}]	Cloud water q_w[kg kg^{-1}]
Size distribution [m^{-4}]	$n_r(D_r) =$ $N_{0r}\exp(-\lambda_r D_r)$ $N_{0r} = 8.0 \times 10^6$	not directly used	$n_g(D_g) =$ $N_{0g}\exp(-\lambda_g D_g)$ $N_{0g} = 1.1 \times 10^6$	$n_i(D_i) =$ $N_{0i}\exp(-\lambda_i D_i)$ $N_{0i} = N_{00i}\exp(-0.12T_c)$ $N_{00i} = 4.0 \times 10^7$ $T_c = \max(T_c, -40°\text{C})$	monodisperse, $\overline{D_w} = \left[\dfrac{6q_w\rho_a}{\pi N_w\rho_w}\right]^{\frac{1}{3}}$ $N_w = 1.0 \times 10^8$
Mass[kg]-size[m] relationship	$m_r = \frac{\pi}{6}\rho_r D_r^3$	$m_s = 0.0185 D_s^{1.9}$	$m_g = \frac{\pi}{6}\rho_g D_g^3$	$m_i = 0.0185 D_i^{1.9}$	$m_w = \frac{\pi}{6}\rho_w D_w^3$
Density [kg m^{-3}]	$\rho_r = 1.0 \times 10^3$	not used	$\rho_g = 3.0 \times 10^2$	not used	$\rho_w = 1.0 \times 10^3$
Fall velocity [m/s]	$\alpha_{ur} = 842$ $\beta_{ur} = 0.8$ $\gamma_{ur} = 0.5$	$\alpha_{us} = 17$ $\beta_{us} = 0.5$ $\gamma_{us} = 0.5$	$U_x(D_x) = \alpha_{ux}D_x^{\beta_{ux}}\left(\frac{\rho_0}{\rho_a}\right)^{\gamma_{ux}}$ $\alpha_{ug} = 124$ $\beta_{ug} = 0.64$ $\gamma_{ug} = 0.5$	$\alpha_{ui} = 71.34$ $\beta_{ui} = 0.6635$ $\gamma_{ui} = 0.5$	not considered

Figure 3.5.3: Cloud microphysical processes in the MSM. For a list of symbols, see Table 3.5.1.

3.5.5 Convective Parameterization

A temporal tendency of a grid mean value ϕ associated with subgrid convection under the isobaric coordinate is generally described as

$$\rho\left(\frac{\partial\overline{\phi}}{\partial t}\right)_{\text{convection}} = \rho g\frac{\partial\rho\overline{\phi'w'}}{\partial p} + S_{\phi}, \tag{3.5.63}$$

where $\overline{\phi'w'}$ and S_{ϕ} represent a subgrid transport flux and a source term respectively. To parameterize the subgrid flux and source term for heat and moisture, a mass flux convective parameterization based on the Kain-Fritsch (KF) (Kain and Fritsch 1990; Kain 2004) type scheme is employed in the MSM.

3.5.5.1 Cloud Model

The scheme parameterizes convection using a cloud model based on a one-dimensional entraining/detraining plume model incorporating detailed treatment for interactions between convective updraft and the surrounding air. The cloud model consists of an updraft mass flux representing the convective activity within a column. Downdraft is not treated in the scheme. The cloud model involves the assumption that the convective updraft area is in a steady state. Thus, mass conservation is represented as

$$0 = \rho g\frac{\partial M^u}{\partial p} + E^u - D^u, \tag{3.5.64}$$

where M, E and D represent convective mass flux, and entrainment / detrainment from / to environmental air respectively. The superscript u shows updraft. For ϕ, the steady state equations can be represented as

$$0 = \rho g\frac{\partial M^u\phi^u}{\partial p} + E^u\overline{\phi} - D^u\phi^u + S_{\phi}^{u}. \tag{3.5.65}$$

The scheme also employs the assumption that the area of convection is small enough relative to that of a grid-box. Based on this assumption, the subgrid flux can be represented as

$$\rho\overline{\phi'w'} = M^u\left(\phi^u - \overline{\phi}\right). \tag{3.5.66}$$

111

Substituting Eq. (3.5.64), Eq. (3.5.65) and Eq. (3.5.66) into Eq. (3.5.63), the temporal tendency of ϕ due to subgrid convection can be re-written as a summation of the detrainment and compensating subsidence terms:

$$\rho \left(\frac{\partial \overline{\phi}}{\partial t} \right)_{\text{convection}} = D^u \left(\phi^u - \overline{\phi} \right) - \rho g M^u \frac{\partial \overline{\phi}}{\partial p}. \tag{3.5.67}$$

3.5.5.2 Determination of Variables in Updraft

Vertical integration with Eq. (3.5.64) and Eq. (3.5.65) from the lifting condensation level (LCL), is applied to determine ϕ^u and vertical profiles of M^u. During this integration, E^u and D^u, representing entrainment and detrainment, are calculated with consideration of the mixing process between the updraft and environmental air.

Following the original KF scheme (Kain and Fritsch 1990), the interaction between updraft and the environment associated with the turbulent mixing is estimated at each vertical model level to determine E^u and D^u. It is assumed that the turbulent mixing occurs very near the periphery of the updraft, and that large number of subparcel-like mixtures of the updraft and the environment form at various ratios that can be described by a Gaussian probability distribution function the mean of with a mean of 0.5, representing a scenario in which environmental mass and updraft mass are likely to be equally mixed in subparcels.

The relationship linking δM_e, δM_u and δM_t, defined as the entrained mass from the environment, the updraft mass mixed with the entrained mass and the total mass respectively, can be expressed as

$$\delta M_u + \delta M_e = \delta M_t = \delta M_t \int_0^1 f(x)dx, \tag{3.5.68}$$

$$\delta M_e = \delta M_t \int_0^1 x f(x)dx, \tag{3.5.69}$$

$$\delta M_u = \delta M_t \int_0^1 (1-x)f(x)dx, \tag{3.5.70}$$

where x and $f(x)$ are the fraction of environmental mass in mixed subparcels and the probability distribution function as a function of x respectively.

δM_e, which determines the amounts of entrainment and detrainment, is inversely proportional to the updraft radius, R:

$$\delta M_e = M_{u0}(a\delta P/R), \tag{3.5.71}$$

where δP is the vertical grid thickness in the pressure coordinate, and the factor a is set to 0.03 m Pa^{-1} as a constant. The radius of the updraft is used only for entrainment rate estimation. The radius R is set to a constant of 750 m.

Consequently, mixtures with positive buoyancy against the environment entrain into updraft, while those with negative buoyancy detrain from it. When x_n is the fraction with which mixed air is neutral against environmental air, E^u and D^u can be formulated as follows:

$$E^u \delta p = \rho g \delta M_t \int_0^{x_n} x f(x)dx, \tag{3.5.72}$$

$$D^u \delta p = \rho g \delta M_t \int_{x_n}^1 (1-x)f(x)dx. \tag{3.5.73}$$

The vertical velocity of the updraft depends on buoyancy and hydrometeor weights. The updraft terminates when the mass flux becomes emaciated through detrainment or when its vertical velocity vanishes.

In the scheme, parameterized convection is divided into deep and shallow convection types. An updraft that does not reach the minimum cloud depth for deep convection is regarded as shallow convection. The minimum cloud depth is a function of temperature at the cloud base (LCL).

3.5.5.3 Treatment of convective precipitation

For cloud water content q_c, Eq. (3.5.65) applies as follows:

$$0 = \rho g \frac{\partial M^u q_c^u}{\partial p} + E^u \overline{q_c} - D^u q_l^u + c_c^u - P_c, \tag{3.5.74}$$

where $c_c^u [\text{kg m}^{-3} \text{s}^{-1}]$ and $P_c [\text{kg m}^{-3} \text{s}^{-1}]$ are condensation/glaciation and precipitation generation terms respectively. In updraft evaluation, water condensate /glaciate (depending on updraft temperature at each level) are considered.

The precipitation generation rate is formulated as a Kessler type autoconversion scheme:

$$P_c = A \max (q_c^u - q_{c0}, 0) . \tag{3.5.75}$$

The threshold q_{c0} is set to a constant value of $2.0 \times 10^{-3} \text{kg kg}^{-1}$. The conversion rate A is set to $\rho g M^u / \Delta p$ so that excess hydrometeors over the threshold are immediately taken out of the updraft as precipitation. The generated precipitation is added to the tendencies shown as per Eq. (3.5.67) for rain, snow and graupel rather than being represented as falling to the ground. The precipitation fall process is calculated in a sedimentation scheme outside the convective parameterization scheme.

3.5.5.4 Closure

The closure process finally determines the magnitude of convective mass flux. Closure is the only difference between deep and shallow convection.

For deep convection, the magnitude of mass flux is determined so that stabilized vertical profiles after convection satisfy the condition that CAPE in the final state should be less than 15% of the initial value. Seeking the stabilized state usually requires iterative adjustment of mass fluxes. The updraft mass flux at the LCL, $M_{u0} [\text{kgm}^{-2} \text{s}^{-1}]$, is initially given as follows with the assumption that vertical velocity w_{one} is 1 m/s and the initial area occupied by convection is 1 % of a grid:

$$M_{u0} = 0.01 \rho_{u\text{LCL}} w_{\text{one}}, \tag{3.5.76}$$

where $\rho_{u\text{LCL}}$ is the density of the updraft mass flux at the LCL. Using M_{u0}, the vertical integration of Eqs. (3.5.64) and (3.5.65) from the LCL are calculated. The value of $\overline{\phi}_{\text{stabilized}}$, the grid mean $\overline{\phi}$ after stabilization, is then calculated based on time integration of Eq. (3.5.67) with the period of the lifetime of convection τ_{lifetime}. If the post-stabilization CAPE is still 15 % more than the initial value, the mass flux at the LCL is increased. Iterating this process, the final value of M_{u0} is determined.

For shallow convection, the mass flux at the LCL is determined using the maximum turbulent kinetic energy (TKE),

$$M_{u0,\text{shallow}} = \frac{\text{TKE}_{\text{max}}}{k_0} \frac{\Delta p_{\text{parcel}}}{g \tau_{\text{lifetime}}}, \tag{3.5.77}$$

where TKE_{max} is the maximum value of TKE and is set to $1 \text{ m}^2 \text{ s}^{-2}$ for the MSM. k_0 is set to $20 \text{ m}^2 \text{ s}^{-2}$. Δp_{parcel} [Pa] is the pressure depth from the LCL to the highest model level at which the depth is no larger than 50 hPa.

The temporal tendency of the adjusted physical quantity ϕ can be determined as

$$\left. \frac{d\overline{\phi}}{dt} \right|_{\text{convection}} = \frac{\overline{\phi}_{\text{stabilized}} - \overline{\phi}_{\text{initial}}}{\tau_{\text{lifetime}}}, \tag{3.5.78}$$

where τ_{lifetime} is set to a constant value of 600 s.

3.5.5.5 Diagnosis of the Convection as a Triggering Process

Diagnosis is performed to determine whether each column is convectively unstable enough to activate the scheme. This is done for every timestep to identify grids where parameterized convection should occur, and involves two steps.

Firstly, the temperature of a lifted parcel is compared with the environmental temperature $\overline{T}$. The parcel temperature T_{diag} is defined as the lifted air mass at the LCL T_{LCL} with a perturbation:

$$T_{\text{diag}} = T_{\text{LCL}} + \Delta T'. \tag{3.5.79}$$

The second term on the right represents perturbation corresponding to subgrid-scale buoyant flux associated with the planetary boundary layer process.

$$\Delta T' = \max \left[A_{\text{plume}}, \min \left[B_{\text{plume}} \sigma_{T_v}, G_{\text{max}} z_h \right] \right] \Pi, \tag{3.5.80}$$

$$\sigma_{T_v} = 1.93 \overline{w' \theta'_{vs}} / w_m, \tag{3.5.81}$$

$$w_m^3 = u_*^3 + 0.25 z_h \overline{w' b'_s}, \tag{3.5.82}$$

where Π, z_h, u^* and $\overline{w' b'_s}$ are the Exner function, the height of the planetary boundary layer, friction velocity and turbulent buoyant flux at the surface respectively. The parameters are set to $A_{\text{plume}} = 0.2$ K, $B_{\text{plume}} = 3.26$ and $G_{\text{max}} = 10^{-3}$ Km^{-1}. The diagnosis process lifts the potential updraft source layer (USL) of the lowest 50 hPa depth adiabatically to its LCL for determination of T_{LCL}. If $T_{\text{diag}} > \overline{T}$ is not satisfied, the base of the potential USL is moved up to the next model level and comparison of T_{diag} with $\overline{T}$ is repeated as long as the base of the potential USL is below the lowest 300 hPa of the atmosphere.

As the second step of diagnosis, if $T_{\text{diag}} > \overline{T}$ is satisfied, the scheme calculates CAPE. To determine this value, the updraft variables are provisionally calculated by vertically integrating Eq. (3.5.64) and Eq. (3.5.65). If the updraft parcel has a positive CAPE value, parameterized convection is activated in the column.

3.5.6 Radiation

The radiation process employed in the MSM is almost identical to that in the GSM, as the codes of the GSM radiation process were ported into the MSM. The details are described in Subsection 3.2.3. Some differences are outlined below.

3.5.6.1 Radiatively Active Constituents

Radiatively active gases accounted for in the MSM are identical to those in the GSM, although certain representations of optical properties differ. Some gas concentrations differ (O_3:375 ppmv, CH_4:1.75 ppmv, N_2O:0.28 ppmv) and aerosol optical depth climatology is based on total-column values from MODerate resolution Imaging Spectroradiometer (MODIS) and Total Ozone Mapping Spectrometer (TOMS) observations with seasonal variations. Other optical properties of aerosols are specified as continental and maritime background values without seasonal variation.

3.5.6.2 Cloud Properties

The effective radius of cloud ice particles $r_{\text{e}}[\mu\text{m}]$ is diagnosed using a linearized equation based on Ou and Liou (1995):

$$r_{\text{e}} = \begin{cases} 20 & T < -60 \\ 20 + \dfrac{130(T + 60)}{40} & -60 \leq T \leq -20 \\ 150 & -20 < T \end{cases}, \tag{3.5.83}$$

where T [°C] is the air temperature. The effective radius of cloud water droplets is fixed at 15 μm.

Cloud optical properties for short-wave radiation are parameterized following Slingo (1989) for liquid droplets and Ebert and Curry (1992) for ice particles. Cloud optical thickness for long-wave radiation is parameterized as per Hu and Stamnes (1993) for liquid droplets and as per Ebert and Curry (1992) for ice particles.

3.5.6.3 Cloud Fraction

The cloud fraction for the radiation scheme is diagnosed using a partial condensation method based on Sommeria and Deardorff (1977) and Mellor (1977), which is also employed to evaluate subgrid scale buoyancy flux in the boundary layer scheme (Subsection 3.5.7). This method involves calculation to determine the variance of the gridbox saturation deficit, associated with fluctuations of liquid water potential temperature (θ_1') and total water specific humidity (q_w'). Assuming unimodal Gaussian distribution for the deficit, the liquid cloud fraction (R_1) and the gridbox mean liquid water content ($\overline{q_1}$) are given by

$$R_1 = \frac{1}{\sqrt{2\pi}(2\sigma_s)} \int_0^\infty \exp\left[-\frac{(q_1 - a_1\Delta\overline{q})^2}{2(2\sigma_s)^2}\right] dq_1 = \frac{1}{2}\left[1 + \mathrm{erf}\left(\frac{Q_1}{\sqrt{2}}\right)\right], \tag{3.5.84}$$

$$\overline{q_1} = \frac{1}{\sqrt{2\pi}(2\sigma_s)} \int_0^\infty q_1 \exp\left[-\frac{(q_1 - a_1\Delta\overline{q})^2}{2(2\sigma_s)^2}\right] dq_1 = 2\sigma_s\left[R_1 Q_1 + \frac{1}{\sqrt{2\pi}}\exp\left(-\frac{Q_1^2}{2}\right)\right], \tag{3.5.85}$$

where $\Delta\overline{q} = \overline{q_w} - q_{sat}(\overline{T_1})$, T_1 denotes the liquid water temperature, and $q_{sat}(T)$ is saturated specific humidity at the temperature (T). a_1 and Q_1 are given by

$$a_1 = \left[1 + \frac{L}{C_p}\left(\frac{\partial q_{sat}}{\partial T}\right)_{T=T_1}\right]^{-1}, \tag{3.5.86}$$

$$Q_1 = \frac{a_1\Delta\overline{q}}{2\sigma_s}, \tag{3.5.87}$$

where L denotes the latent heat of condensation and C_p is specific heat at the constant pressure of dry air, and σ_s is a half of the standard deviation of the saturation deficit. σ_s can be represented using the turbulent prognostic variables ($\overline{\theta_1'^2}$, $\overline{q_w'^2}$, and $\overline{\theta_1' q_w'}$) in the boundary layer scheme (Subsection 3.5.7) as follows:

$$\sigma_s^2 = \frac{1}{4}\left(a_1^2 \overline{q_w'^2} - 2a_1 b_1 \overline{\theta_1' q_w'} + b_1^2 \overline{\theta_1'^2}\right), \tag{3.5.88}$$

$$b_1 = a_1 \Pi \left(\frac{\partial q_{sat}}{\partial T}\right)_{T=T_1}, \tag{3.5.89}$$

where Π is the Exner function.

For parametrizing the ice cloud fraction, a pragmatic approach based on Wilson and Ballard (1999) is employed. The ice cloud fraction R_i is given by

$$R_i = \begin{cases} 0 & \dfrac{\overline{q_f}}{b_{si}} = 0 \\[2mm] \dfrac{1}{2}\left(6\dfrac{\overline{q_f}}{b_{si}}\right)^{2/3} & 0 < \dfrac{\overline{q_f}}{b_{si}} \leq \dfrac{1}{6} \\[2mm] 1 - 4\cos^2\phi & \dfrac{1}{6} < \dfrac{\overline{q_f}}{b_{si}} \leq 1 \\[2mm] 1 & 1 < \dfrac{\overline{q_f}}{b_{si}} \end{cases}, \tag{3.5.90}$$

where $\overline{q_f}$ is the gridbox mean ice water content including snow aggregates. b_{si} and ϕ are given by

$$b_{si} = 2\sqrt{6}\sigma_s, \tag{3.5.91}$$

$$\phi = \frac{1}{3}\left\{\cos^{-1}\left[\frac{3}{2\sqrt{2}}\left(1 - \frac{\overline{q_f}}{b_{si}}\right)\right] + 4\pi\right\}. \tag{3.5.92}$$

A total cloud fraction R is obtained by combination of liquid and ice cloud fraction. Assuming that the liquid and ice clouds are minimally overlapped, R is given by

$$R = R_1 + R_i - \min\langle R_1, R_i\rangle. \tag{3.5.93}$$

3.5.6.4   Radiative Timesteps

Long-wave and short-wave radiation schemes are fully calculated every 15 minutes, while heating rates associated with long-wave and short-wave radiation are corrected at every time step using the surface temperature and the solar zenith angle, respectively.

3.5.7   Boundary Layer

The boundary layer scheme represents vertical turbulent transport of momentum, heat and water. The fluxes exhibit the temporal tendency of the variable $\phi(= u, v, \theta_1, q_w)$ associated with turbulent transport as follows:

$$\frac{\partial \phi}{\partial t} = -\frac{\partial}{\partial z}\overline{w'\phi'}. \tag{3.5.94}$$

The MSM employs the Mellor-Yamada-Nakanishi-Niino Level 3 model (MYNN3) (Nakanishi and Niino 2009) as a boundary layer scheme. This is a second order turbulent closure model in which it is assumed that the third-order moments of turbulent fluctuation can be depicted by lower-order moments.

3.5.7.1   Prognostic Equations and Fluxes

In the MYNN3 with boundary layer approximation, in which horizontal derivatives are ignored, just only four turbulent prognostic variables (including turbulent kinetic energy (TKE)), remain:

$$\frac{\partial q^2}{\partial t} = -2\left(\overline{u'w'}\frac{\partial \overline{u}}{\partial z} + \overline{v'w'}\frac{\partial \overline{v}}{\partial z}\right) + 2\frac{g}{\overline{\theta_v}}\overline{w'\theta_v'} - 2\varepsilon + \frac{\partial}{\partial z}\left(q\ell S_q \frac{\partial q^2}{\partial z}\right), \tag{3.5.95}$$

$$\frac{\partial \overline{\theta_1'^2}}{\partial t} = -2\overline{w'\theta_1'}\frac{\partial \overline{\theta_1}}{\partial z} - 2\varepsilon_\theta + \frac{\partial}{\partial z}\left(q\ell S_\theta \frac{\partial \overline{\theta_1'^2}}{\partial z}\right), \tag{3.5.96}$$

$$\frac{\partial \overline{q_w'^2}}{\partial t} = -2\overline{w'q_w'}\frac{\partial \overline{q_w}}{\partial z} - 2\varepsilon_q + \frac{\partial}{\partial z}\left(q\ell S_{q_w} \frac{\partial \overline{q_w'^2}}{\partial z}\right), \tag{3.5.97}$$

$$\frac{\partial \overline{\theta_1'q_w'}}{\partial t} = -\overline{w'\theta_1'}\frac{\partial \overline{q_w}}{\partial z} - \overline{w'q_w'}\frac{\partial \overline{\theta_1}}{\partial z} - 2\varepsilon_{\theta q} + \frac{\partial}{\partial z}\left(q\ell S_{\theta q} \frac{\partial \overline{\theta_1'q_w'}}{\partial z}\right), \tag{3.5.98}$$

where q^2 is a doubled TKE value, θ_1 the liquid water potential temperature, q_w the total water content, and ℓ the mixing length (see Subsection 3.5.7.4). $\overline{\phi}$ represents an ensemble-averaged ϕ, and ϕ' is the turbulent fluctuation of ϕ. The buoyancy flux, $(g/\overline{\theta_v})\overline{w'\theta_v'}$, and the dissipation terms ε_X are described in Subsections 3.5.7.2 and 3.5.7.3, respectively. Here, q_1 is the mixing ratio of liquid water (including the ice phase), and

$$q^2 = \left(\overline{u'^2} + \overline{v'^2} + \overline{w'^2}\right), \tag{3.5.99}$$

$$\theta_1 = \theta - \frac{L}{C_p}\frac{\theta}{T}q_1, \tag{3.5.100}$$

$$q_w = q_v + q_1, \tag{3.5.101}$$

where L denotes the latent heat of condensation and C_p specific heat at the constant pressure of dry air. The turbulent fluxes are diagnosed as

$$\overline{u'w'} = -q\ell(S_{M2.5} + S'_M)\frac{\partial \overline{u}}{\partial z}, \tag{3.5.102}$$

$$\overline{v'w'} = -q\ell(S_{M2.5} + S'_M)\frac{\partial \overline{v}}{\partial z}, \tag{3.5.103}$$

$$\overline{w'\theta_1'} = -q\ell(S_{H2.5} + S'_H)\frac{\partial \overline{\theta_1}}{\partial z}, \tag{3.5.104}$$

$$\overline{w'q'_w} = -q\ell(S_{H2.5} + S'_H)\frac{\partial \overline{q_w}}{\partial z}, \tag{3.5.105}$$

where S_X and S'_X are non-dimensional diffusion coefficients (see Subsection 3.5.7.5).

Once the prognostic equations (3.5.95), (3.5.96), (3.5.97), and (3.5.98) are integrated, the fluxes in Eqs. (3.5.102), (3.5.103), (3.5.104), and (3.5.105) and the tendencies of the turbulent prognostic variables can be calculated.

3.5.7.2 Buoyancy Flux

Buoyancy flux $(g/\overline{\theta_v})\overline{w'\theta'_v}$ is a major origin of TKE production. With consideration of partial condensation effects assuming that the fluctuations of θ_1 and q_w from their mean values is expressed by the Gaussian probability density function (PDF) (Sommeria and Deardorff 1977), the width of which depends on $\overline{\theta'^2_1}$, $\overline{q'^2_w}$ and $\overline{\theta'_1 q'_w}$, the buoyancy flux can be written as a function of the cloud fraction (R) and the gridbox mean liquid water content ($\overline{q_1}$) determined as moments of the PDF (see Subsection 3.5.6). Following Sommeria and Deardorff (1977) and Mellor (1977), the value is given by

$$\frac{g}{\theta_v}\overline{w'\theta'_v} = \frac{g}{\theta_v}\left(\beta_\theta \overline{w'\theta'_1} + \beta_q \overline{w'q'_w}\right), \tag{3.5.106}$$

$$\beta_\theta = 1 + 0.61\overline{q_w} - 1.61\overline{q_1} - \widetilde{R}a_1 b_1 c_1, \tag{3.5.107}$$

$$\beta_q = 0.61\overline{\theta} + \widetilde{R}a_1 c_1, \tag{3.5.108}$$

$$\widetilde{R} = R - \frac{\overline{q_1}}{2\sigma_s}\frac{1}{\sqrt{2\pi}}\exp\left(-\frac{Q_1^2}{2}\right), \tag{3.5.109}$$

$$c_1 = (1 + 0.61\overline{q_w} - 1.61\overline{q_1})\frac{\overline{\theta}}{T}\frac{L}{C_p} - 1.61\overline{\theta}. \tag{3.5.110}$$

Here, a_1, b_1, σ_s and Q_1 are given by Eqs. (3.5.86), (3.5.89), (3.5.88), and (3.5.87).

3.5.7.3 Dissipation Terms

The dissipation terms ε_X appearing in the equations are parameterized on the basis of Kolmogorov's local isotropy assumption as

$$\varepsilon = \frac{q}{B_1\ell}q^2, \quad \varepsilon_\theta = \frac{q}{B_2\ell}\overline{\theta'^2_1}, \quad \varepsilon_q = \frac{q}{B_2\ell}\overline{q'^2_w}, \quad \varepsilon_{\theta q} = \frac{q}{B_2\ell}\overline{\theta'_1 q'_w}, \tag{3.5.111}$$

with the closure constants B_1 and B_2 (Nakanishi and Niino 2009).

3.5.7.4 Mixing Lengths

The formulation of mixing length ℓ is based on the original work of Nakanishi and Niino (2009), but modified partially. ℓ is defined by blending three length scales as

$$\frac{1}{\ell^2} = \frac{1}{L_S^2} + \frac{1}{L_T^2} + \frac{1}{L_B^2}, \tag{3.5.112}$$

where

$$L_S = \begin{cases} kz/3.7 & (\zeta \geq 1) \\ kz(1 + 2.7\zeta)^{-1} & (0 \leq \zeta < 1) \\ kz(1 - 10\zeta)^{0.2} & (\zeta < 0) \end{cases}, \tag{3.5.113}$$

$$L_B = \begin{cases} q/N_1 & (\partial\theta/\partial z > 0, \zeta \geq 0) \\ \left[1 + 5w_L(q_c/L_T N_1)^{1/2}\right]q/N_1 & (\partial\theta/\partial z > 0, \zeta < 0) \\ \infty & (\partial\theta/\partial z \leq 0) \end{cases}, \tag{3.5.114}$$

117

with the Brunt-Väisälä frequency N_l, the von Kármán constant k, $q_c = [(g/\overline{\theta_v})\overline{w'\theta'_v}L_T]^{1/3}$, and $\zeta = z/L_{MO}$ with the Monin-Obukhov length L_{MO}. w_L is a function given by

$$w_L(z) = \frac{1 - \tanh\left(\frac{z-(z_h+\Delta z)}{\Delta z/2}\right)}{2}, \tag{3.5.115}$$

with the boundary layer height z_h, and the transition layer depth into the free atmosphere Δz. z_h is calculated following the method of Olson *et al.* (2019) and Δz is assumed to be $0.3 z_h$. w_L is equal to 1 in the boundary layer ($z < z_h$), gradually decreases in the transition layer ($z_h \leq z < z_h + 2\Delta z$) and becomes 0 in the free atmosphere ($z \geq z_h + 2\Delta z$). It is introduced to switch mixing length formulation smoothly between the boundary layer and the free atmosphere.

L_T is defined by blending the length scales for the boundary layer ($L_{T(BL)}$) and the free atmosphere ($L_{T(FA)}$) as

$$L_T = w_L L_{T(BL)} + (1 - w_L)L_{T(FA)}, \tag{3.5.116}$$

$$L_{T(BL)} = 0.23\frac{\displaystyle\int_0^{z_h+\Delta z} qz\, dz}{\displaystyle\int_0^{z_h+\Delta z} q\, dz}. \tag{3.5.117}$$

$L_{T(FA)}$ is defined in sections where q^2 exceeds a threshold $q_{thr}^2 (= 10^{-4}\ \mathrm{m^2 s^{-2}})$ in the free atmosphere ($z > z_h$). If there are N sections, $L_{T(FA)}$ is evaluated as

$$L_{T(FA)}(z) = \begin{cases} L_{T(FA)}^1 & (z_{min}^1 \leq z \leq z_{max}^1) \\ L_{T(FA)}^2 & (z_{min}^2 \leq z \leq z_{max}^2) \\ \vdots & \vdots \\ L_{T(FA)}^N & (z_{min}^N \leq z \leq z_{max}^N) \\ 0 & (\text{elsewhere}) \end{cases}, \tag{3.5.118}$$

$$L_{T(FA)}^n = 0.23\frac{\displaystyle\int_{z_{min}^n}^{z_{max}^n} q(z - z_{min}^n)\, dz}{\displaystyle\int_{z_{min}^n}^{z_{max}^n} q\, dz} \quad (n = 1, 2, \cdots, N), \tag{3.5.119}$$

where z_{min}^n and z_{max}^n are the lower and upper boundary of the nth section.

3.5.7.5 Nondimensional Diffusion Coefficients

$S_{M2.5}$ and $S_{H2.5}$ are determined using the gradient Richardson number, TKE and the empirical constants appearing in closure assumptions. S'_M and S'_H are correction terms induced by enhancement from the level 2.5 model (in which only TKE is treated as a prognostic variable) to the level 3 model. The correction terms depend on the turbulent prognostic variables (q^2, $\overline{\theta_l'^2}$, $\overline{q_w'^2}$ and $\overline{\theta_l'q_w'}$). Following Nakanishi and Niino (2009), S_q, S_{θ_l}, $S_{\theta q}$ and S_{q_w} are assumed to be proportional to $S_{M2.5}$ as $S_q = 3S_{M2.5}$ and $S_{\theta_l} = S_{\theta q} = S_{q_w} = S_{M2.5}$. For technical details, refer to Nakanishi (2001) and Nakanishi and Niino (2004, 2006, 2009).

3.5.8 Surface Fluxes

The main procedures relating to surface processes involve the evaluation of surface fluxes. The surface scheme in the MSM employs a tiled approach in which different subgrid surface types are represented for land and sea. Turbulent fluxes are calculated for all tiles based on properties such as albedo and surface temperature, and are averaged over tiles with land fractions.

3.5.8.1 Basic Equations

Within the surface layer, it is assumed that turbulent fluxes are constant with height and equivalent to surface values. These can be expressed in terms of differences between quantities in the lowest layer of the atmosphere (u_1, v_1, θ_{v1}, and q_{v1}) and the surface (θ_{vs} and q_{vs}) as

$$\overline{u'w'} = -C_m U_a u_1 , \tag{3.5.120}$$

$$\overline{v'w'} = -C_m U_a v_1 , \tag{3.5.121}$$

$$\overline{w'\theta_v'} = -C_h U_a (\theta_{v1} - \theta_{vs}) , \tag{3.5.122}$$

$$\overline{w'q_v'} = -C_q U_a (q_{v1} - q_{vs}) , \tag{3.5.123}$$

where u and v are horizontal wind velocity components, θ_v virtual potential temperature, q_v specific humidity, and U_a wind speed near the surface. Following Kitamura and Ito (2016), U_a is expressed using turbulent kinetic energy, $E\ (= q^2/2)$, as

$$U_a = \sqrt{u_1^2 + v_1^2 + 2CE}, \tag{3.5.124}$$

where $C = 2/3$. q^2 is offered by the boundary layer scheme (see Subsection 3.5.7). q_{vs} is represented as a saturated specific humidity (q_{sat}) at the surface temperature (T_s):

$$q_{vs} = q_{sat}(T_s). \tag{3.5.125}$$

Over the sea surface, q_{vs} is reduced due to salinity by the factor of 0.98 (Zeng *et al.* 1998).

3.5.8.2 Transfer Coefficients for Momentum and Heat

The transfer coefficients are formulated as

$$
\begin{aligned}
C_m(z) &= \frac{k^2}{\left[\ln \dfrac{z}{z_{0m}} - \psi_m\left(\dfrac{z}{L_{MO}} \right) + \psi_m\left(\dfrac{z_{0m}}{L_{MO}} \right) \right]^2} \\
&\equiv \frac{k^2}{\Phi_m^2(z, L_{MO})} ,
\end{aligned} \tag{3.5.126}
$$

$$
\begin{aligned}
C_h(z) &= \frac{k^2}{\left[\ln \dfrac{z}{z_{0m}} - \psi_m\left(\dfrac{z}{L_{MO}} \right) + \psi_m\left(\dfrac{z_{0m}}{L_{MO}} \right) \right]\left[\ln \dfrac{z}{z_{0h}} - \psi_h\left(\dfrac{z}{L_{MO}} \right) + \psi_h\left(\dfrac{z_{0h}}{L_{MO}} \right) \right]} \\
&\equiv \frac{k^2}{\Phi_m(z, L_{MO})\Phi_h(z, L_{MO})} ,
\end{aligned} \tag{3.5.127}
$$

where z is the height of the lowest model layer, L_{MO} the Monin-Obukhov length, z_{0m} and z_{0h} the roughness length for momentum and heat, and $k = 0.4$ (von Kármán's constant). The integrated gradient functions for momentum, ψ_m, and heat, ψ_h, are given as functions of $\zeta = z/L_{MO}$ following Beljaars and Holtslag (1991) for unstable ($\zeta < 0$) and Gryanik *et al.* (2020) for stable ($\zeta \geq 0$):

$$
\psi_m(\zeta) = \begin{cases} -3\dfrac{a_m}{b_m}\left\{ (1 + b_m\zeta)^{1/3} - 1 \right\} & (\zeta \geq 0) \\[2em] \dfrac{\pi}{2} - 2\tan^{-1} x + \ln \dfrac{(1 + x)^2(1 + x^2)}{8} & (\zeta < 0) \end{cases} , \tag{3.5.128}
$$

$$
\psi_{\mathrm{h}}(\zeta) =
\begin{cases}
-\dfrac{a_h}{b_h} \ln(1 + b_h \zeta) & (\zeta \geq 0) \\[2ex]
2 \ln \dfrac{1 + x^2}{2} & (\zeta < 0)
\end{cases}
, \tag{3.5.129}
$$

with $a_m = 5$, $a_h = 5$, $b_m = 0.3$, $b_h = 0.4$ and $x = (1 - 16\zeta)^{1/4}$.

Here, u_1, v_1, θ_1 and q_{v1} are volume-averaged variables as ASUCA employs the finite volume method for the spatial descretization scheme. To make consistent with this, Φ_m and Φ_h should be averaged over the lowest model layer (Nishizawa and Kitamura 2018). The mean values of Φ_m and Φ_h are given by

$$
\overline{\Phi_m} = \Phi_m(\zeta_1) - \frac{1}{\zeta_1} \int_{\zeta_{0m}}^{\zeta_1} \phi_m(\zeta') d\zeta', \tag{3.5.130}
$$

$$
\overline{\Phi_h} = \Phi_h(\zeta_1) - \frac{1}{\zeta_1} \int_{\zeta_{0h}}^{\zeta_1} \phi_h(\zeta') d\zeta', \tag{3.5.131}
$$

where $\overline{\Phi_m}$ and $\overline{\Phi_h}$ are the mean values of Φ_m and Φ_h, $\zeta_1 = z_1/L_{\mathrm{MO}}$, $\zeta_{0m} = z_{0m}/L_{\mathrm{MO}}$, $\zeta_{0h} = z_{0h}/L_{\mathrm{MO}}$, $\phi_m = 1 - \zeta(\partial \psi_m/\partial \zeta)$, $\phi_h = 1 - \zeta(\partial \psi_h/\partial \zeta)$ and z_1 is the depth of lowest model layer.

The Monin-Obukhov length is determined from the following relation:

$$
Ri_{\mathrm{B}} = \frac{z}{L_{\mathrm{MO}}} \frac{\overline{\Phi_h}(z, L_{\mathrm{MO}})}{\overline{\Phi_m}^2(z, L_{\mathrm{MO}})}, \tag{3.5.132}
$$

which can be solved by using an iterative approach such as the Newton's method. Ri_{B} is the Bulk Richardson Number defined by

$$
Ri_{\mathrm{B}} = \frac{gz}{\dfrac{1}{2}(\theta_{v1} + \theta_{vs})} \frac{(\theta_{v1} - \theta_{vs})}{U_{\mathrm{a}}^2}. \tag{3.5.133}
$$

3.5.8.3 Transfer Coefficients for Moisture

C_{q} over sea areas is represented with the same formula as for C_{h}, except with the roughness length for moisture (z_{0q}). For land, evaporation from soil, vegetation and water intercepted by the surface are modeled. C_{q} over land is represented as

$$
C_{\mathrm{q}} = \left\{ f_{\mathrm{intc}} + (1 - f_{\mathrm{intc}}) \left[f_{\mathrm{veg}} (\psi_{\mathrm{stm}} + \psi_{\mathrm{can}}) + f_{\mathrm{soil}} \beta_{\mathrm{s}} \right] \right\} C_{\mathrm{h}} \tag{3.5.134}
$$

where f_{intc} is a fraction of the interception reservoir, f_{veg} is a fraction of vegetation, f_{soil} is a fraction of bare soil, ψ_{stm} and ψ_{can} are aerodynamic resistance factors, and β_{s} is evaporation efficiency from bare soil. f_{veg} is calculated using the 1km MODIS-based Maximum Green Vegetation Fraction (Broxton *et al.* 2014b). f_{soil} is given by

$$
f_{\mathrm{soil}} = 1 - f_{\mathrm{veg}} - f_{\mathrm{urban}}, \tag{3.5.135}
$$

where f_{urban} is a fraction of the urbanized area, and f_{urban} is obtained by combining the fractions of buildings and roads derived from the National Land Numerical Information dataset provided by Japan's Ministry of Land, Infrastructure, Transport and Tourism. Parameterization for the interception reservoir is as described in Subsection 3.5.9.

ψ_{stm}, a factor for vegetation transpiration, is given by

$$
\psi_{\mathrm{stm}} = \frac{1}{r_{\mathrm{s}}} \left(C_{\mathrm{h}} U_{\mathrm{a}} + \frac{1}{r_{\mathrm{s}}} \right)^{-1}, \tag{3.5.136}
$$

where r_s is stomatal resistance. r_s is a function of the Leaf Area Index (LAI), downward shortwave radiation, root zone soil water, atmospheric water vapor deficit and air temperature. Following Noilhan and Planton (1989), r_s is given by

$$r_s = \frac{r_{s,min}}{LAI} F_1 F_2^{-1} F_3^{-1} F_4^{-1} \tag{3.5.137}$$

with $r_{s,min}$ = 250 s m^{-1}. LAI is prescribed from monthly climatology based on the MODIS LAI product (Myneni 2015). F_1 parameterizes the influences of photosynthetically active radiation:

$$F_1 = (1 + f) \left(f + \frac{r_{s,min}}{r_{s,max}} \right)^{-1}, \quad f = \frac{0.55 S_\downarrow}{S_0} \left(\frac{2}{LAI} \right), \tag{3.5.138}$$

where $S_\downarrow$ is downward short-wave radiation at the surface, $r_{s,max}$ = 1200 s m^{-1} and S_0 = 30 W m^{-2}. F_2 describes the availability of soil water in the root zone for transpiration:

$$F_2 = \frac{w_2 - w_{wp}}{w_{fc} - w_{wp}} \quad (0 \le F_2 \le 1). \tag{3.5.139}$$

Here, w_2, w_{fc} and w_{wp} are volumetric soil water content in the root zone, at field capacity and at the wilting point, respectively. w_{fc} and w_{wp} are estimated using the fraction of clay (Subsection 3.5.9). F_3 (the effect of the vapor pressure deficit in air) and F_4 (air temperature dependence) are

$$\begin{aligned} F_3 &= 1 - 0.025 \{ e_{sat}(T_1) - e_1 \} \quad (0 \le F_3 \le 1) \\ F_4 &= 1 - 0.0016(298 - T_1)^2 \quad (0 \le F_4 \le 1) \end{aligned}, \tag{3.5.140}$$

where T_1 and e_1 are temperature and vapor pressure at the lowest model levels and $e_{sat}(T_1)$ is saturated vapor pressure at T_1.

ψ_{can} is a factor for turbulent exchange between the vegetation canopy and the underlying soil, given by

$$\psi_{can} = f_{can} \left(\frac{\beta_s g_{can}}{C_h U_a + \beta_s g_{can}} \right), \tag{3.5.141}$$

where g_{can} is in-canopy conductance and f_{can} is a canopy gap fraction. Following Essery *et al.* (2003), g_{can} is given by

$$g_{can} = \frac{C_m^{1/2} U_a}{43}, \tag{3.5.142}$$

f_{can} is a function of LAI following Zeng and Wang (2007):

$$f_{can} = 1 - V, \tag{3.5.143}$$

$$V = \frac{1 - \exp\{-k_{can} \min\langle LAI, LAI_{cr}\rangle\}}{1 - \exp\{-k_{can} LAI_{cr}\}}, \tag{3.5.144}$$

with k_{can} = 1.5 and LAI_{cr} = 2.

β_s is formulated following Lee and Pielke (1992):

$$\beta_s = \begin{cases} \frac{1}{4} \left[1 - \cos\left(\pi \frac{w_g}{w_{fc}}\right) \right]^2 & w_g < w_{fc} \\ 1 & w_g \ge w_{fc} \end{cases}. \tag{3.5.145}$$

w_g is surface volumetric soil water content (Subsection 3.5.9). If the gridbox is covered with snow, β_s is set as 1.

3.5.8.4 Roughness Length

Momentum roughness length (z_{0m}) for land depends on land use at each grid point. Thermal roughness length (z_{0h}) for land is calculated using the relational expression $\ln(z_{0m}/z_{0h}) = kB^{-1}$ (e.g., Garratt and Francey 1978). For urban surfaces, kB^{-1} is set as 6 following Kanda *et al.* (2005), while $kB^{-1} = 2$ is applied for other land use types. Moisture roughness length (z_{0q}) for land is assumed to be the same as z_{0h}.

Roughness lengths for sea areas are calculated using friction velocity u_* following Beljaars (1995):

$$z_{0m} = a_m \frac{\nu}{u_*} + a_{Ch} \frac{u_*^2}{g} , \tag{3.5.146}$$

$$z_{0h} = a_h \frac{\nu}{u_*} , \tag{3.5.147}$$

$$z_{0q} = a_q \frac{\nu}{u_*} , \tag{3.5.148}$$

where $a_m = 0.11$, $a_{Ch} = 0.018$, $a_h = 0.40$ and $a_q = 0.62$, and ν is kinematic viscosity ($= 1.5 \times 10^{-5}$ m^2 s^{-1}). u_* is defined by

$$u_* = \left(\overline{u'w'}^2 + \overline{v'w'}^2 \right)^{\frac{1}{4}} . \tag{3.5.149}$$

3.5.8.5 Screen Level Diagnostics

The screen level physical quantities such as temperature and dew point at 1.5 m height and wind at 10 m height are diagnosed by interpolation between the lowest model level and surface assuming the same gradient functions as in the scheme of surface process. Wind velocity at z_{10m} (10 m height), u_{10m}, and virtual potential temperature at $z_{1.5m}$ (1.5 m height), $\theta_{v1.5m}$ are diagnosed as

$$u_{10m} = \sqrt{\frac{C_m(z)}{C_m(z_{10m})}} u_1 , \tag{3.5.150}$$

$$\theta_{v1.5m} = \theta_{vs} + \frac{C_h(z)}{C_h(z_{1.5m})} \sqrt{\frac{C_m(z_{1.5m})}{C_m(z)}} (\theta_{v1} - \theta_{vs}) . \tag{3.5.151}$$

3.5.9 Ground Temperature and Soil Moisture

3.5.9.1 Ground Surface Temperature

Ground surface temperature, which is used in evaluating surface fluxes, is predicted by solving a surface energy balance equation given by

$$c_s \frac{\partial T_s}{\partial t} = (1 - \alpha) S_{w\downarrow} + L_{w\downarrow} - \sigma T_s^4 - H - LE - G_s , \tag{3.5.152}$$

where $S_{w\downarrow}$ and $L_{w\downarrow}$ denote the fluxes of shortwave and longwave radiation towards the surface, σ is the Stefan-Boltzmann constant, α is the surface albedo, and G_s is heat flux towards the ground. H and LE represent fluxes of sensible heat and latent heat from the surface:

$$H = -C_p \rho \, \overline{w'\theta_v'} , \tag{3.5.153}$$

$$LE = -L\rho \, \overline{w'q_v'} , \tag{3.5.154}$$

where C_p is the specific heat of dry air at a constant pressure, L is the latent heat of vaporization, and ρ is the density of air near the surface.

Ground temperature (T_g), which is used in evaluating G_s, is predicted using a multi-layer model. The basic formula adopted is the heat conduction equation:

$$c_g \frac{\partial T_g}{\partial t} = -\frac{\partial G}{\partial z}, \quad G = -\lambda \frac{\partial T_g}{\partial z} , \tag{3.5.155}$$

where G is ground heat flux, c_{g} is heat capacity and λ is thermal conductivity. The soil column is discretized into eight layers to solve the above equations, numerically. The soil temperature for the lowest layer is fixed to a climatological value for forecasts. To obtain climatological data for ground temperature, monthly mean temperatures at standard pressure levels were first calculated from objective analysis conducted in 1985 and 1986. Next, these data were interpolated vertically to the model ground surface. Then, only the annual mean and the first harmonic component of annual change in surface temperature were extracted to obtain the climatological underground temperature at the k-th ground layer with the following equation:

$$T_{\mathrm{g}} = \hat{T} + A \exp\left(-\frac{z}{d}\right) \cos\left\{\frac{2\pi}{365}(D - P) - \frac{z}{d}\right\} , \qquad (3.5.156)$$

where $\hat{T}$ is the mean ground surface temperature, A and P are the amplitude and the phase of the annual component of surface temperature, respectively, z_{k} is the depth of the k-th ground layer, $d(= 2.65 \text{ m})$ is the e-folding depth and D is the number of days since the beginning of the year.

Sea surface temperature is also spatially interpolated from the results of SST analysis (Section 5.2). The value is given as T_{s}, and is predicted using an ocean mixed-layer model (Subsection 3.5.10) for the MSM.

3.5.9.2 Interception Reservoir

Rainfall and dew are intercepted by vegetation, urban surface and bare ground, with intercepted water evaporating at the potential rate. The prognostic equation for intercepted water content W is

$$\frac{dW}{dt} = P_{\mathrm{r}} - E_{intc} - R_{\mathrm{r}}, \qquad (3.5.157)$$

where P_{r} is the precipitation rate, and E_{intc} and R_{r} are evaporation and runoff rates from intercepted water. E_{intc} is given by

$$E_{\mathrm{intc}} = f_{\mathrm{intc}} C_{\mathrm{h}} U_{\mathrm{a}} (q_{\mathrm{vs}} - q_{\mathrm{v1}}). \qquad (3.5.158)$$

The interception reservoir fraction f_{intc} is defined as

$$f_{\mathrm{intc}} = \left(\frac{W}{W_{\mathrm{m}}}\right)^{2/3} , \qquad (3.5.159)$$

where W_{m} is the maximum value for intercepted water. W_{m} is defined from LAI, f_{urban} and f_{soil} as:

$$W_{\mathrm{m}} = W_{\mathrm{m,veg}} \mathrm{LAI} f_{\mathrm{veg}} + W_{\mathrm{m,urban}} f_{\mathrm{urban}} + W_{\mathrm{m,soil}} f_{\mathrm{soil}}. \qquad (3.5.160)$$

$W_{\mathrm{m,veg}}$, $W_{\mathrm{m,urban}}$ and $W_{\mathrm{m,soil}}$ are set as 0.2 kg m^{-3}.

R_{r} is simply defined as the excess of intercepted water, given by

$$R_{\mathrm{r}} = \frac{1}{\Delta t} \max \langle W + (P_{\mathrm{r}} - E_{\mathrm{intc}})\Delta t - W_{\mathrm{m}} , 0\rangle \qquad (3.5.161)$$

where Δt is the model timestep.

3.5.9.3 Soil Moisture

Soil moisture is predicted using the force-restore method based on Noilhan and Planton (1989):

$$\frac{\partial w_{\mathrm{g}}}{\partial t} = \frac{C_1}{\rho_{\mathrm{w}} d_1}(R_{\mathrm{r}} - E_{\mathrm{bs}}) - \frac{C_2}{\tau}(w_{\mathrm{g}} - w_{\mathrm{geq}}) , \qquad (3.5.162)$$

$$\frac{\partial w_2}{\partial t} = \frac{1}{\rho_{\mathrm{w}} d_2}(R_{\mathrm{r}} - E_{\mathrm{bs}} - E_{\mathrm{tr}}) , \qquad (3.5.163)$$

where w_2 is the mean volumetric water content in the root zone, τ a time constant (86400 s), E_{bs} the evaporation rate from bare soil, E_{tr} the transpiration rate, ρ_w the density of liquid water, $d_1 = 0.1$ m, $d_2 = 0.5$ m, and w_{geq} the surface volumetric water content on which gravity balances the capillarity forces. Evaporations from soil (E_{bs} and E_{tr}) are given by

$$E_{bs} = \rho(1 - f_{intc})(f_{soil}\beta_s + f_{veg}\psi_{can})C_h U_a(q_{vs} - q_{v1}) \tag{3.5.164}$$

$$E_{tr} = \rho(1 - f_{intc})f_{veg}\psi_{stm}C_h U_a(q_{vs} - q_{v1}). \tag{3.5.165}$$

C_1, C_2 and w_{geq} are defined as

$$C_1 = \begin{cases} C_{1,sat}\left(\dfrac{w_g}{w_{sat}}\right)^{-b/2-1} & w_g \geq w_{wp} \\[3mm] C_{1,max}\exp\left[-\dfrac{(w_g - w_{max})^2}{2\sigma_g^2}\right] & w_g < w_{wp} \end{cases}, \tag{3.5.166}$$

$$C_2 = C_{2,ref}\left(\frac{w_2}{w_{sat} - w_2 + 0.01}\right), \tag{3.5.167}$$

$$w_{geq} = w_2 - aw_{sat}\left(\frac{w_2}{w_{sat}}\right)^p\left[1 - \left(\frac{w_2}{w_{sat}}\right)^{8p}\right]. \tag{3.5.168}$$

When soil is very dry, C_1 implicitly represents the vapor phase transfers within soil (Braud *et al.* 1993). Following Noilhan and Mahfouf (1996), $C_{1,max}$, w_{max}, and σ_g are expressed as

$$C_{1,max} = (1.19w_{wp} - 5.09) \times 10^{-2}T_s + 1.464w_{wp} + 17.86, \tag{3.5.169}$$

$$w_{max} = \eta w_{wp}, \tag{3.5.170}$$

$$\eta = (-1.815 \times 10^{-2}T_s + 6.41)w_{wp} + (6.5 \times 10^{-3}T_s - 1.4), \tag{3.5.171}$$

$$\sigma_g^2 = -\frac{w_{max}^2}{2\ln\dfrac{0.01}{C_{1,max}}}. \tag{3.5.172}$$

Hydraulic parameters w_{sat}, w_{wp}, w_{fc}, b, $C_{1,sat}$, $C_{2,ref}$, a, p are related to soil texture. Using empirical equations based on Noilhan and Lacarrére (1995), these parameters are estimated as follows:

$$w_{sat} = (-1.08f_{sand} + 494.305) \times 10^{-3}, \tag{3.5.173}$$

$$w_{wp} = 37.1342 \times 10^{-3}(f_{clay})^{1/2}, \tag{3.5.174}$$

$$w_{fc} = 89.0467 \times 10^{-3}(f_{clay})^{0.3496}, \tag{3.5.175}$$

$$b = 0.137f_{clay} + 3.501, \tag{3.5.176}$$

$$C_{1,sat} = (5.58f_{clay} + 84.88) \times 10^{-2}, \tag{3.5.177}$$

$$C_{2,ref} = 13.815(f_{clay})^{-0.954}, \tag{3.5.178}$$

$$a = 732.42 \times 10^{-3}(f_{clay})^{-0.539}, \tag{3.5.179}$$

$$p = 0.134f_{clay} + 3.4 \tag{3.5.180}$$

f_{sand} and f_{clay}, which are sand and clay fractions in the soil, are obtained from HWSD (Harmonized World Soil Database) dataset (FAO *et al.* 2012).

3.5.10 Ocean Mixed Layer

The ocean mixed layer (OML) scheme treats temporal variations in water temperature and salinity, especially during periods of typhoon passage, to provide temporally changing lower boundary conditions of flux over the

ocean. In such conditions, near-surface wind drives vertical mixing and upwelling of sea water, resulting in sea surface cooling. Formulation of one-dimensional prognostic equations for water temperature T_{ocn}, salinity S, and ocean current V_{ocn} in the ocean is based on Price *et al.* (1986):

$$\frac{\partial T_{ocn}}{\partial t} = -\frac{1}{\rho_0 C}\frac{\partial F}{\partial z} + D, \tag{3.5.181}$$

$$\frac{\partial S}{\partial t} = -\frac{\partial E}{\partial z} + D, \tag{3.5.182}$$

$$\frac{\partial V_{ocn}}{\partial t} = -f \times V_{ocn} - \frac{1}{\rho_0}\frac{\partial G}{\partial z}, \tag{3.5.183}$$

where F, E, and G are air-sea heat fluxes, as given from the surface scheme (Subsection 3.5.8) and radiation scheme (Subsection 3.5.6) and freshwater fluxes (calculated from evaporation and precipitation rates), and G is wind stress. D is a Rayleigh damping term, ρ_0 is the reference density of water, C is the heat capacity of water, and f is the Coriolis parameter.

The OML scheme considers three vertical mixing processes based on:

$$\frac{\partial \rho}{\partial z} \le 0 \tag{3.5.184}$$

for static stability,

$$R_b = \frac{g\Delta\rho h}{\rho_0(\Delta V_{ocn})^2} \le 0.30 \tag{3.5.185}$$

for mixed layer shear flow stability, and

$$R_g = \frac{g\partial\rho/\partial z}{\rho_0(\partial V_{ocn}/\partial z)^2} \le 0.25 \tag{3.5.186}$$

for stratified shear flow stability. g is the acceleration of gravity, h is the mixed layer depth, and $\Delta()$ takes the difference between the mixed layer and the level just beneath.

First, heat fluxes except short-wave radiation and freshwater fluxes are given to the surface grid, a density profile is calculated. Short-wave radiation is absorbed within the water column with a double exponential depth dependence. When static instability (3.5.184) matches, the mixing occurs from the surface downward and the mixed layer is homogenized until static stability is achieved. Second, wind stress drives mixed-layer motion, and the mixed-layer Richardson number R_b is calculated. The mixed layer entrains successively deeper levels as long as (3.5.185) is satisfied. Lastly, the gradient Richardson number R_g is calculated for each grid, and adjacent cells are mixed as long as (3.5.186) is satisfied.

The OML scheme is applied only at sea grids. To avoid drifts of water temperature and salinity, Rayleigh damping is applied as follows:

$$D = -L(b, d)(\phi - \phi_{ini}), \tag{3.5.187}$$

$$L(b, d) = min\left[max\left\{\frac{L_b(b)}{\tau}, \frac{L_d(d)}{\tau}\right\}, \frac{1}{dt}\right], \tag{3.5.188}$$

$$L_b(b) = \left\{\frac{b_{th}}{min(b_{th}, b)}\right\}^2, \tag{3.5.189}$$

$$L_d(d) = \left\{\frac{d_{th}}{min(d_{th}, d)}\right\}^2, \tag{3.5.190}$$

where L is the location-based function, ϕ_{ini} is the value of the initial condition, $\tau = 86,400$ s, $b_{th} = 50$ m, $d_{th} = 400$ km, b is the ocean floor, d is the distance from land grids and dt is the integration time step. The e-folding time decreases when the ocean bottom is shallower than b_{th} and the distance from land grids is

less than d_{th} to vary water temperature and salinity smoothly between grids where the OML scheme turns on and off. The vertical grid spacing is 5 m, with the deepest bottom at 100 m to save computational time and memory. Sea surface temperature (SST) is given from SST analysis (Section 5.2). The initial conditions of ocean variables are spatially and temporally interpolated from the monthly climatology of the World Ocean Atlas 2018 (WOA18, Locarnini *et al.* 2018; Zweng *et al.* 2018). To fill the discontinuity between SST and water temperature, the SST anomaly from the surface water temperature of WOA18 is added to the water temperature from surface to bottom. Ocean currents are set to zero at initial condition.

3.5.11 Parallelization

The Open Multi Processing (OpenMP) interface is employed for shared memory parallelization in the model, and the Message Passing Interface (MPI) is used for distributed memory parallelization. The model domain is split into horizontally two-dimensional sub-domains, and each decomposed sub-domain is assigned to one of the MPI processes (Aranami and Ishida 2004).

The OpenMP interface is used for parallelization inside the sub-domains. OpenMP threads are applied to loops for the y direction, and some horizontal loops (i.e., for the x and y directions) are fused to increase the loop length such that the load imbalance between threads is minimized. The z direction is used as the innermost loop at which vectorization is applied. Thus, kij-ordering is adopted for nested loops.

The sub-domains have halo regions that are exchanged with immediately adjacent MPI processes. As MPI communication and file I/O are time-consuming operations with the current supercomputer architecture, two types of overlapping are used in the model to significantly improve computational efficiency. One is overlapping of halo exchanges with the computation (Cats *et al.* 2008) to minimize the overhead of communication between MPI processes. The OpenMP interface is also used for this operation; while one thread is communicating with another MPI process, the other threads continue independent computation. The other technique involves an I/O server approach (Selwood 2012) to overlap file I/O with computation. In this method, some MPI processes are dedicated to file I/O. While computation continues, dedicated I/O processes read data from files and send them to the relevant computational processes. When output is required, the processes save the data in a dedicated buffer to invoke send operation and immediately continue computation. I/O processes receive the data and output the data to the disk.

The domain decomposition and I/O server configuration involve 88 nodes and 1056 MPI processes (including 20 I/O processes), with 8 threads/MPI for 78-hour forecasts, and 51 nodes and 816 MPI processes (including 16 I/O processes), with 6 threads/MPI for 39-hour forecasts used on Cray XC50.

3.5.12 Forecast Performance

Forecast verification is an essential process for monitoring the quality of NWP products and improving the model itself. This subsection outlines the performance of MSM precipitation forecasts with evaluation based on comparison with actually observed values.

Figures 3.5.4 and 3.5.5 show time-series representations of threat and bias scores for three-hour cumulative precipitation forecasts produced by the MSM with a 10-mm threshold from January 2015 to December 2022. Verification is performed using Radar/Raingauge-Analyzed Precipitation data (referred to here as R/A; see Subsection 4.4.1) as reference observations. The verification grid size is 20 km, meaning that forecast and observed precipitation over land or sea within 40 km from the coast is averaged over 20 km meshes. Using all verification grids, contingency tables are created for each initial time by comparing forecasts and observations, and aggregated into monthly or annual tables.

These figures indicate that the threat score improved in 2017 in which the new-generation nonhydrostatic model ASUCA was introduced to the MSM (see Subsection 3.5.1). The bias score gradually approaches to unity over the previous eight years while the threat score remains at the same level since 2017. This steady progress is attributable to the ongoing development of the forecast model and its data assimilation system with more extensive use of observation data.
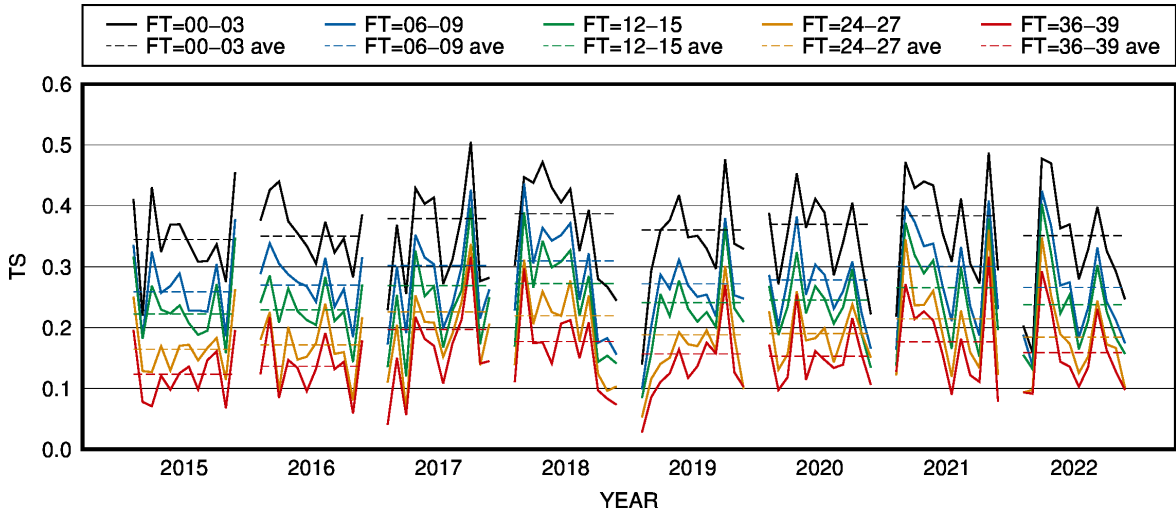
Figure 3.5.4: Monthly and annual threat scores of 3-hour cumulative precipitation at the 10 mm threshold, against the R/A within 20 km verification grids. The solid and dashed lines represent monthly and annual scores for each, FT represents the forecast range (hours). The verification period is from January 2015 to December 2022.
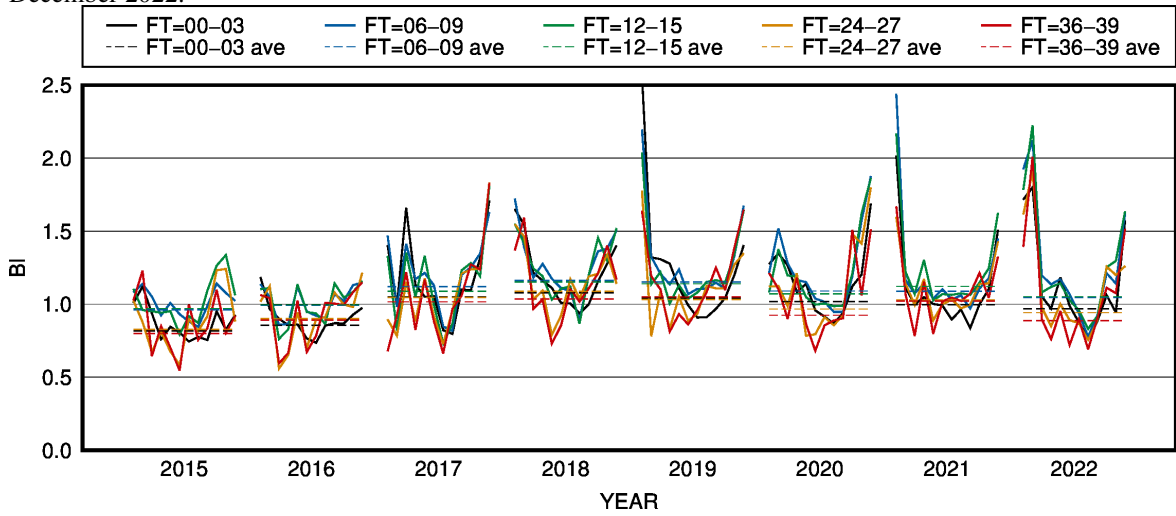

Figure 3.5.5: As per Figure 3.5.4, but for bias scores

127

3.6 Meso-scale Ensemble Prediction System

3.6.1 Introduction

This section describes the configuration of the regional model-based Mesoscale Ensemble Prediction System (MEPS), introduced in June 2019 based on Ono *et al.* (2021), primarily to provide uncertainty information for the MSM. Updates of initial and lateral boundary perturbations in September 2020 (Kakehata *et al.* 2021) and the introduction of a stochastic physics scheme in March 2023 (Kawada *et al.* 2023) are also outlined.

3.6.2 System Configuration

MEPS consists of 21 members, including 1 non-perturbed run. As the forecast model used in each ensemble member is identical to that of the MSM (5 km horizontal grid spacing, 96 vertical layers), non-perturbed control forecasting is identical to MSM forecasting with 39-hour forecasts at 0000, 0600, 1200 and 1800 UTC. Uncertainties in initial and lateral boundary conditions are considered, as described below, with initial perturbations (IPs) and lateral boundary perturbations (LBPs) derived from singular vectors (SVs). IPs comprise a linear combination of global SVs (GSVs) based on GSM and meso-scale SVs from the JMA-NHM(Saito *et al.* 2006), which has different spatial and temporal resolutions, and LBPs are supplied from linearly evolved GSVs. Model uncertainties are considered using the Stochastically Perturbed Parametrization Tendencies scheme (SPPT; Buizza *et al.* (1999a), Palmer *et al.* (2009)). Uncertainties in lower-boundary conditions are not considered in the current system (see Table 3.6.1 for MEPS specifications).

Table 3.6.1: MEPS specifications

System	
Title	Meso-scale Ensemble Prediction System
Implementation	27 June 2019 (Latest version: 28 March 2023)
Configuration	
Domain	Japan, Lambert projection, 817×661 grid points
Horizontal resolution (grid spacing)	5 km at 60 and 30°N (standard parallels)
Vertical resolution (model top)	96 stretched height hybrid levels (37.5 km)
Forecast length	39 hours (00, 06, 12, 18 UTC)
Members	1 unperturbed control forecast and 20 perturbed ensemble
Coupling to ocean / wave / sea ice models	–
Integration time step	100/3 seconds (3-stage Runge-Kutta method)
Initial conditions and perturbations	
Strategy	Singular vectors (SVs); linear combination of MSV40s, MSV80s and global SVs (GSVs)
Lateral boundary perturbations	
Strategy	Based on integration of GSV (a large-scale component of initial perturbation) using the tangent linear model
Model uncertainty perturbations	
Physics	Stochastic perturbation of physics tendency
Other model details	
	All ensemble members use exactly the same model as the MSM.

3.6.3 Initial Perturbations

3.6.3.1 Singular Vectors

The SV method computes perturbations with a large growth rate σ,

$$\sigma = \frac{\|\mathbf{M}x\|}{\|x\|} \tag{3.6.1}$$

where $x \in \mathbf{R}_N$ is an N-dimensional perturbation vector and $\mathbf{M}$ is the tangent linear model (TLM) operator. Using the positive-definite operator $\mathbf{C}$ and a Euclidean inner product $(\cdot, \cdot)$, the perturbation norm is given by

$$\|x\| = \sqrt{(\mathbf{T}x, \mathbf{CT}x)}. \tag{3.6.2}$$

$\mathbf{T}$ is a local projection operator (LPO) that constrains the perturbation growth locations. At the initial time, $\mathbf{T}$ is usually an identity matrix.

To numerically solve (3.6.1) with a large growth rate σ, the eigenvalue problem of the matrix

$$\mathbf{A} \equiv \mathbf{C}^{-\frac{1}{2}*}\mathbf{M}^*\mathbf{T}^*\mathbf{CTMC}^{-\frac{1}{2}}, \tag{3.6.3}$$

is solved using the numerical algorithm called Lanczos algorithm. In (3.6.3), $\mathbf{M}^*$ denotes the adjoint model (ADM). The TLM/ADM integration time is called the optimization time interval (OTI).

Total energy (TE; Ehrendorfer *et al.* 1999) is used as the norm in MEPS, described as

$$\|x\|^2 = \int_S \int_{Z_{\text{btm}}}^{Z_{\text{top}}} \frac{1}{2}\rho \left[u^2 + v^2 + w^2 + w_t \frac{C_p\theta^2}{T_r} + RT_r\left(\frac{p}{P_r}\right)^2 + w_q \frac{L^2}{C_pT_r}q^2 \right] dzdS \tag{3.6.4}$$

where ρ is density, u, v and w are zonal, meridional and vertical wind perturbations, respectively, θ, p and q are perturbations of potential temperature, pressure and the mixing ratio of water vapor, respectively, C_p is specific heat at a constant pressure, $T_r = 300$ K and $P_r = 1,000$ hPa are reference values of temperature and pressure, respectively, R is the gas constant, L is the latent-heat constant, and w_t and w_q are weight coefficients for θ and q, respectively. $\int_S$ and $\int_{Z_{\text{btm}}}^{Z_{\text{top}}}$ indicate integration extending over the horizontal target domain S and the vertical direction from Z_{btm} to Z_{top}, respectively.

3.6.3.2 Global SVs

GSM-based SVs are used as IPs and LBPs to represent large-scale uncertainties of synoptic flow in middle to upper troposphere, GSM-based SVs are used as IPs and LBPs. Global SVs (GSVs) are adopted in the global EPS (Subsection 3.3.3.2), while GSVs adopted in MEPS are calculated using a more suitable configuration for a regional EPS that targets the Japan area with a shorter OTI.

The horizontal resolution of each GSVs is TL63 (around 270 km in the mid-latitudes) with 40 vertical layers. The OTI is set as 45 hrs, which is longer than the forecast range of MEPS (39 hrs), because the operational limitation for the initial time of global analysis at the operational start time of MEPS is 6 hrs earlier than that of MEPS.

TE is also adopted as the norm for GSVs. However, in MEPS, the pressure term is not taken into account because its amplitude may be negligible in contrast to other TE terms. As moisture perturbations often cause excessive precipitation and unrealistic humidification results for land areas, the weight of the specific humidity term in TE is set as zero for GSV computations in MEPS ("Dry TE" in Table 3.6.2).

3.6.3.3 Mesoscale SVs

Mesoscale SVs (MSVs) are utilized for IPs in MEPS, with particular focus on the sensitivity of water vapor fields to severe weather. MSVs are based on a simplified version of JMA-NHM (Saito *et al.* 2006) and the TLM and ADM developed for JNoVA (Honda *et al.* 2005), along with the Lanczos algorithm.

Table 3.6.2: Configurations of MSV40, MSV80 and GSV

	MSV40	MSV80	GSV
Domain	Same as MSM (102 x 82)	Same as MSM (51 x 41)	Global
Resolution	40 km, L38	80 km, L38	TL63L40
OTI	6 hrs	15 hrs	45 hrs
norm	Moist TE	Moist TE	Dry TE
Horizontal target	125°–145° E, 25°–45° N	125°–145° E, 25°–45° N	120°–170° E, 25°–45° N
Vertical target	q: ~3 km, u, v, θ: ~5 km	q: ~3 km, u, v, θ: ~5 km	~9 km
No. of SVs	10	10	20
Use	IPs	IPs	IPs and LBPs

MSV40s computed in MEPS have a horizontal resolution of 40 km with 38 vertical layers and are designed to target meso-β- to meso-α-scale meteorological systems with a shorter OTI of 6 hrs. MSV80s with a horizontal resolution of 80 km, which can be expected to complement MSV40s in IP spatial distribution, are also employed. The OTI of each MSV80 is 15 hrs with targeting of meso-α-scale phenomena.

The TE norm is also adopted to evaluate MSV growth rates. In contrast to the norm used for GSVs, the moisture term here is explicitly considered for MSVs ("Moist TE" in Table 3.6.2). The weight of the potential temperature term w_t is 3.0, and that of the moisture term w_q is 0.6. Other terms are evaluated to an altitude of around 5 km, while vertical integration of the moisture term is limited to approximately 3 km because the desired MSVs for MEPS are related to water vapor fields in lower layers rather than to large-scale flows. Ten SVs are calculated for each MSV40 and MSV80 in the MSV target region around Japan (125–145° E and 25–45° N). Adaptive targeting is also used, with adaptive limitation of the MSV region depending on weather conditions. Here, grid points with 925 hPa vorticity values below a certain threshold are removed from the predetermined rectangular target region (Kakehata *et al.* 2021).

The specifications of these SVs are summarized in Table 3.6.2.

3.6.3.4 Linear Combination of SVs

IPs in MEPS comprise a linear combination of MSV40s, MSV80s and GSVs. Before blending, MSV80s and GSVs are interpolated to have the same resolution as MSV40s. The amplitude of each perturbation is then adjusted so that the maximum value of any one element is 5.13 m/s for wind components, 3.42 K for potential temperature and 5.13 g/kg for the mixing ratio of water vapor.

After these procedures, coefficients of the linear combination of all SVs are determined via variance minimum rotation (Yamaguchi *et al.* 2009). Ten sets of IPs are randomly chosen from 40 candidates calculated via variance minimum rotation because only this number is required for the 21 ensemble runs (including one non-perturbed run).

3.6.4 Lateral Boundary Perturbation

For a regional EPS, it is essential to consider uncertainties in lateral boundaries as well as in initial fields. It is preferable for LBPs to be consistent with the time evolution of IPs (Caron 2013). In consideration of the requirements for LBPs in a regional EPS, the linearly evolved GSVs used for IPs are adopted. Here, evolved GSVs are linearly combined using the variance minimum rotation coefficients used for IPs. This configuration enables provision of consistent and seamless perturbations during the forecast period even when their spatial scales are larger than those of the model domain.

The LBP amplitude is adjusted to reflect the uncertainty of lateral boundary conditions. In MEPS, amplitude is determined such that the average of temperature perturbations at around 500 hPa at the initial time of

the MEPS is equal to the climatological root mean square error (RMSE) of lateral boundary values against the MSM initial fields.

3.6.5 Perturbed Physics

The SPPT scheme (Buizza *et al.* (1999a), Palmer *et al.* (2009)) is used to represent model uncertainties in physical processes. The perturbed tendency of the physical process is

$$X_p = (1 + r_X)X_c, \tag{3.6.5}$$

where r_X is a Gaussian random number correlated in space-time, and X_c is the physical process tendency. The random number amplitude was set as 0.5, the correlation time as 6 hours, and the correlation length as 500 km. For computational stability, only convection and radiation scheme tendencies were perturbed.

3.7 Local Forecast Model (JMA-LFM2303)

3.7.1 Introduction

The Local Forecast Model (LFM) was launched in August 2012, along with the Local Analysis (LA) described in Section 2.7, leveraging a supercomputer upgrade implemented in June 2012. The LFM provides weather information for aviation and disaster prevention, running forecasts at an even higher resolution than the 5-km Meso-Scale Model (MSM, Section 3.5). It has 2-km horizontal grid spacing and 76 vertical layers up to a height of 21,801 m above sea level, and is designed to produce forecasts featuring greater detail with emphasis on predicting localized and short-lived extreme events.

The model focuses on providing very-short-range forecasts such as those covering the period 10 hours ahead, and allows quick and frequent updating of forecasts using initial conditions with the latest observations assimilated by LA. The operation of the LFM was started with 8 runs per day on a domain covering the eastern part of Japan (1,100 km × 1,600 km), and operation was extended in May 2013 to 24 runs per day on a domain covering Japan and its surrounding areas (3,160 km × 2,600 km).

A new-generation non-hydrostatic model known as ASUCA (Ishida *et al.* 2009, 2010, 2022; Hara *et al.* 2012) replaced the previous JMA-NHM (Saito *et al.* 2006, 2007) for LFM forecasting in January 2015 (Aranami *et al.* 2015), ahead of its implementation in the MSM in February 2017 (Subsection 3.5.1). Selected later upgrades of the ASUCA dynamical core and physics library applied to the MSM were also incorporated into the LFM in January 2017. The forecast range was extended from 9 to 10 hours in March 2019. The number of vertical layers was increased from 58 to 76 in March 2021, and the land surface model was updated to the one introduced for the MSM in March 2022. Physical process improvement included the implementation of cloud microphysics used in the MSM, and incorporation of turbulent orography form drag in March 2023, with updates of trace gas concentration and the topography data set.

3.7.2 General Configurations

The LFM provides 10-hour forecasts every hour on the hour. The forecast domain covers Japan and its surrounding areas, and has 2-km horizontal grid spacing.

The LFM employs a model identical to the MSM with similar configuration (see Section 3.5), incorporating the changes described below (see Table 3.1.3).

- Boundary conditions are obtained from MSM forecasts.

- The model is operated with a 12-second timestep.

- The main part of convection vertical transport is expected to be resolved with grid mean vertical velocity at a horizontal grid spacing of 2 km. However, this does not necessarily mean that all phenomena associated with convection can be resolved. In particular, phenomena on unresolved scales (such as small-scale

convergences and topography variances) can induce the forced lifting needed to initiate convection. Accordingly, parameterization to represent convective initiation is used in the LFM (Hara 2015), thereby mitigating delays in the onset of convection.

- The LFM incorporates the advanced version of the cloud microphysics scheme used in the MSM (Ikuta *et al.* 2021), with modifications for 2 km resolution.

- As described in Subsection 3.5.6, the cloud fraction used in the radiation process is diagnosed in consideration of fluctuations of temperature and water content from their grid mean values over each of the grids. As the fluctuations are expected to be smaller in higher resolution models, the width of the probability density function depicting the characteristics of the fluctuation was made smaller than that used in the MSM.

- Trace gas (CO_2, N_2O, CH_4) concentration in the radiation process was updated with WMO (2021).

- The ocean mixed layer model introduced to the MSM in March 2022 (Subsection 3.5.10) is not used; sea surface temperature is fixed at an initial value.

- The GTOPO30 Subsection 3.5.1 data set was replaced with MERIT DEM (Yamazaki *et al.* 2017), a very accurate high-resolution topography data set.

- A turbulent orographic form drag scheme was introduced following Beljaars *et al.* (2004b). Standard deviations for topography were obtained from MERIT DEM.

- The domain decomposition and I/O server configuration in parallelization involve 138-nodes, 1656 MPI processes and 8 threads/MPI on Cray XC50. The domain is divided into 45 parts in the x-direction and 36 in the y-direction, and there are 36 I/O servers.

3.7.3 Forecast Performance

LFM forecast performance is evaluated in the same way as for MSM forecasts (Subsection 3.5.12). Figures 3.7.1 and 3.7.2 show time-series representations of threat and bias scores for LFM one-hour cumulative precipitation forecasts at a 10-mm threshold. It can be seen that the LFM tends to underestimate precipitation in the one-hour forecast range in summer and overestimate with lead times from two hours onward, with a spin-up period during the initial forecast stages.

To verify the skill of LFM convective precipitation forecasts, the Fractions Skill Score (FSS ; Subsection A.2.12) of one-hour cumulative precipitation from the LFM is compared with that from the MSM. Figure 3.7.3 shows FSS differences between the two models averaged over all initial times for July 2022 with a verification grid size of 5 km. The LFM is inferior for the thresholds less than 10 mm particularly in the one-hour forecast range, due to the spin-up effect from the initial field as seen in Figure 3.7.2. For spatial scales over 80 km, the LFM FSS is better than that of the MSM with thresholds over 15 mm. The forecast skill superiority of the LFM is remarkable for the latter forecast range. Figure 3.7.4 shows a Hovmöller diagram of FSS differences between the two models for a spatial scale of 80 km and a forecast range of nine hours averaged over all initial times for each month. For thresholds less than 5 mm, the difference is quite small for all seasons. The LFM FSS improves for thresholds over 10 mm, for summer after 2020. Thus, the LFM exhibits superior forecast skill for heavy rain events.
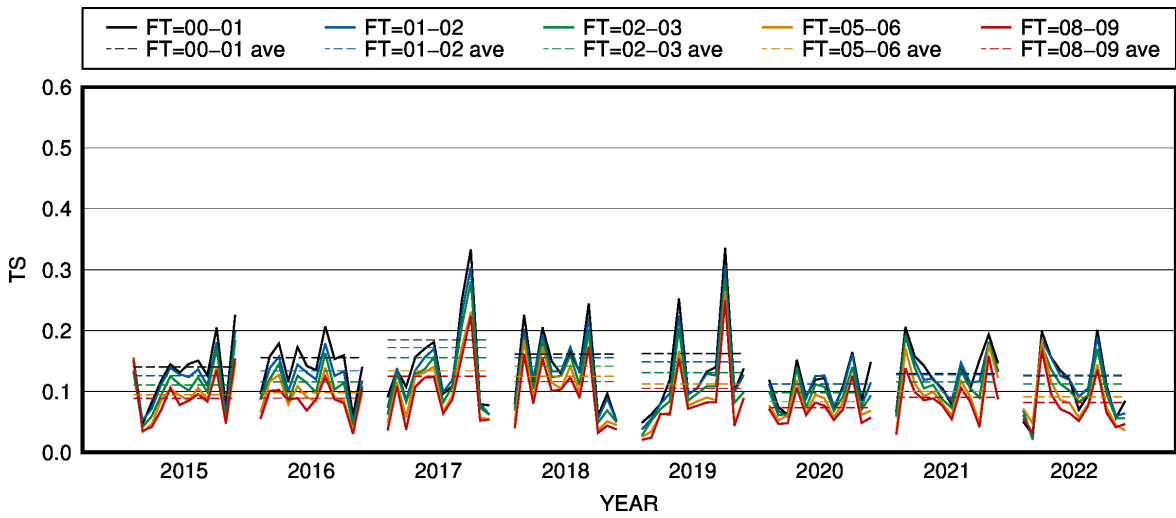
Figure 3.7.1: Monthly and annual threat scores for one-hour cumulative precipitation at the 10 mm threshold against the R/A within 10 km verification grids. The solid and dashed lines represent monthly and annual scores for each, and FT represents the forecast range (hours). The verification period is from January 2015 to December 2022.
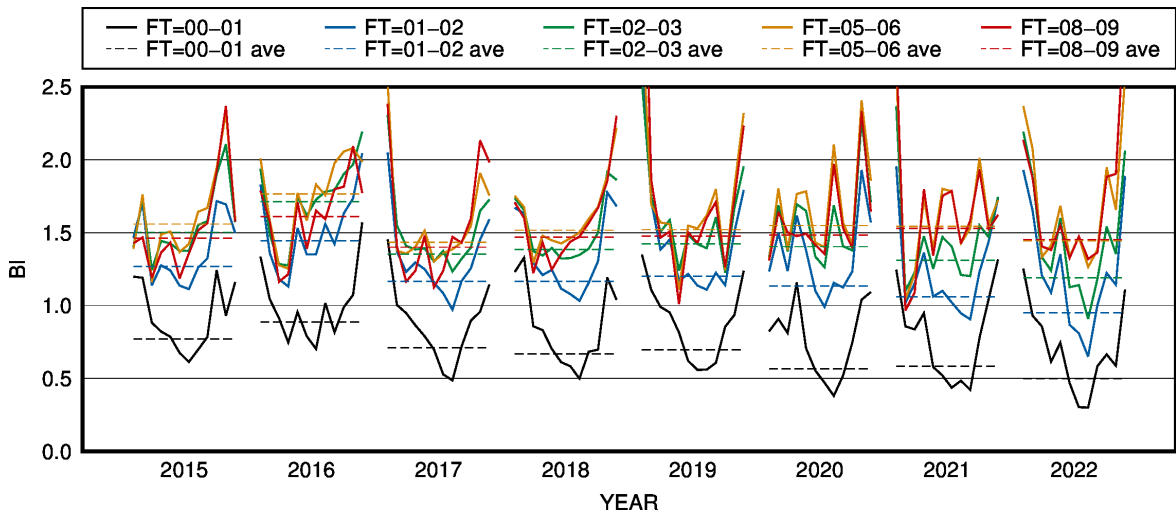
Figure 3.7.2: As per Figure 3.7.1 but for bias scores

133
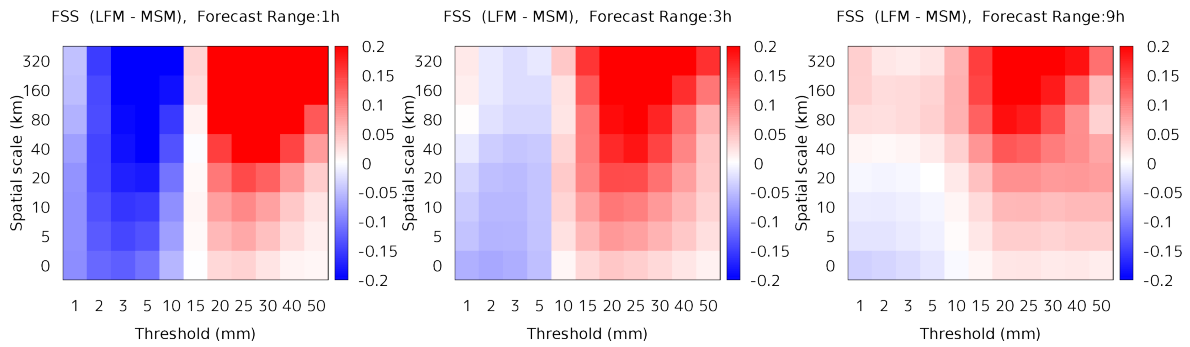
Figure 3.7.3: Monthly averaged subtraction of Fraction Skill Scores for MSM one-hour cumulative precipitation from those of the LFM. The forecast ranges are one, three and nine hours. The verification period is July 2022.
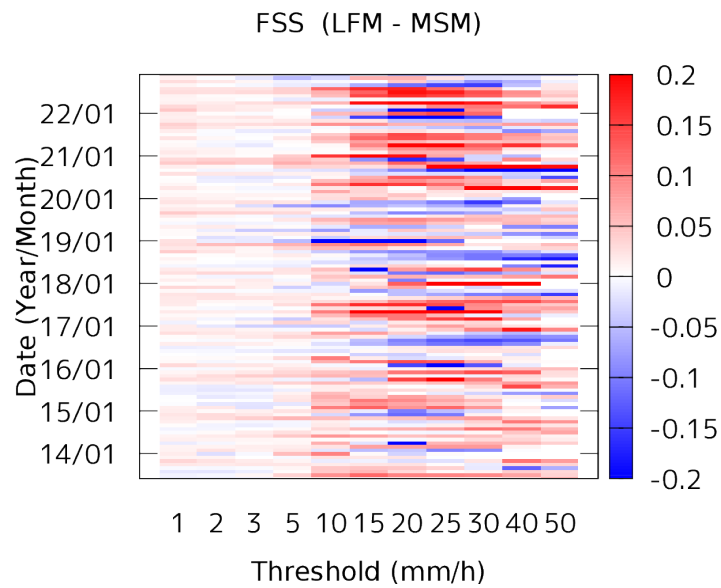
Figure 3.7.4: Monthly averaged subtraction of Fraction Skill Scores for MSM one-hour cumulative precipitation from those of the LFM. The forecast range is nine hours and the spatial scale is 80 km. The verification period is from June 2013 to December 2022.

3.8 Atmospheric Transport and Dispersion Model

3.8.1 Introduction

In July 1997, JMA was designated as a Regional Specialized Meteorological Centre (RSMC) specializing in the provision of atmospheric transport and dispersion model (ATDM) products for environmental emergency response covering Regional Association II (RA-II) of the World Meteorological Organization (WMO). RSMC Tokyo is required to provide advice on the atmospheric transport of pollutants related to nuclear facility accidents and radiological emergencies. The RSMC's ATDM products are sent to the National Meteorological Services (NMS) of WMO Member States in RA-II and to the secretariats of WMO and of the International Atomic Energy Agency (IAEA). The basic procedure of the service is defined in WMO (2019).

3.8.2 Model

3.8.2.1 Basic Model Description

The ATDM used by JMA is based on Iwasaki *et al.* (1998) with modifications developed by Kawai (2002). It involves the use of a Lagrangian approach in which tracer particles released at the temporal and spatial points of pollutant emission are displaced due to horizontal and vertical advection and diffusion and laid down through dry and wet deposition. Computation of advection, dispersion (turbulent diffusion) and deposition is based on the output of the operational numerical weather prediction (NWP) model, involving three-hourly model-level global model (GSM; see Section 3.2) outputs with temporal and spatial interpolation to tracer points. A total of 1,000,000 tracer particles are used in the operational ATDM, and time-integrated concentration and deposition are calculated using 0.5x0.5-degree latitude-longitude grids.

Horizontal velocities of tracers are estimated in accordance with Gifford (1982) as

$$u(t) = u_{\mathrm{m}}(t) + u'(t),$$
$$u'(t) = R_{\mathrm{h}} u'(t - \delta t) + \sqrt{1 - R_{\mathrm{h}}^2}\, \sigma G, \tag{3.8.1}$$

$$v(t) = v_{\mathrm{m}}(t) + v'(t),$$
$$v'(t) = R_{\mathrm{h}} v'(t - \delta t) + \sqrt{1 - R_{\mathrm{h}}^2}\, \sigma G, \tag{3.8.2}$$

where u and v are zonal and meridional wind speed components, and u_m and v_m are those of forecast values from the global NWP system. R_{h} is an autocorrelation of Lagrangian velocity as estimated using $e^{-\delta t/T_{\mathrm{L}}}$, where δt is the single time step length and T_{L} is the Lagrangian time scale. σ is the root mean square of horizontal velocity, which can be estimated as $(K_{\mathrm{h}}/T_{\mathrm{L}})^{1/2}$ with reference to the horizontal diffusion coefficient K_{h}. G represents random fluctuation whose statistical distributions have the Gaussian distribution function with a mean of 0 and a standard deviation of 1. The Monte Carlo method is used to determine velocities and displacements of each tracer particle. The horizontal diffusion coefficient K_{h} needs to be parameterized in consideration of the model resolution and the temporal and spatial variations of meteorological fields.

An appropriate constant value is set to reduce the computational time burden. Horizontal displacements δx and δy are given by

$$\delta x = u(t)\delta t, \tag{3.8.3}$$
$$\delta y = v(t)\delta t. \tag{3.8.4}$$

The vertical displacement δz for a single time step δt is given as

$$\delta z = w_{\mathrm{m}}(t)\delta t + \Sigma G \sqrt{2K_{\mathrm{v}}\delta t'}. \tag{3.8.5}$$

Here, w_{m} is the vertical wind speed given by the GSM forecast. The vertical diffusion coefficient depends on atmospheric vertical profiles. The time step for the integration of vertical diffusion $\delta t'$ is much shorter than

those for the integration of horizontal diffusion and advection. This shorter time step is used so that vertical displacement caused by diffusion does not exceed the thickness of the model layer. The vertical diffusion coefficient K_v is set with reference to meteorological parameters processed by the NWP model in a way analogous to the molecular diffusion coefficient estimation of Louis *et al.* (1982), and is given as follows:

$$K_v = l^2 \left| \frac{\partial c}{\partial z} \right| F(R_i), \tag{3.8.6}$$

where c is the horizontal wind speed, and the parameters l and R_i are the vertical mixing length of turbulence and the flux Richardson number, respectively. The similarity function of $F(R_i)$ is defined with reference to Louis *et al.* (1982). The mixing length is expressed as a function of the geometric height z:

$$l = \frac{\kappa z}{1 + \kappa z/l_0} \tag{3.8.7}$$

where κ is von Kármán's constant and l_0 is the maximum mixing length.

3.8.2.2 Dry and Wet Deposition

The surface tracer flux F associated with dry deposition is presented using deposition velocity $V(z_r)$ and concentration $C(z_r)$ at the reference level z_r as

$$F \equiv V(z_r)C(z_r). \tag{3.8.8}$$

For simplicity, the deposition rate is set to F/z_r following Kitada *et al.* (1986).

For wet deposition, only wash-out processes are parameterized. The wet deposition rate $\Lambda[1/h]$ is approximated as a function of precipitation intensity $P[mm/h]$ as predicted by the GSM with the below-cloud scavenging ratio per hour given by Kitada (1994) as

$$\Lambda \approx 0.1 P^{0.75}. \tag{3.8.9}$$

The Monte Carlo method is applied to decide which tracer particles are removed from the atmosphere at the above-mentioned dry and wet deposition rates. Noble gases such as ^{133}**Xe** are excluded from these depositing treatments.

3.8.3 Products

ATDM products are charts of 3D trajectories, time-integrated pollutant concentrations, total depositions. Sample charts are shown in Figures 3.8.1 - 3.8.7, and information on related interpretation is provided in Appendix 2.2.22 of WMO (2019).

3-D TRAJECTORY

FROM 21UTC 1 OCT 2018 TO 00UTC 5 OCT 2018
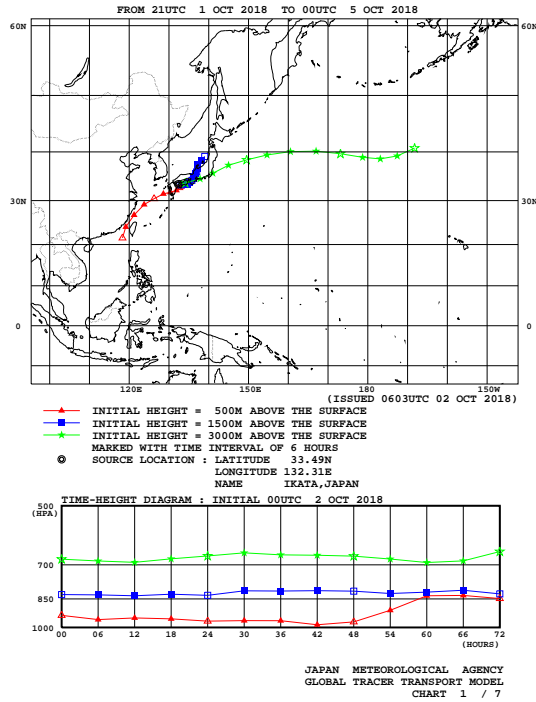
INITIAL HEIGHT = 500M ABOVE THE SURFACE
INITIAL HEIGHT = 1500M ABOVE THE SURFACE
INITIAL HEIGHT = 3000M ABOVE THE SURFACE
MARKED WITH TIME INTERVAL OF 6 HOURS
SOURCE LOCATION : LATITUDE   33.49N
                 LONGITUDE 132.31E
                 NAME   IKATA,JAPAN

TIME-HEIGHT DIAGRAM : INITIAL 00UTC 2 OCT 2018

(ISSUED 0603UTC 02 OCT 2018)

JAPAN METEOROLOGICAL AGENCY
GLOBAL TRACER TRANSPORT MODEL
CHART 1 / 7

Figure 3.8.1: Example of the 3D trajectories

TIME INTEGRATED SURFACE - 500m LAYER CONCENTRATION

INTEGRATED FROM 00UTC 2 OCT 2018
            TO   00UTC 3 OCT 2018

(ISSUED 0603UTC 02 OCT 2018)

ASSUMED POLLUTANT RELEASED : I -131
START OF THE EMISSION   : 2100UTC 1 OCT 2018
END   OF THE EMISSION   : 0300UTC 2 OCT 2018
        SOURCE LOCATION : LATITUDE   33.49N
                          LONGITUDE 132.31E
                          NAME   IKATA,JAPAN
ASSUMED TOTAL EMISSION :   7.53 *10^{18} Becquerel
UNIFORM RELEASE FROM   20- 500m ABOVE THE GROUND
UNIT   : Bq.s/m³
          MAXIMUM : 7.49*10^{10} (Bq.s/m³)
CONTOURS: 10^{10} , 10^{8} , 10^{6} , 10^{4} Bq.s/m³

JAPAN METEOROLOGICAL AGENCY
GLOBAL TRACER TRANSPORT MODEL
CHART 2 / 7

TIME INTEGRATED SURFACE - 500m LAYER CONCENTRATION

INTEGRATED FROM 00UTC 3 OCT 2018
            TO   00UTC 4 OCT 2018

(ISSUED 0603UTC 02 OCT 2018)

ASSUMED POLLUTANT RELEASED : I -131
START OF THE EMISSION   : 2100UTC 1 OCT 2018
END   OF THE EMISSION   : 0300UTC 2 OCT 2018
        SOURCE LOCATION : LATITUDE   33.49N
                          LONGITUDE 132.31E
                          NAME   IKATA,JAPAN
ASSUMED TOTAL EMISSION :   7.53 *10^{18} Becquerel
UNIFORM RELEASE FROM   20- 500m ABOVE THE GROUND
UNIT   : Bq.s/m³
          MAXIMUM : 1.48*10^{9} (Bq.s/m³)
CONTOURS: 10^{8} , 10^{6} , 10^{4} Bq.s/m³

JAPAN METEOROLOGICAL AGENCY
GLOBAL TRACER TRANSPORT MODEL
CHART 3 / 7

Figure 3.8.2: Example of time-integrated concentration in forecasts of up to 24 hours

Figure 3.8.3: Example of time-integrated concentration in forecasts of up to 48 hours

137

TIME INTEGRATED SURFACE - 500m LAYER CONCENTRATION
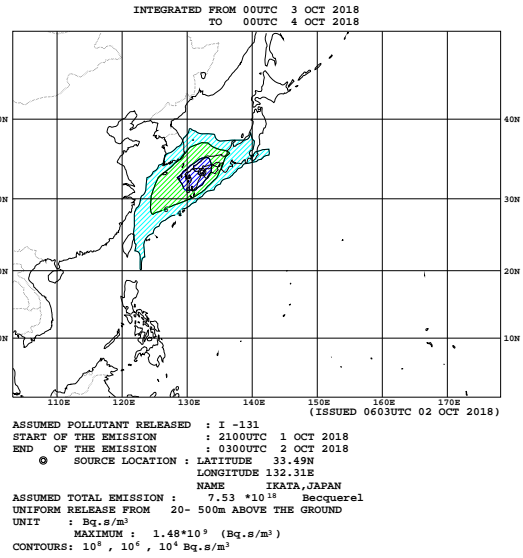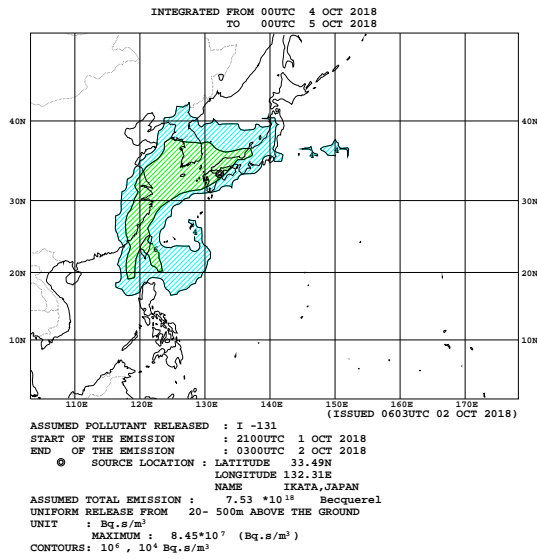
INTEGRATED FROM 00UTC 4 OCT 2018
TO   00UTC 5 OCT 2018

(ISSUED 0603UTC 02 OCT 2018)

ASSUMED POLLUTANT RELEASED : I -131
START OF THE EMISSION   : 2100UTC 1 OCT 2018
END   OF THE EMISSION   : 0300UTC 2 OCT 2018
  ◎   SOURCE LOCATION : LATITUDE   33.49N
                         LONGITUDE 132.31E
                         NAME   IKATA,JAPAN
ASSUMED TOTAL EMISSION :   7.53 *10¹⁸   Becquerel
UNIFORM RELEASE FROM   20- 500m ABOVE THE GROUND
UNIT   : Bq.s/m³
            MAXIMUM : 8.45*10⁷ (Bq.s/m³)
CONTOURS: 10⁶ , 10⁴ Bq.s/m³

JAPAN METEOROLOGICAL AGENCY
GLOBAL TRACER TRANSPORT MODEL
CHART 4 / 7
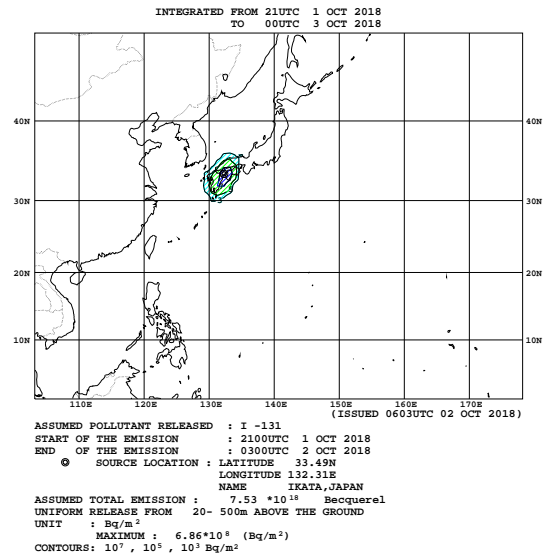
Figure 3.8.4: Example of time-integrated concentration in forecasts of up to 72 hours

TOTAL (WET AND DRY) DEPOSITION

INTEGRATED FROM 21UTC 1 OCT 2018
TO   00UTC 3 OCT 2018

(ISSUED 0603UTC 02 OCT 2018)

ASSUMED POLLUTANT RELEASED : I -131
START OF THE EMISSION   : 2100UTC 1 OCT 2018
END   OF THE EMISSION   : 0300UTC 2 OCT 2018
  ◎   SOURCE LOCATION : LATITUDE   33.49N
                         LONGITUDE 132.31E
                         NAME   IKATA,JAPAN
ASSUMED TOTAL EMISSION :   7.53 *10¹⁸   Becquerel
UNIFORM RELEASE FROM   20- 500m ABOVE THE GROUND
UNIT   : Bq/m²
            MAXIMUM : 6.86*10⁸ (Bq/m²)
CONTOURS: 10⁷ , 10⁵ , 10³ Bq/m²

JAPAN METEOROLOGICAL AGENCY
GLOBAL TRACER TRANSPORT MODEL
CHART 5 / 7

Figure 3.8.5: Example of total deposition in forecasts of up to 24 hours

TOTAL (WET AND DRY) DEPOSITION

INTEGRATED FROM 21UTC 1 OCT 2018
TO   00UTC 4 OCT 2018

(ISSUED 0603UTC 02 OCT 2018)

ASSUMED POLLUTANT RELEASED : I -131
START OF THE EMISSION   : 2100UTC 1 OCT 2018
END   OF THE EMISSION   : 0300UTC 2 OCT 2018
  ◎   SOURCE LOCATION : LATITUDE   33.49N
                         LONGITUDE 132.31E
                         NAME   IKATA,JAPAN
ASSUMED TOTAL EMISSION :   7.53 *10¹⁸   Becquerel
UNIFORM RELEASE FROM   20- 500m ABOVE THE GROUND
UNIT   : Bq/m²
            MAXIMUM : 6.37*10⁸ (Bq/m²)
CONTOURS: 10⁷ , 10⁵ , 10³ Bq/m²

JAPAN METEOROLOGICAL AGENCY
GLOBAL TRACER TRANSPORT MODEL
CHART 6 / 7
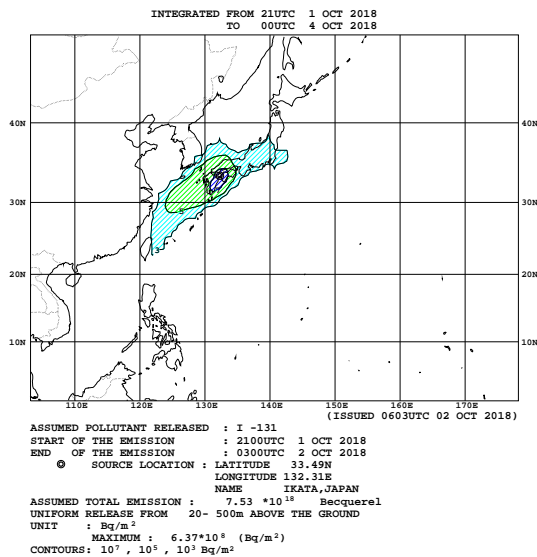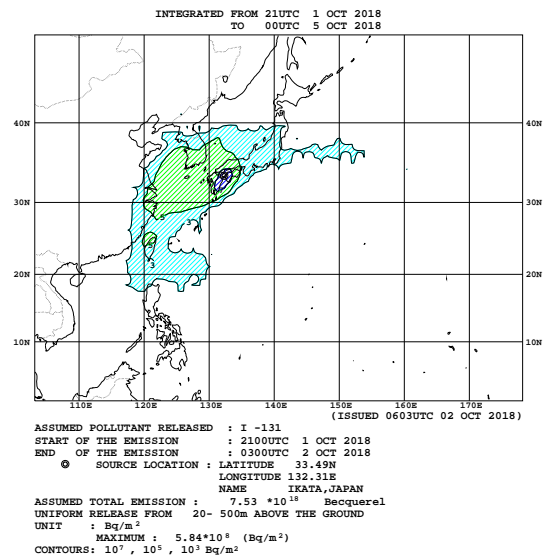
Figure 3.8.6: Example of total deposition in forecasts of up to 48 hours

TOTAL (WET AND DRY) DEPOSITION

INTEGRATED FROM 21UTC 1 OCT 2018
TO   00UTC 5 OCT 2018

(ISSUED 0603UTC 02 OCT 2018)

ASSUMED POLLUTANT RELEASED : I -131
START OF THE EMISSION   : 2100UTC 1 OCT 2018
END   OF THE EMISSION   : 0300UTC 2 OCT 2018
  ◎   SOURCE LOCATION : LATITUDE   33.49N
                         LONGITUDE 132.31E
                         NAME   IKATA,JAPAN
ASSUMED TOTAL EMISSION :   7.53 *10¹⁸   Becquerel
UNIFORM RELEASE FROM   20- 500m ABOVE THE GROUND
UNIT   : Bq/m²
            MAXIMUM : 5.84*10⁸ (Bq/m²)
CONTOURS: 10⁷ , 10⁵ , 10³ Bq/m²

JAPAN METEOROLOGICAL AGENCY
GLOBAL TRACER TRANSPORT MODEL
CHART 7 / 7

Figure 3.8.7: Example of total deposition in forecasts of up to 72 hours

3.9 Chemical Transport Model

3.9.1 Global CTM for UV Index Forecasting

3.9.1.1 Introduction

JMA provides distributions and time-series representations of UV index forecasts via its website (Figure 3.9.1 and Figure 3.9.2) based on a prediction system introduced in May 2005. UV index is calculated using a global chemical transport model (CTM) that predicts the global distribution of ozone along with a radiative transfer model. In October 2014, ozone chemistry modeling was updated with a new version of the chemistry-climate model (Deushi and Shibata 2011), which is part of the Earth System Model (MRI-ESM1; Yukimoto *et al.* 2011), and its horizontal resolution was enhanced from T42 to TL159. Nudging for total column ozone assimilation is also implemented.
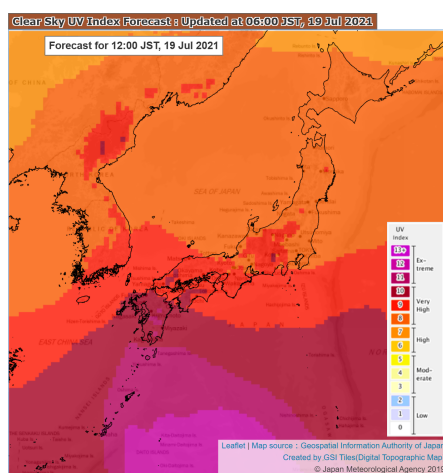
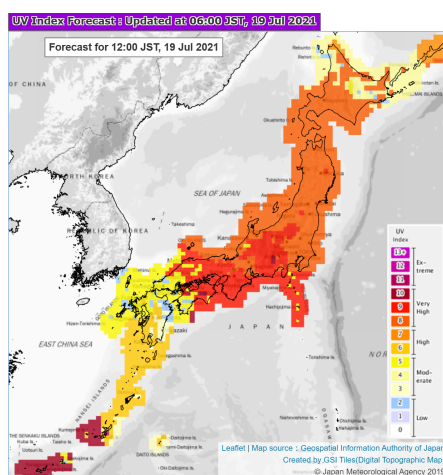Figure 3.9.1: Clear-sky UV index forecast provided once a day (https://www.data.jma.go.jp/env/uvindex/en/).

Figure 3.9.2: UV index forecast provided twice a day (https://www.data.jma.go.jp/env/uvindex/en/).

3.9.1.2 Basic Framework

The Meteorological Research Institute Chemical Climate Model version 2.1 (MRI-CCM2.1) developed by Deushi and Shibata (2011) and Yukimoto *et al.* (2019) is a global CTM used to predict distribution of atmospheric ozone and related trace gases (see Table 3.9.1 for specifications). The chemical reaction scheme is based on chemical families method, with a module incorporating 90 chemical species (64 long-lived and 26 short-lived; Table 3.9.2). In the latest module version, 266 chemical reactions are considered (191 gas-phase, 59 photolysis and 16 heterogeneous). The CTM prediction period is 120 hours and the resolution is TL159L64 (approx. 110 km horizontal-grid intervals and 64 vertical layers up to 0.01 hPa). In addition to chemical reactions, the module also treats grid scale transport with a semi-Lagrangian scheme, sub-grid scale convective transport and turbulent diffusion, dry and wet deposition and emission of trace gases from various sources.

Table 3.9.1: Global CTM specifications.

Basic equations	Eulerian model coupled with Global Spectral Model
Numerical technique	3D semi-Lagrangian transport and chemical reaction
Integration domain	Global
Grid size	TL159 (1.125°)
Vertical levels	64 (surface – 0.01 hPa)
Initial and forecast times	120 hours from 12 UTC (daily)
Boundary conditions	Similar to Global Spectral Model
Forcing data (nudging)	Global analysis (GA) and Global Spectral Model (GSM) forecasts
Observational data	Total column ozone from OMPS/NOAA

The dynamic module in the global CTM has an assimilation process in the meteorological field. Nudging (as outlined in Eq. (3.9.1)) is applied to operational global atmospheric analysis and forecasting during the CTM integration period. This starts 72 hours prior to UV index analysis and ends 48 hours after the prediction period.

3.9.1.3 Coupling of Chemical and Meteorological Parts

The chemical modules are coupled with the dynamical module with derivation of meteorological fields such as wind, temperature and precipitation as required in chemical computation (Figure 3.9.3). In the global CTM used for ozone prediction, chemical modules are directly coupled with the Atmospheric General Circulation Model (MRI-AGCM3; Mizuta *et al.* 2012) developed by the Meteorological Research Institute (MRI) of JMA as part of MRI-ESM1. Online coupling is achieved using Scup coupler software (Yoshimura and Yukimoto 2008).

CTMs generally require more computational resources than atmospheric global circulation models (AGCMs) due to the need for handling of more chemical variables and processes. Accordingly, global CTMs require lower spatial resolution in operational use, and the spatial resolution of the atmospheric model in the global CTM differs from that of the GCM used for operational meteorological analysis and forecasting (Section 3.2). There may also be differences in adopted model processes between the operational AGCM and the dynamical module of the global CTM. As a result, meteorological fields computed in the CTM are not necessarily consistent with those of operational meteorological analysis and forecasting. The nudging technique shown in Eq. (3.9.1) is often utilized optimize CTM prediction accuracy:

$$\left(\frac{\partial x}{\partial t}\right)_{nudging} = -\frac{x - x_{analysis/forecast}}{\tau} \tag{3.9.1}$$

Here, x is a meteorological variable of the CTM at a certain time t, $x_{analysis/forecast}$ is the corresponding analysis or forecast value derived from the higher-resolution operational AGCM, and τ is a relaxation time of $6 - 24$ hours. This technique enables the CTM to simulate meteorological fields realistically for the prediction period.

Table 3.9.2: Species used in the atmospheric ozone CTM.

Long-lived			
01: N_2O	02: CH_4	03: H_2O	04: NO_y
05: HNO_3	06: N_2O_5	07: Cl_y	08: O_x
09: CO	10: OClO	11: CO_2	12: Passive tracer
13: HCl	14: $ClONO_2$	15: HOCl	16: Cl_2
17: H_2O_2	18: $ClNO_2$	19: HBr	20: $BrONO_2$
21: NO_x	22: HO_2NO_2	23: ClO_x	24: BrO_x
25: Cl_2O_2	26: HOBr	27: CCl_4(CFC-10)	28: $CFCl_3$(CFC-11)
29: CF_2Cl_2(CFC-12)	30: Br_y	31: CH_3Cl	32: CH_3Br
33: CF_2ClBr (Halon1211)	34: CF_3Br (Halon1301)	35: COF_2	36: HF
37: CH_2O	38: CH_3OOH	39: C_2H_6	40: CH_3CHO
41: C_2H_5OOH	42: PAN ($CH_3C(O)OONO_2$)	43: $CH_3C(O)OOH$	44: C_3H_8
45: ACET ($CH_3C(O)CH_3$)	46: C_3H_7OOH	47: HACET ($CH_3C(O)CH_2OH$)	48: MGLY ($CH_3C(O)CHO$)
49: C_2H_4	50: GLY ALD ($HOCH_2CHO$)	51: GPAN ($HOCH_2C(O)OONO_2$)	52: GC(O)OOH ($HOCH_2C(O)OOH$)
53: C_3H_6	54: ONIT ($CH_3C(O)CH_2ONO_2$)	55: POOH (HOC_3H_6OOH)	56: C_4H_{10}
57: C_5H_8 (isoprene)	58: MACR	59: ISON	60: ISOPOOH
61: NALD	62: MACROOH	63: MPAN	64: $C_{10}H_{16}$ (terpenes)

Short-lived			
01: O(1D)	02: OH	03: Cl	04: O(3P)
05: O_3	06: HO_2	07: NO_2	08: NO
09: Br	10: N	11: ClO	12: BrO
13: NO_3	14: BrCl	15: H	16: CH_3O_2
17: $C_2H_5O_2$	18: $CH_3C(O)O_2$	19: $C_3H_7O_2$	20: $ACETO_2$ ($CH_3C(O)CH_2O_2$)
21: EO_2 ($HOC_2H_4O_2$)	22: EO (HOC_2H_4O)	23: $GC(O)O_2$ ($HOCH_2C(O)O_2$)	24: PO_2 ($HOC_3H_6O_2$)
25: $ISOPO_2$	26: $MACRO_2$		

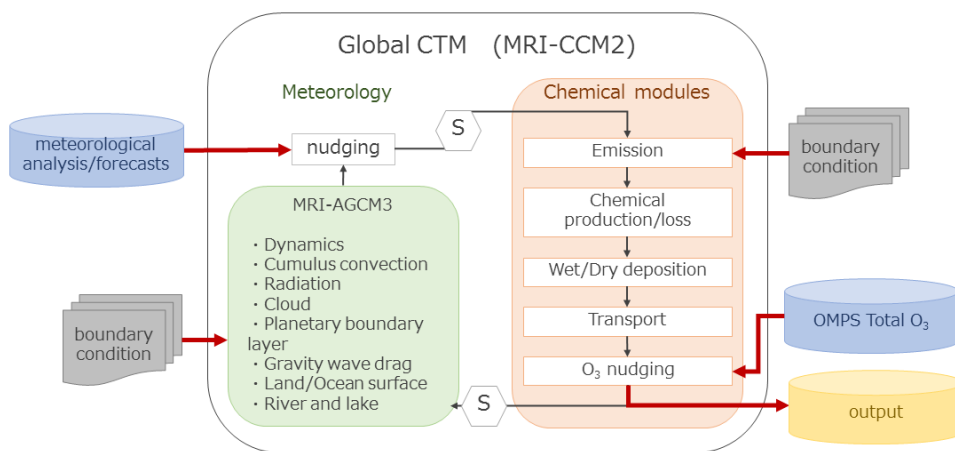| Chemical families |
|---|
| $O_x = O_3 + O(3P) + O(1D)$ |
| $ClO_x = Cl + ClO$ |
| $Cl_y = ClO_x + OClO + 2Cl_2O_2 + HCl + ClONO_2 + HOCl + 2Cl_2 + ClNO_2 + BrCl$ |
| $NO_x = NO + NO_2 + NO_3$ |
| $NO_y = NO_x + N + HNO_3 + 2N_2O_5 + HO_2NO_2 + ClONO_2 + ClNO_2 + BrONO_2 + PAN + GPAN + ONIT + ISON + NALD + MPAN$ |
| $BrO_x = Br + BrO + BrCl$ |
| $Br_y = BrO_x + HBr + HOBr + BrONO_2$ |

Figure 3.9.3: Global CTM ("S": Scup coupler).

3.9.1.4 Data Assimilation

The chemical module in the global CTM also has an assimilation process and total column ozone from Ozone Mapping and Profiler Suite (OMPS/NOAA-20) satellite monitoring is assimilated every hour based on

$$x_{assimilated} = x_{guess} - w(x_{guess} - x_{obs}) \qquad (3.9.2)$$

Here, x is total column ozone, x_{guess} is the model guess, x_{obs} is OMPS data and $x_{assimilated}$ is the value after assimilation. The weight of the model guess with OMPS data (w in Eq. (3.9.2)) is 3/4, as determined by the ratio of the root mean square error against surface observation using a Dobson and Brewer spectrophotometer. OMPS data obtained within 72 hours prior to the UV index analysis time are assimilated into the CTM.

3.9.1.5 Verification

Figure 3.9.4 compares assimilated and observed ozone profiles for 2015. For all heights, the mean differences are within around 0.5 ppmv and the root mean square errors (RMSEs) of simulation against observation are less than 0.8 ppmv.

3.9.1.6 Radiative Transfer Model for UV Index Forecasting

The surface UV dose is calculated under clear-sky conditions using the radiative transfer model (Aoki *et al.* 2002) in an area from 122 to 149°E and from 24 to 46°N with a grid resolution of $0.25 \times 0.20°$. Look-up table (LUT) method is used to calculate the surface UV dose for reduced computational cost. The basic parameters of the LUT for the clear-sky UV dose are the solar zenith angle and total column ozone predicted using the CTM. The clear-sky UV index is derived from the clear-sky UV dose corrected in consideration of climatological aerosol optical depth, distance from the sun, altitude and climatological surface albedo. The UV index is derived from correction of the clear-sky UV index with cloud information from the operational weather forecast (see Table 3.9.3 for specifications).
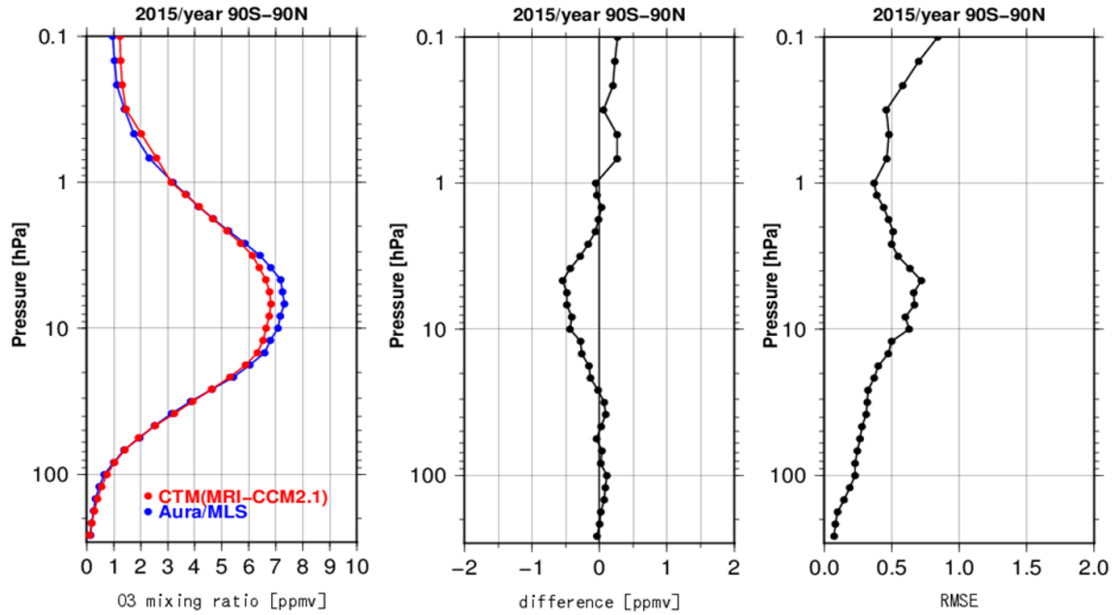
Figure 3.9.4: Annual mean vertical ozone profiles for 2015 averaged over the globe. Left: ozone mixing ratio for the CTM (red) and satellite observation (blue,Aura/MLS); middle: mixing ratio differences; right: root mean square error.

Table 3.9.3: Radiative Transfer Model specifications.

Basic equations	Radiative transfer equations for multiple scattering and absorption by atmospheric molecules and aerosols
Numerical technique	Doubling and adding
Spectral region and resolution	280 – 400 nm and 0.5 nm

The clear-sky UV index calculated using the LUT is verified against the observed UV index for clear-sky conditions (Figure 3.9.5). The mean error of the calculated clear-sky UV index is 0.1 and the RMSE is 0.4. Modeled UV indices agree closely with observation values.
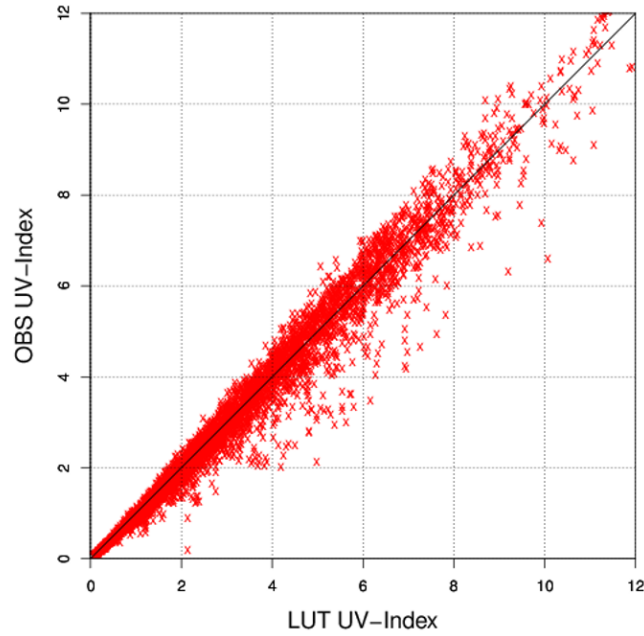

Figure 3.9.5: Relationship between calculated clear-sky UV indices and observed UV indices for clear-sky conditions at three JMA stations from 2015 to 2017.

3.9.2 Regional CTM Used for Photochemical Oxidant Information

3.9.2.1 Introduction

Based on operational predictions made using a regional CTM, JMA provides local governments with photochemical oxidant information to support the issuance of related advisories. The Agency began to utilize a global CTM (Subsection 3.9.1) for this information in August 2010, and switched to a regional CTM in March 2015. A finer-resolution local CTM nested from the regional model was also introduced for these information in March 2020. Assimilation of surface ozone concentration observation data began in March 2017 for the regional CTM, and in June 2022 for the local CTM. The calculation domain of the local CTM was expanded and the local CTM was directly nested from the global CTM in February 2023, since when the previous regional CTM has been stopped and the local CTM has been referred to by the term "new regional CTM".

3.9.2.2 Basic Framework

The regional chemical transport model for photochemical smog bulletins covering the Japan and its surrounding area was developed by Kajino *et al.* (2019, 2022) (see Table 3.9.4 for specifications). The CTM, known as ASUCA-Chem or NHM-Chem, has a horizontal resolution of 5×5 km in Lambert coordinates and a vertical resolution of 19 layers from the surface to 10 km in terrain-following coordinates. The regional CTM uses output from the operational Meso-Scale Model (MSM), known as ASUCA (Ishida *et al.* 2022), as meteorological fields to run chemical modules with offline coupling (Figure 3.9.6). In this model, 72 chemical species and 214 reactions as per SAPRC99 (Carter 2000) are treated, and major processes for atmospheric trace species such as emissions, advection, turbulent diffusion, sub-grid scale convection and dry/wet deposition are incorporated. ASUCA-Chem also implements a fully dynamic aerosol module with a three-moment bulk model using a modal-moment dynamics approach. However, in the operational version of ASUCA-Chem used for surface photochemical oxidant prediction, aerosol dynamics are fully resolved but simplified in the interests of computational efficiency.

The lateral and upper boundaries for ozone and several related species are nested from the global CTM described in Subsection 3.9.1. The natural and anthropogenic emission inventory dataset listed in Table 3.9.5 is adopted for the regional CTM. NHM-Chem source code is available subject to licensing with JMA, and further resources, including a user's manual and analysis tools, can be provided by the Meteorological Research Institute upon request.
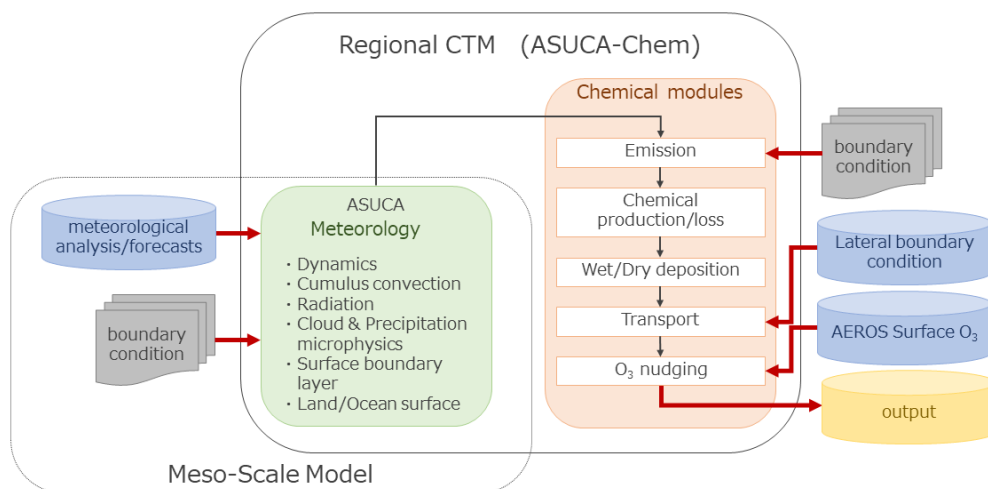
Figure 3.9.6: As per Figure 3.9.3, but for the regional CTM.

Table 3.9.4: Regional CTM specifications.

Model type	3-dimensional Eulerian chemical transport model
Area	Around Japan
Grid size	5 km
Vertical levels	19 (surface – 10 km)
Initial and forecast times	51 hours from 12 UTC (daily)
Meteorological fields	Meso-Scale Model (MSM) output
Boundary conditions	Global Chemical Transport Model (CTM)
Observational data	Surface ozone concentration from the Atmospheric Environmental Regional Observation System (AEROS)

3.9.2.3   Relaxation to Observational Data

The regional CTM is operated for a period of 51 hours with an initial time of 12 UTC. Running of the model actually starts at 19 UTC, and surface ozone concentration data (AEROS: Atmospheric Environmental Regional Observation System in Japan) for $12 - 18$ UTC are assimilated via nudging similar to the right side of Eq. (3.9.1), expressed as:

$$\gamma \left(x_{obs}(s) \frac{x_{mdl}(k)}{x_{mdl}(1)} - x_{mdl}(k) \right) \tag{3.9.3}$$

Analysis of ozone concentration in the planetary boundary layer (the k-th model layer) is based on model guess concentration $x_{mdl}(k)$ and modified using surface observation $x_{obs}(s)$ with the nudging factor γ as 1×10^{-3} [s^{-1}].

3.9.2.4   Verification

Simulated surface ozone was compared with hourly in-situ observation in the calculation domain from April to September in 2022. The mean error, RMSE and correlation coefficient of one-day-ahead forecasting for spring/summer were 0.2/4.2 ppb, 13.3/14.7 ppb, and 0.69/0.71, respectively.

Table 3.9.5: Emission inventories of trace gases used in the regional CTM.

Inventory/reference			Emission source	Coverage
REAS2	Regional Emission inventory in Asia, version 2	Ohara *et al.* (2007)	Anthropogenic	East Asia
EAGrid-Japan	Asian Air Pollutant Emission Grid Database for Japan	Kannari *et al.* (2007)	Anthropogenic	Japan
GFED3	Global Fire Emission Database, version 3	Giglio *et al.* (2010)	Natural	Global
MEGAN2	Model of Emission of Gases and Aerosols from Nature, version 2	Guenther *et al.* (2006)	Natural	Global

3.10 Kosa (Aeolian Dust) Analysis Prediction Model

3.10.1 Introduction

JMA provides Kosa (Aeolian dust) forecasts via its website once a day (Figure 3.10.1) based on a prediction system introduced in January 2004. The data are provided to relevant local governments and to the Japan Meteorological Business Support Center (JMBSC), which in turn provides the data to commercial meteorological operators. Forecasts are also provided for the WMO Sand and Dust Storm Warning Advisory and Assessment System (SDS-WAS) Asia node of the China Meteorological Administration in Beijing. The model was updated to a new version based on an Earth-system model (MRI-ESM1; Yukimoto *et al.* 2011; Yukimoto *et al.* 2012) for global climate change research in November 2014, and the horizontal resolution was enhanced from TL159 to TL479 in February 2017. Dust emission flux calculation was updated to encompass the scheme of Tanaka and Chiba (2005) in November 2014. JMA's aerosol data assimilation system and Kosa analysis were introduced in January 2020.

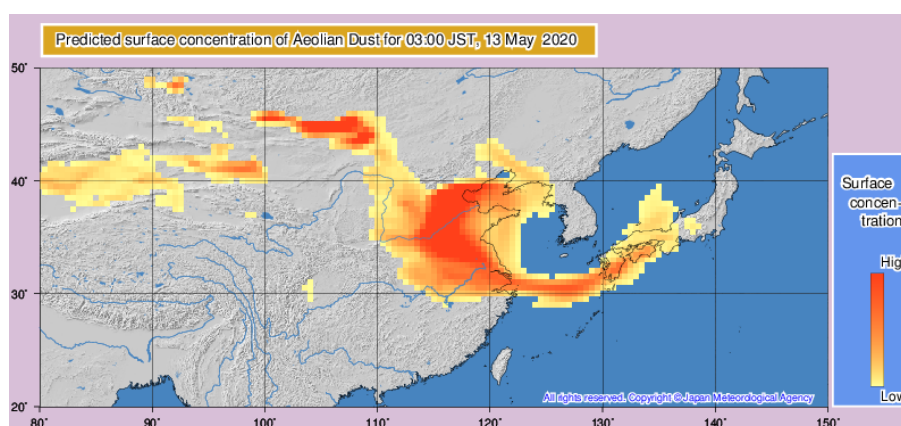Figure 3.10.1: Prediction for surface concentration of Kosa (Aeolian dust) (`https://www.data.jma.go.jp/env/kosa/fcst/en/`). Data on the total amount of airborne Kosa are also provided (not shown).

3.10.2 Basic Framework

The MASINGAR (Model of Aerosol Species IN the Global AtmospheRe; Tanaka *et al.* 2003) chemical transport model used for Kosa (Aeolian dust) prediction consists of transport modules for advective transport with a semi-Lagrangian scheme and sub-grid scale eddy diffusive/convective transport, as well as other modules of surface emission, dry/wet deposition and chemical reactions (see Table 3.10.1 for specifications). It treats sulfate, black carbon, organic carbon, mineral dust and sea salt as major tropospheric aerosol species with the assumption of external mixing. The chemical module is directly coupled with MRI-AGCM3 using Scup coupler software as per the CTM for UV index forecasting (Subsection 3.9.1.3) as shown in Figure 3.10.2.

147

Assimilation for the meteorological field (U, V, T) involves Newtonian nudging, which is essentially the same as for the CTM for UV index forecasting (Eq. (3.9.1)). The prediction period is 96 hours, and the spatial resolution is TL479L40 (horizontal grid interval: approx. 40 km; 40 vertical layers up to 0.4 hPa in sigma-pressure hybrid coordinates).

The emission flux of mineral dust aerosol depends on meteorological, geographical and soil-surface conditions such as wind speed, land use, vegetation type, soil moisture and soil type. The emission flux F of dust (soil particles with diameter D) is expressed in proportion to the saltation flux Q:

$$F(D) = \alpha(D, d_s) Q(d_s) \tag{3.10.1}$$

Here, d_s is the diameter of saltation particles, and the proportional coefficient α depends on both D and d_s. The saltation flux Q is zero when the friction velocity on a bare surface u_* is lower than the following threshold velocity:

$$u_{*t}(d_s) = f_w \sqrt{A_N \left(\frac{\rho g d_s}{\rho_a} + \frac{\Gamma}{\rho_a d_s} \right)} \tag{3.10.2}$$

Here, A_N and Γ are empirical constants, ρ is soil particle density, ρ_a is air density, g is gravitational acceleration (Shao and Lu 2000) and f_w is a factor depending on soil moisture (Fećan *et al.* 1998). When u_* is greater than u_{*t}, the saltation flux is expressed as

$$Q(d_s) = \frac{c(d_s) \rho_a u_*^3}{g} \left(1 - \frac{u_{*t}(d_s)^2}{u_*^2} \right) \tag{3.10.3}$$

Here, c is a coefficient depending on d_s (Shao and Leslie 1997).

Table 3.10.1: Kosa (Aeolian dust) analysis and prediction model specifications.

Basic equations	Eulerian model coupled with Global Spectral Model
Numerical technique	3D semi-Lagrangian transport and dust emission calculation from surface meteorology
Integration domain	Global
Grid size	TL479 (0.375°)
Vertical levels	40 (surface – 0.4 hPa)
Initial and forecast times	96 hours from 12 UTC (daily)
Boundary conditions	Similar to Global Spectral Model
Forcing data (nudging)	Global Analysis (GA) and Global Spectral Model (GSM) forecasts
Data assimilation	2-dimensional variation (2D-Var)
Observational data for assimilation	Aerosol optical depth at 500 nm from AHI

3.10.3   Data Assimilation

JMA began 2D-Var aerosol data assimilation (Yumimoto *et al.* 2017) against aerosol optical depth (AOD) with the Himawari-8/9 geostationary satellite in January 2020. AOD data are obtained using the JAXA/EORC retrieval algorithm (Yoshida *et al.* 2018, 2021; Kikuchi *et al.* 2018) with a one-day analysis cycle to calculate initial conditions for five-day forecasting. Assimilation is performed using Himawari-8/9 AOD data with a ±1 hour target time at 06 UTC in the analysis cycle. AOD observation error is approximated as

$$\sigma_{obs} = \max(\sigma_{H08/09}, \alpha + \beta * \tau_{H08/09}) \tag{3.10.4}$$

Here, σ_{obs} is the AOD observation error, $\sigma_{H08/09}$ is the Himawari-8/9 AOD retrieval error, and α and β are coefficients estimated from statistical calculation of Himawari-8/9 AOD observation error against data from the Moderate Resolution Imaging Spectroradiometer (MODIS) on the Aqua satellite. These estimated values are used for observation error covariance.

AOD background error is calculated using five initial forecasting data points within ±6 hours of the target assimilation time (Yumimoto *et al.* 2018). As output is every three hours, an ensemble of 25 forecast data points is used for background error covariance.
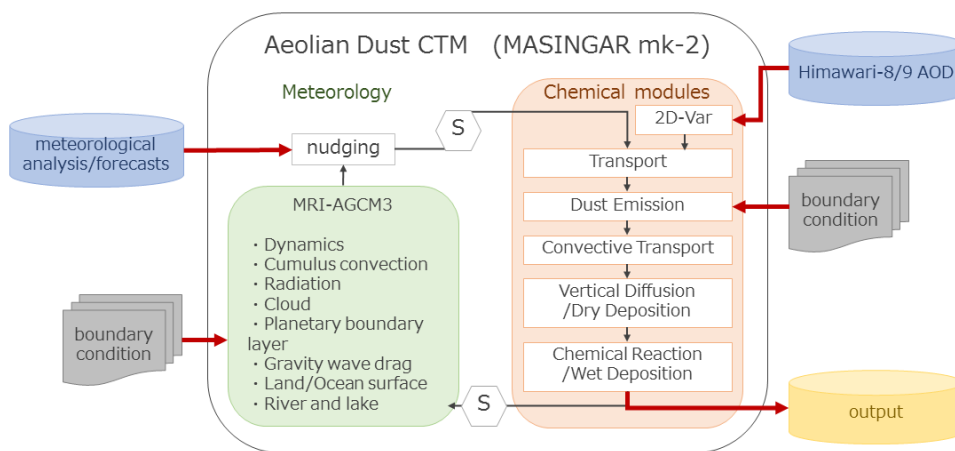
Figure 3.10.2: Kosa (Aeolian dust) CTM ("S": Scup coupler).

3.10.4 Verification

Predictions from the operational Kosa CTM are verified against surface synoptic observations (reported present weather code (ww)). The model score is calculated using categorical verification as outlined in Appendix A (Table 3.10.2). The threshold surface dust concentration value for Kosa prediction is currently 90 μg/m^3, and the threat score for Kosa prediction with/without 2D-Var after 24 hours in the Japan area is 0.28/0.26 averaged over spring (2016 − 2018).

Table 3.10.2: Verification indices for Kosa (Aeolian dust) CTM categorical prediction (*ww*: present weather code; ρ_s^{dust}: predicted surface dust concentration).

	Observed (*ww* = 06 − 09, 30 − 35, 98)	Not Observed
Forecast ($\rho_s^{dust} \geq 90\,\mu$g/m^3)	FO	FX
Not Forecast ($\rho_s^{dust} < 90\,\mu$g/m^3)	XO	XX

3.11 Verification

JMA verifies the output of Numerical Weather Prediction (NWP) model forecasts against observation and/or analysis outcomes, and the results are used as reference in research and development regarding NWP models. GSM and Global EPS verification results are exchanged between JMA and other NWP centers via the Lead Centre for Deterministic NWP Verification (LC-DNV) and the Lead Centre for EPS Verification. The standard verification procedures are defined in the Manual on the Global Data-processing and Forecasting System (WMO 2019). This section summarizes operational verification for the GSM and the Global EPS.

The specifications of GSM verification against analysis values are shown in Table 3.11.1, and the scores used for verification are presented in Appendix A.1. GSM forecast performance, including typhoon forecasting, is described in Subsection 3.2.14.

Radiosonde data and synoptic surface observation (SYNOP) data are used for verification against observation values. The specifications of verification against radiosonde data for the GSM are shown in Table 3.11.2. All radiosonde data passing quality control are used in verification. Stations from which radiosonde data are used in verification are selected on the basis of recommendations from the Commission for Basic Systems. The specifications of verification against SYNOP data for the GSM are shown in Table 3.11.3.

The specifications of verification regarding Global EPS output for One-week Forecasting are shown in Table 3.11.4. The probabilistic forecast for verification is defined as the ratio of the number of ensemble members in an event to the ensemble size for every grid. The verification results for the Global EPS are described in Subsection 3.3.6.

Table 3.11.1: Operational verification against analysis for the GSM

Verification grid	$1.5° \times 1.5°$ (latitude/longitude)	
Elements	Extra-tropics:	Geopotential height (Z) and temperature (T) at 850, 500, 250 and 100 hPa; Wind at 925, 850, 700, 500, 250 and 100 hPa; Relative humidity (RH) at 850 and 700 hPa; Mean sea-level pressure (MSLP)
	Tropics:	Z, T and wind at 850 and 250 hPa; RH at 850 and 700 hPa
Scores	Wind:	Root mean square vector wind error and mean error of wind speed
	Other elements:	Mean error, root mean square error, anomaly correlation, S1 score (only for MSLP), mean absolute error, root mean square forecast and analysis anomalies, standard deviations of forecast and analysis fields
Forecast range (initial time)	Up to 264 hours (00 and 12 UTC)	
Forecast steps	Every 12 hours	
Areas	NH extra-tropics ($90°N - 20°N$), SH extra-tropics ($20°S - 90°S$), Tropics ($20°N - 20°S$), North America ($25°N - 60°N, 50°W - 145°W$), Europe/North Africa ($25°N - 70°N, 10°W - 28°E$), Asia ($25°N - 65°N, 60°E - 145°E$), Australia/New Zealand ($10°S - 55°S, 90°E - 180°E$), Northern polar region ($90°N - 60°N$) and Southern polar region ($90°S - 60°S$)	

Table 3.11.2: Operational verification against radiosonde data for the GSM

Verification grid	Nearest model grid point to the observation location	
Elements	Extra-tropics:	Z and T at 850, 500, 250 and 100 hPa; Wind at 925, 850, 700, 500, 250 and 100 hPa; RH at 850 and 700 hPa
	Tropics:	Z, T and wind at 850 and 250 hPa; RH at 850 and 700 hPa
Scores	Wind:	Root mean square vector wind error and mean error of wind speed
	Other elements:	Mean error, mean absolute error and root mean square error
Forecast range (initial time)	Up to 264 hours (00 and 12 UTC)	
Forecast steps	Every 12 hours	
Areas	NH extra-tropics, SH extra-tropics, Tropics, North America, Europe/North Africa, Asia, Australia/New Zealand, Northern polar region and Southern polar region	

Table 3.11.3: Operational verification against SYNOP data for the GSM

Verification grid	Nearest model grid point to the observation location
Elements	T at 2 m, wind speed at 10 m, wind direction at 10 m and 24-hour precipitation
Scores	T at 2 m, wind speed at 10 m and wind direction at 10 m: Mean error, mean absolute error and root mean square error Contingency tables for following thresholds wind speed at 10 m: 5, 10 and 15 m/s 24-hour precipitation: 1, 10 and 50 mm
Forecast range (initial time)	Up to 264 hours (00 and 12 UTC)
Forecast steps	24-hour precipitation: Every 24 hours Other elements: Every 6 hours up to 72-hour forecast; Every 12 hours up to end of the forecast

Table 3.11.4: Operational verification of the Global EPS for One-week Forecasting

	Deterministic verification	Probabilistic verification	
Analysis	Global analysis on 1.5° × 1.5° grid		
Forecast	Ensemble mean	Probability	
Climatology	Climatological fields and standard deviations are calculated from common climatology provided from LC-DNV. The climatological probability is given by the monthly frequency derived from analysis fields.		
Elements	Z at 500 hPa; T at 850 hPa; u wind component (U) and v wind component (V) at 850 and 250 hPa; MSLP	Anomalies of Z at 500 hPa, T at 2 m, T at 850 hPa and MSLP with thresholds of ±1, ±1.5 and ±2 climatological standard deviation; Wind speed at 850 hPa with thresholds of 10, 15 and 25 m/s; U and V at 850 and 250 hPa with thresholds of 10th, 25th, 75th and 90th percentile points with respect to the defined climatology; 10 m wind speed with thresholds 10 and 15 m/s; 24-hour precipitation with thresholds 1, 5, 10 *and* 25 mm/24 hours	Z at 500 hPa; T at 2 m and 850 hPa; U and V at 850 and 250 hPa; Wind speed at 10 m and 850 hPa; MSLP; 24-hour precipitation
Scores	Root mean square error, and anomaly correlation	Reliability table	Continuous ranked probability score
Forecast range (initial time)	Up to 264 hours (00 and 12 UTC)		
Forecast steps	Every 24 hours		
Areas	NH extra-tropics, SH extra-tropics and Tropics		

3.12 Atmospheric Transport Model for Volcanic Ash

3.12.1 Introduction

Since April 1997, JMA has provided information on volcanic ash clouds to airlines, civil aviation authorities and related organizations in its role as the Volcanic Ash Advisory Centre (VAAC) Tokyo. JMA introduced the Global Atmospheric Transport Model (JMA-GATM) in December 2013 to create Volcanic Ash Advisories (VAAs). JMA also launched its Volcanic Ash Fall Forecast (VAFF) product based on the Regional Atmospheric Transport Model (JMA-RATM) in March 2008 (Shimbori *et al.* 2009) and updated it in spring 2015 (Hasegawa *et al.* 2015).

In March 2021, the new Atmospheric Transport Model (JMA-ATM; Shimbori and Ishii 2021) has been developed by the Meteorological Research Institute to unify the JMA-GATM and JMA-RATM, and then implemented in the JMA's supercomputer system connected to the Volcanic ash Advisory and ash fall Forecast distribution System (VAFS).

3.12.2 Initial Condition

3.12.2.1 Emission Source Parameter Model

In the case of creating VAFFs, a volcanic plume in the shape of an inverted cone is adopted as the initial condition of the JMA-ATM. The initial plume is based on information from observational reports, including eruption time and plume height, and on the duration of volcanic ash emission. For volcanic ash grain size, log-normal distribution is adopted. The probability density function of the diameter D is given by

$$f(D) = \frac{1}{\sqrt{2\pi\sigma_D^2}} \exp\left[-\frac{\log^2(D/D_{\rm m})}{2\sigma_D^2}\right] \tag{3.12.1}$$

Here, $D_{\rm m}$ is the mean diameter and σ_D is the standard deviation of distribution. The number of tracers, diameter the range and these parameters $D_{\rm m}$, σ_D are shown in Table 3.12.1.

The vertical distribution of volcanic particles in the eruption plume is calculated according to Suzuki (1983). The probability that a tracer with diameter D is released from a height of z above vent level is given as follows:

$$P(D, z) = AY(D, z)e^{-Y(D,z)} \tag{3.12.2}$$

Here, A is the normalization constant and $Y(D, z)$ is expressed as

$$Y(D, z) = \beta \frac{W(z) - w_{\rm t}(D, 0)}{w_{\rm t}(D, 0)} \tag{3.12.3}$$

with release constant β (set as 0.017). $w_{\rm t}(D, 0)$ is the terminal velocity at the height of the volcano summit as calculated using Eq. (3.12.20). $W(z)$ is the vertical velocity in the eruption column at height z, which can be represented as

$$W(z) = W_0\left(1 - \frac{z}{H}\right) \tag{3.12.4}$$

where $W_0 = \sqrt{H/H_0}\,[{\rm m\,s^{-1}}]$ is initial velocity, H is column height and $H_0 = 0.22\,{\rm m}$. The total amount of volcanic ejecta M is given as (e.g. Koyaguchi 2008)

$$M = K_M H^4 T_M \tag{3.12.5}$$

where T_M is the duration of eruption and K_M is a constant set to $193\,{\rm kg\,km^{-4}s^{-1}}$.

3.12.2.2 Initialization for Volcanic Ash Clouds

In the case of creating VAAs, the boundary of volcanic ash observed by a meteorological satellite is adopted as the initial condition of the JMA-ATM. While the ash cloud-top height can be obtained from satellite imagery,

cloud-base height is estimated using vertical wind shear. To import the shape of the observed volcanic ash cloud, an initialization method for the ash clouds has been implemented in the operational system (Ishii *et al.* 2021). This method has a low computational cost, and therefore, is suitable for creating initial conditions immediately after an eruption occurs. The specifications of tracer particles for VAAC operation are also shown in Table 3.12.1.

Table 3.12.1: JMA-ATM specifications for VAAs and VAFFs

	VAA	VAFF (Scheduled)	VAFF (Preliminary)	VAFF (Detailed)
Number of Tracer Particles	40,000	100,000		250,000
Diameter of Tracer Particles	$1 - 10\,\mu$m (for ash cloud) $10 - 100\,\mu$m (for plume)	$0.65\,\mu$m $- 96$ mm		
Mean Diameter	$7.81\,\mu$m (for ash cloud) $31.6\,\mu$m (for plume)	0.25 mm		
Standard Deviation	0.5 (for ash cloud) 1.0 (for plume)	1.0		
Forecast Time	18 hours	18 hours	1 hour	6 hours
Time Step	600 seconds (Euler)	200 seconds (4-stage Runge-Kutta)		

3.12.3 Model

3.12.3.1 Basic Framework

The JMA-ATM adopts an offline Lagrangian scheme, the time tendency of tracer variables is calculated in each process and integrated at the last time step in order that dynamical and physical processes are commutative at each time step. The location (longitude λ, latitude φ, altitude z) of each tracer after the time step Δt is given by

$$\lambda(t + \Delta t) = \lambda(t) + \left(f_\lambda^{\text{hadv}} + f_\lambda^{\text{hdif}} \right) \Delta t \tag{3.12.6}$$

$$\varphi(t + \Delta t) = \varphi(t) + \left(f_\varphi^{\text{hadv}} + f_\varphi^{\text{hdif}} \right) \Delta t \tag{3.12.7}$$

$$z(t + \Delta t) = z(t) + \left(f_z^{\text{vadv}} + f_z^{\text{vdif}} + f_z^{\text{fall}} + f_z^{\text{ddep}} + \sum_\alpha f_z^{\text{wout}(\alpha)} \right) \Delta t \tag{3.12.8}$$

Here, f represents tendency of each physical process as shown in the following Subsections 3.12.3.2 to 3.12.3.5.

3.12.3.2 Horizontal and Vertical Advection

In the JMA-ATM, tracers are transported by mean wind velocity $\left(\overline{U}, \overline{V}, \overline{W} \right)$ at each tracer location as derived by interpolating forecast gridded data from the GSM (see Section 3.2), MSM (see Section 3.5) or LFM (see Section 3.7). The time tendencies of transport process are given by

$$f_\lambda^{\text{hadv}} = \frac{\overline{U}}{R_{\text{E}} \cos \varphi} \quad (\varphi \neq \pm 90°) \tag{3.12.9}$$

$$f_\varphi^{\text{hadv}} = \frac{\overline{V}}{R_{\text{E}}} \tag{3.12.10}$$

$$f_z^{\text{vadv}} = \overline{W} \tag{3.12.11}$$

where R_{E} is the radius of earth.

3.12.3.3 Horizontal and Vertical Diffusion

The effects of horizontal dispersion are represented using horizontal wind perturbation $(U'(t), V'(t))$ from mean wind $(\overline{U}(t), \overline{V}(t))$. $(U'(t), V'(t))$ are given by

$$U'(t) = R_{U'}(\Delta t)U'(t - \Delta t) + \sqrt{1 - R_{U'}(\Delta t)^2}\,\sigma_{U'}\Gamma \tag{3.12.12}$$

$$V'(t) = R_{V'}(\Delta t)V'(t - \Delta t) + \sqrt{1 - R_{V'}(\Delta t)^2}\,\sigma_{V'}\Gamma \tag{3.12.13}$$

Here, Γ represents a random number which obeys Gaussian distribution with a mean of 0 and a standard deviation of 1. The autocorrelation coefficients of Lagrangian velocity $(R_{U'}, R_{V'})$ are given by

$$R_{U'}(\Delta t) = R_{V'}(\Delta t) = e^{-\Delta t/t_{Lh}} \tag{3.12.14}$$

using the Lagrangian time scale t_{Lh}, and their standard deviations $(\sigma_{U'}, \sigma_{V'})$ are

$$\sigma_{U'} = \sigma_{V'} = \sqrt{\frac{K_h}{t_{Lh}}} \tag{3.12.15}$$

The parameters are set to $K_h = 5.864 \times 10^3\,\mathrm{m^2 s^{-1}}$ (for VAAs) or $5.864 \times 10^4\,\mathrm{m^2 s^{-1}}$ (for VAFFs), $t_{Lh} = 5.0 \times 10^4\,\mathrm{s}$, and the initial condition of horizontal wind perturbation is $U'(0) = V'(0) = 0.253\Gamma\,\mathrm{m\,s^{-1}}$ following Kawai (2002).

The time tendencies of horizontal dispersion process $\left(f_\lambda^{hdif}, f_\varphi^{hdif}\right)$ are determined by assigning (U', V') to Eqs. (3.12.9) - (3.12.10) rather than $(\overline{U}, \overline{V})$.

Meanwhile, vertical dispersion is represented as atmospheric vertical turbulence. The diffusion coefficient K_v is given using vertical shear of mean horizontal wind $\overline{\boldsymbol{U}_h} = (\overline{U}, \overline{V})$ as

$$K_v = l^2 \left|\frac{\partial \overline{\boldsymbol{U}_h}}{\partial z}\right| F_v(R_f) \tag{3.12.16}$$

Here, $F_v(R_f)$ represents atmospheric stability as a function of the flux Richardson number R_f given by the level 2 scheme of Mellor and Yamada (1974, 1982). The mixing length l is given by

$$l = \frac{\kappa z'}{1 + \kappa z'/l_0} \tag{3.12.17}$$

Here, z' is height above ground surface, κ is von Kármán constant (set to 0.4) and l_0 is the maximum mixing length given by Holtslag and Boville (1993)

$$l_0 = \begin{cases} l_{FA} + (l_{PBL} - l_{FA})\exp\left(1 - \dfrac{z'}{h_{PBL}}\right) & (z' > h_{PBL}) \\ l_{PBL} & (z' \le h_{PBL}) \end{cases} \tag{3.12.18}$$

The maximum mixing length in the free atmosphere l_{FA}, that in the planetary boundary layer (PBL) l_{PBL} and height of PBL h_{PBL} are set to 30 m, 100 m, 1000 m, respectively.

The time tendency of vertical dispersion process is given by

$$f_z^{vdif} = W' = \frac{\sum' \sqrt{2K_v \Delta t'}\,\Gamma}{\Delta t} \qquad (\Delta t = \Sigma'\Delta t') \tag{3.12.19}$$

Here, $\Delta t' (\le \Delta t)$ is the limitation of time step to prevent the displacement by vertical dispersion from becoming excessively large (Iwasaki *et al.* 1998).

3.12.3.4 Gravitational Fallout

In the JMA-ATM, it is assumed that volcanic ash particles fall at their terminal velocity w_t, as determined from the equation for balance between gravitational force and air resistance force:

$$w_t(D, z) = \sqrt{\frac{4C_C(\rho_p - \rho_a)gD}{3C_a\rho_a}} \tag{3.12.20}$$

where ρ_p is particle density, ρ_a is air density and C_a is the drag coefficient in consideration of the shape parameter $F = (a_2 + a_3)/2a_1$ (where a_1, a_2 and a_3 are particle principal axes, with a_1 as the longest) as given by Suzuki (1983):

$$C_a = \frac{24}{Re}F^{-0.32} + 2\sqrt{1.07 - F} \tag{3.12.21}$$

where Re is the Reynolds number represented as $Re = \rho_a w_t D/\eta_a$ with air viscosity η_a. C_C is the Cunningham correction factor, which is used to account for the reduction of drag on small particles and is expressed as

$$C_C = 1 + Kn\left[1.257 + 0.400\exp\left(-\frac{1.100}{Kn}\right)\right] \tag{3.12.22}$$

with the Knudsen number $Kn = 2\text{MFP}/D$ based on the mean free path of air MFP. η_a and MFP are given as follows:

$$\eta_a(z) = \eta_0\left[\frac{1 + C_S/T_0}{1 + C_S/T(z)}\right]\left[\frac{T(z)}{T_0}\right]^{1/2} \tag{3.12.23}$$

$$\text{MFP}(z) = \text{MFP}_0\frac{\eta_a(z)}{\eta_0}\left[\frac{p(z)}{p_0}\right]^{-1}\left[\frac{T(z)}{T_0}\right]^{1/2} \tag{3.12.24}$$

where $p(z)$ is air pressure at height z, $T(z)$ is air temperature at z, and C_S is the Sutherland constant of air (117 K). η_0 (18.18 μPa s) and MFP_0 (0.0662 μm) are the standard values for the reference atmosphere ($T_0 = 293.15$ K and $p_0 = 1013.25$ hPa).

The density of volcanic ash particles ρ_p is defined as a function of diameter D:

$$\rho_p(D) = \frac{\rho_{min} + a\rho_{max}D}{1 + aD} \tag{3.12.25}$$

where $a = 5 \times 10^3$ m^{-1}, ρ_{max} is the density for coarse tephra and is set to 1×10^3 kg m^{-3} as per the density of pumice stone, ρ_{min} is the density for fine ash and is set to 2.4×10^3 kg m^{-3}.

The time tendency of gravitational fallout process is given by

$$f_z^{fall} = -w_t \tag{3.12.26}$$

3.12.3.5 Dry and Wet Deposition

Dry deposition works on tracers within the surface boundary layer. The dry deposition rate P_d is computed from the depth of the surface boundary layer L_r and dry deposition velocity V_d as follows:

$$P_d = \begin{cases} \dfrac{V_d\Delta t}{L_r} & (z' \leq L_r) \\ 0 & (z' > L_r) \end{cases} \tag{3.12.27}$$

V_d is represented in consideration of the aerodynamic resistance r_a (Kitada *et al.* 1986)

$$V_d = \frac{1}{r_a} \tag{3.12.28}$$

$$r_a = \frac{1}{\kappa u_*}\ln\frac{z' - d}{z_0} \tag{3.12.29}$$

$$u_* = \kappa U_\mathrm{h} \Big/ \ln \frac{z' - d}{z_0} \tag{3.12.30}$$

where U_h is horizontal wind speed. Roughness length z_0 and zero-plane displacement d are determined from vegetation type or sea surface temperature.

For tracers judged to be deposited based on the probability Eq. (3.12.27), the time tendency of the dry deposition process is given by

$$f_\mathrm{z}^\mathrm{ddep} = -\frac{z'}{\Delta t} \tag{3.12.31}$$

which means the tracers are deposited on the surface while one time step.

Wet deposition involves a washout process (below-cloud scavenging) representing the deposition of tracers via precipitation and a rainout process (in-cloud scavenging) representing removal of tracers via their roles as cloud condensation nuclei. In the JMA-ATM for operational use, only the washout process is considered. The wet deposition probability associated with the type of precipitation (α = r(rain), s(snow), g(graupel)) is given by

$$P_{\mathrm{w}(\alpha)} = \begin{cases} 1 - e^{-\Lambda_{\mathrm{w}(\alpha)}\Delta t} & (z' < L_\mathrm{b}) \\ 0 & (z' \geq L_\mathrm{b}) \end{cases} \tag{3.12.32}$$

where L_b is the height of cloud base and $\Lambda_{\mathrm{w}(\alpha)}$ is the wet deposition rate given by

$$\Lambda_{\mathrm{w}(\alpha)} = A_\alpha R_\alpha^{B_\alpha} \tag{3.12.33}$$

where $R_\alpha \, [\mathrm{mm\,h^{-1}}]$ is precipitation intensity. The below-cloud scavenging coefficients are set to $A_\mathrm{r} = A_\mathrm{s} = A_\mathrm{g} = 2.98 \times 10^{-5}\,\mathrm{s^{-1}}$, $B_\mathrm{r} = 0.75$ and $B_\mathrm{s} = B_\mathrm{g} = 0.30$.

The time tendency of washout process is given by

$$f_\mathrm{z}^{\mathrm{wout}(\alpha)} = -\frac{z'}{\Delta t} \tag{3.12.34}$$

in the same way as for the dry deposition process.

3.12.3.6 Time Integration

Two types of time integral methods, the Euler method (as shown in Eqs. (3.12.6) - (3.12.8)) and the four-stage Runge-Kutta (RK4) method are implemented for the JMA-ATM. The Euler method integrates time tendencies of processes which have dependency on time step Δt such as dispersion processes and deposition processes. While the RK4 method is used for transport processes and gravitational fallout process for VAFFs. Following the RK4 method, a variable ϕ_i after the time step Δt is calculated by

$$\phi_i(t + \Delta t) = \phi_i(t) + \frac{1}{6} \sum_k \left(d_i^{k(1)} + 2d_i^{k(2)} + 2d_i^{k(3)} + d_i^{k(4)} \right) \Delta t \tag{3.12.35}$$

$d_i^{k(1)}$, $d_i^{k(2)}$, $d_i^{k(3)}$ and $d_i^{k(4)}$ are specified by the time tendency f_i^k of each process k as

$$d_i^{k(1)}(t) = f_i^k \left(t, \phi_i(t) \right) \tag{3.12.36}$$

$$d_i^{k(2)}(t) = f_i^k \left(t + \frac{1}{2}\Delta t, \phi_i(t) + \frac{1}{2}d_i^{k(1)}\Delta t \right) \tag{3.12.37}$$

$$d_i^{k(3)}(t) = f_i^k \left(t + \frac{1}{2}\Delta t, \phi_i(t) + \frac{1}{2}d_i^{k(2)}\Delta t \right) \tag{3.12.38}$$

$$d_i^{k(4)}(t) = f_i^k \left(t + \Delta t, \phi_i(t) + d_i^{k(3)}\Delta t \right) \tag{3.12.39}$$

3.12.4 Products

3.12.4.1 Volcanic Ash Advisory

VAAC Tokyo issues VAAs in text, graphical and IWXXM (XML/GML) formats as defined in ICAO (2018). VAAs include information on the forecast height and area of ash clouds 6, 12 and 18 hours ahead of observation times based on JMA-ATM results. The forecast is normally updated every six hours (at 00, 06, 12 and 18 UTC) when ash clouds are identified in satellite imagery. If notable changes occur in ash clouds, updates are provided as often as needed. Sample VAAs are shown in Figures 3.12.1 and 3.12.2.

```
FVFE01 RJTD 130600
VA ADVISORY
DTG: 20210813/0600Z
VAAC: TOKYO
VOLCANO: FUKUTOKU-OKA-NO-BA 284130
PSN: N2417 E14129
AREA: JAPAN
SUMMIT ELEV: -29M
ADVISORY NR: 2021/3
INFO SOURCE: HIMAWARI-8
AVIATION COLOUR CODE: NIL
ERUPTION DETAILS: VA EMISSIONS CONTINUING
OBS VA DTG: 13/0520Z
OBS VA CLD: SFC/FL540 N2413 E14136 - N2251 E13850 - N2243 E13455 -
N2336 E13423 - N2455 E13655 - N2442 E14134 MOV W 50KT
FCST VA CLD +6 HR: 13/1120Z SFC/FL560 N2420 E14141 - N2116 E13432 -
N2121 E13006 - N2157 E12908 - N2348 E13229 - N2529 E13959
FCST VA CLD +12 HR: 13/1720Z SFC/FL550 N2415 E14153 - N1904 E12509 -
N1926 E12334 - N2441 E13143 - N2646 E13913
FCST VA CLD +18 HR: 13/2320Z SFC/FL560 N2413 E14153 - N1623 E11912 -
N1648 E11823 - N2520 E12821 - N2745 E13859
RMK: NIL
NXT ADVISORY: 20210813/0900Z=
```
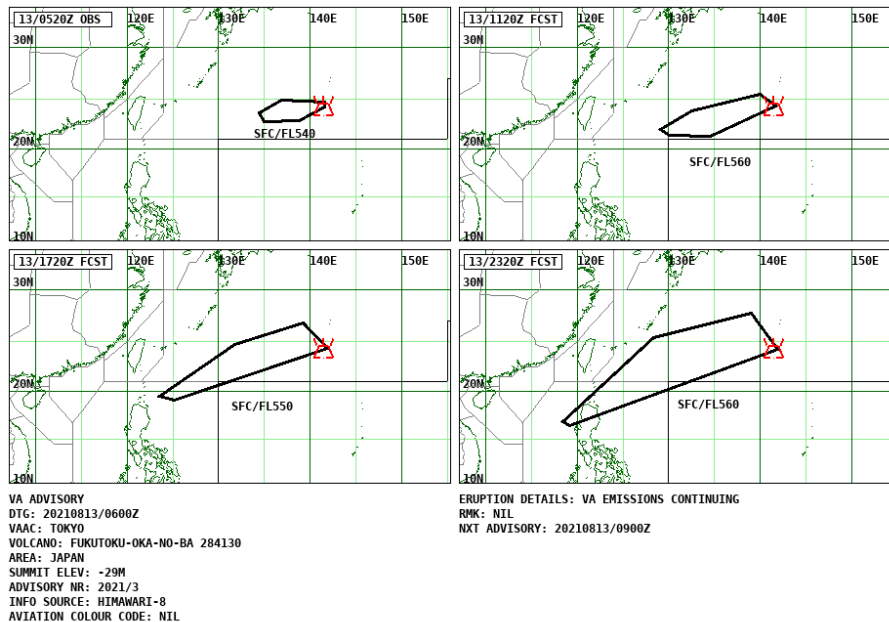
Figure 3.12.1: Sample VAA in text form

Figure 3.12.2: Sample VAA in graphical form

3.12.4.2 Volcanic Ash Fall Forecast

JMA provides three types of forecasts sequentially: VAFFs (Scheduled) are issued periodically based on an assumed eruption for active volcanoes, VAFFs (Preliminary) are brief forecasts up to one hour ahead issued within 5 - 10 minutes of an actual eruption, and VAFFs (Detailed) are more accurate forecasts up to six hours ahead every hour issued within 20 - 30 minutes of an actual eruption. The amount of volcanic ash fall and maximum particle size at grid points with spacing of 0.02 degrees are calculated based on tracers falling to the surface for use in VAFFs. The amount of ash fall is shown in three qualitative categories combined with recommended action to be taken by the general public (Hasegawa *et al.* 2015). VAFFs include graphical information on ash quantities and lapilli pieces with dimensions of 1 cm or more as well as text information on the direction of ash drift, municipalities affected and precautions for disaster prevention. Sample VAFFs are shown in Figures 3.12.3 (Scheduled), 3.12.4 (Preliminary) and 3.12.5 (Detailed).
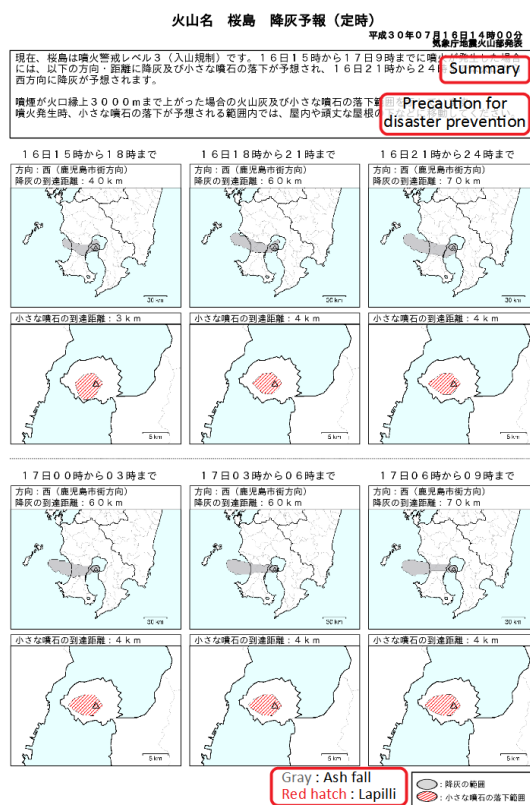

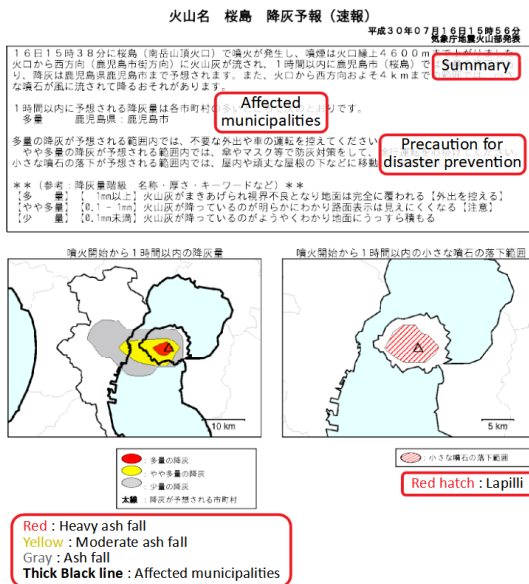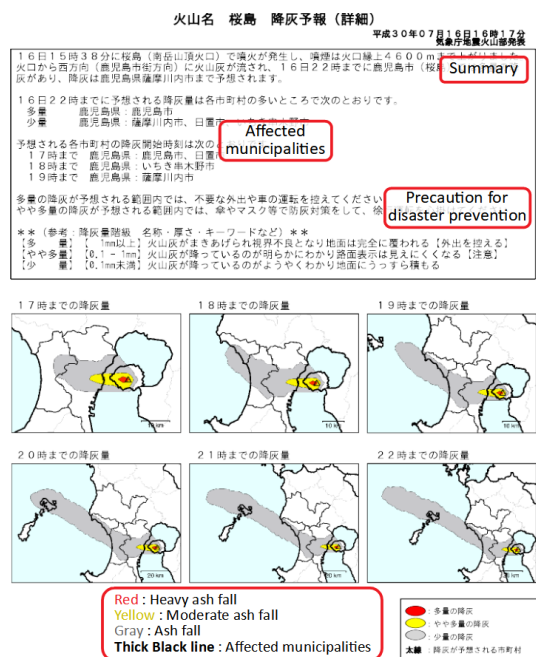Figure 3.12.3: Sample VAFF (Scheduled)

Figure 3.12.4: Sample VAFF (Preliminary)

Figure 3.12.5: Sample VAFF (Detailed)